

---

# Methods<sup>1</sup>

---

## Expedition 335 Scientists<sup>2</sup>

### Chapter contents

Introduction .....	1
Igneous petrology .....	6
Geochemistry .....	10
Alteration and metamorphism .....	13
Structural geology .....	15
Paleomagnetism .....	19
Physical properties .....	22
Downhole logging .....	30
Core section image analysis .....	34
Underway geophysics .....	35
References .....	36
Figures .....	39
Tables .....	68

### Introduction

This chapter documents the procedures and methods employed in the various shipboard laboratories during Expedition 335 of the Integrated Ocean Drilling Program (IODP). This information applies only to shipboard work described in the *Expedition Reports* section of the Expedition 335 *Proceedings* volume. Also described is the information architecture for the population and extraction of curatorial information, as well as shipboard scientific observations and data from the Laboratory Information Management System (LIMS) database and the Sample Master and DESClogik interfaces. Methods for shore-based analysis of Expedition 335 samples and data will be described in the individual scientific contributions to be published in the *Research Results* section of the Expedition 335 *Proceedings* volume and in international peer-reviewed literature.

### Authorship

All shipboard scientists contributed to this volume. However, certain sections were written by discipline-based groups of scientists as listed below (group leaders and then alphabetically):

Expedition 335 summary: Expedition 335 Scientists  
Methods and Hole 1256D:

Background and objectives: Teagle and Ildefonse

Operations: Grout, Ildefonse, Blum, and Teagle

Igneous petrology: Lissenberg, Abe, Adachi, Dick, Koepke,  
Miyashita, Oizumi, and Payot

Alteration and metamorphism: Alt, Abily, France, Harris, and  
Python

Structural geology: Anma, Deans, Endo, Ferre, and Till

Geochemistry: Godard, Kurz, and Roy

Paleomagnetism: Morris and Kim

Physical properties: Tominaga and Baines

Core section image analysis: Wilson

Downhole measurements: Guerin, Zakharova, and Wilson

Underway geophysics: Wilson

Deep drilling of intact crust: harnessing past lessons to inform  
future endeavors: Ildefonse and Teagle

<sup>1</sup>Expedition 335 Scientists, 2012. Methods. In Teagle, D.A.H., Ildefonse, B., Blum, P., and the Expedition 335 Scientists, *Proc. IODP, 335*: Tokyo (Integrated Ocean Drilling Program Management International, Inc.).

doi:10.2204/iodp.proc.335.102.2012

<sup>2</sup>Expedition 335 Scientists' addresses.



## Numbering of sites, holes, cores, and samples and computation of depth

Drilling sites are numbered consecutively from the first site drilled by the *Glomar Challenger* in 1968. Starting with IODP Expedition 301, the prefix “U” designates sites occupied by the US Implementing Organization (USIO) vessel, the R/V *JOIDES Resolution*. Site 1256 does not follow this nomenclature because it was started during Ocean Drilling Program (ODP) Leg 206 (although the “U” does currently appear in online database reports). At a site, multiple holes are often drilled. For all IODP drill sites, a letter suffix distinguishes each hole drilled at the same site. The first hole drilled is assigned the site number modified by the suffix “A,” the second hole takes the site number and the suffix “B,” and so forth. Hole 1256D was the fourth hole drilled at Site 1256 (Wilson, Teagle, Acton, et al., 2003).

While on site, ship location over a hole is maintained with respect to one or two positioning beacons deployed on the seafloor and in active communication with the Neutronics 5002 dynamic positioning (DP) system on the *JOIDES Resolution*. In general, the primary reference for DP is GPS; the beacon reference acts as a backup in the event that GPS becomes unreliable.

The cored interval is measured in meters below rig floor (mbrf) and reported in meters below seafloor (mbsf). Depth below seafloor is determined by subtracting the seafloor depth measured from the rig floor, as determined from the initial drill pipe measurement at Hole 1256B (3645.4 m) (Wilson, Teagle, Acton, et al., 2003) from the rig floor measurements. Note that according to the recent IODP Depth Scales Terminology version 2 ([www.iodp.org/program-policies/2/](http://www.iodp.org/program-policies/2/)), the mbsf scale is defined as the core depth below seafloor, method A (CSF-A), with units of meters. The computations of mbsf and m (CSF-A) depths are exactly the same.

During most IODP expeditions, each cored interval is generally 9.5–9.8 m long, which is the length of a core barrel. However, one potential cause of poor recovery during hard rock coring is core jamming in the bit or in the throat of the core barrel. Once the opening in the bit is jammed, core is prevented from entering the core barrel. During ODP hard rock coring missions, core barrels were often extracted at shorter penetration intervals in order to mitigate loss of core when the bit was blocked. This strategy improved core recovery in Hole 1256D during Leg 206 and IODP Expedition 309 and was the standard operating procedure throughout IODP Expedition 312. All cores recovered from Hole 1256D during Expedi-

tion 335 were cored at intervals of 4.7 m half-cores or less.

Each core recovered is divided into 1.5 m sections that are numbered serially from the top. When full recovery is achieved, the sections are numbered sequentially as recovered, starting with 1 at the top of the core; the last section may be shorter than 1.5 m (Fig. F1). For the purpose of nominal depth calculation, the top depth of the core is equated with the top depth of the cored interval (in mbsf) by convention, to achieve consistency in handling analytical data derived from cores. All pieces recovered are placed immediately adjacent to each other in the core tray. Samples and descriptions of cores are designated by distance, measured in centimeters from the top of the section to the top and bottom of each sample or interval. A full identifier for a sample consists of the following information: expedition, site, hole, core number, core type, section number, section half identifier (if applicable), top and bottom offsets in centimeters measured from the top of section (half), and additional subsample names if applicable. For example, the designation “Sample 335-1256D-235R-1W, 0–1 cm (Thin Section 2)” represents the second thin section made during the expedition, of a billet removed from the interval between 0 and 1 cm at the top of working section half 1W in Core 235R (R designates that this core was taken with the rotary core barrel) of Hole 1256D from Expedition 335. In addition, core pieces are numbered sequentially from the top of each section, and if a core piece can be reassembled the piece numbers are annotated with the suffix “A, B,” and so forth.

## Curation protocols for geologic and industrial materials recovered by fishing and hole cleaning operations during Expedition 335

Extensive hole cleaning operations undertaken during Expedition 335 recovered a large amount of geologically valuable materials from Hole 1256D, as well as metallic junk from drilling, fishing, and milling equipment. To preserve the operational information and source of samples retrieved by fishing, reaming, and cleaning operations, nomenclature was developed for identifying on which reentry and from what device the samples were collected. Materials were recovered from external (EXJB; when deployed in multiples, EXJB1 and EXJB2), bit sub (BSJB), flow-through (FTJB), and reverse circulation (RCJB) junk baskets and the fishing magnet (FM) (see Fig. F19 in the “Expedition 335 summary” chapter [Expedition 335 Scientists, 2012a]). A very large amount of sand-sized cuttings were recovered from the drill collars (DCs). Table T1 shows the nomenclature for identifying the reentry (run) number and the sample re-

covery device. Full operations details of the numerous hole-clearing runs are documented in “Operations” and Table T3, both in the “Expedition 335 summary” chapter (Expedition 335 Scientists, 2012a). For curatorial reasons, the original sample depth was assigned somewhere in Hole 1256D from the bottom of the 16 inch casing to the total depth (270–1520 mbsf). For many materials, tighter depth ranges can be assigned from operational (e.g., bit withdrawals) and geological (e.g., igneous texture, alteration, and metamorphism) information. Large rocks (>5 cm) were assigned individual identification letters (e.g., Run12-RCJB-Rock B). Cobble-sized samples were weighed and measured individually (see Table T6 in the “Site 1256” chapter [Expedition 335 Scientists, 2012b]), whereas smaller samples were clustered by texture and grain size. Shipboard analyses (e.g., thin sections and inductively coupled plasma–atomic emission spectroscopy [ICP-AES] analyses) could then be tied to a particular rock or cutting style (sand or rubble) from a specific tool on a specific reentry run (Table T1).

### Core reference frame for sample orientation

Each core piece that has a length exceeding that of the core liner diameter is associated with its own core reference frame (CRF) (Fig. F2). The primary reference is the axial orientation (i.e., the top and bottom of the piece) based on the piece’s orientation when extracted from the core barrel. The core axis defines the *z*-direction, where positive is downcore. The secondary reference is an arbitrarily marked axis-parallel line on the whole-round surface of the piece. This is the cut line, which marks the plane through the cut line and the core axis where the piece will be split. The cut line is selected by scientists to maximize the dip angle of planar features on the split surface, which facilitates accurate structural measurements. The *x*-axis of the CRF is defined orthogonally to the cut plane, positive (000°) into the working half and negative (180°) into the archive half. The *y*-axis is orthogonal to the *x*-*z* plane and, using the right-hand cork-screw rule, is positive (090°) to the left and negative (270°) to the right when looking upcore onto the archive half.

Cube samples taken from the working half were marked with an arrow in the negative *z*-direction (upcore) on the working half surface (*x*-*y* plane), which defines the cube’s orientation unequivocally within the CRF. Thin section billets and thin sections made of billets were also marked with an upcore arrow, in addition to a “~” sign marking the 270° direction. Thin section billets taken from the *x*-*y* plane (i.e., bottom or top face of the piece) and thin sec-

tions made from such billets were marked with “Ø” and the “~” symbol for the 270° direction. For thin sections cut in the *x*-*z* plane, an arrow indicates the uphole direction, and “@” indicates the thin section faces 090°, whereas “\$” indicates a 270° facing (Fig. F2).

### Core handling and core flow

The 15 steps of the core handling and core flow process, from coring to shipboard sampling, are summarized in Figure F3. Nonmagnetic core barrels were used throughout Expedition 335. Because of high ambient temperatures at the bottom of ODP Hole 1256D (>100°C), and to minimize the risk of cores jamming, all cores during Expedition 335 were recovered without plastic liners. When the core came to the rig floor, the Curator, supported by USIO technicians, waited with presplit core liners at the end of the catwalk. Once the core barrel was lowered horizontally, each rock piece was removed from the core barrel one by one and placed in consecutive order in 1.5 m split plastic liners labeled “A” through “D” (“A” through “F” for 9 m cores), with “A” being the lowermost split liner section. Blue and colorless liner caps denote the top and bottom of each split liner, respectively. This convention was used throughout the curation process. Before each piece was removed from the core barrel, the curator marked the bottom of all oriented pieces with a red wax pencil. In some cases, pieces too small to be oriented with certainty were marked before they were extracted from the core barrel. Therefore, the red wax mark does not universally indicate that the core piece was oriented. The core catcher sample was added to the bottom of split section A. To minimize contamination of the core with platinum group elements and gold, all personnel handling and describing the cores or other sample material removed jewelry from their hands and wrists before handling. For cores where the selection of microbiological samples was planned, all personnel handling the cores wore nitrile gloves to reduce contamination.

Once all core material was removed from the core barrel, split sections were transferred to the catwalk or core splitting area, and the rock material in each section was measured and entered into Sample Master as Recovered Length (Fig. F4). This parameter was used to compute core recovery. While the core was being recovered from the core barrel on the catwalk, identification labels were put on prescribed split liners. After transport to the splitting room, core pieces were transferred into the prescribed and labeled liners. After all pieces were placed in the labeled split liners, the curator and one other technician washed

the whole-round pieces, one piece at a time, and allowed them to dry.

The rocks in each section were then placed into sample bins, by inserting plastic core dividers between individual pieces. These spacers may represent substantial intervals of no recovery. Adjacent core pieces that could be fitted together along fractures were curated as single pieces. Core pieces that appeared susceptible to crumbling were encased in shrink-wrap. Once binning activities and curatorial measurements were completed, a digital photograph was taken of the unlabeled section for insurance against accident during the prelabeling handling of whole-round pieces.

A designated scientist was then called to the splitting room to check the binning and reconstruction of fractured pieces. A splitting line was marked on each piece with a red wax pencil so that the piece could be split into representative working and archive halves, ideally maximizing the expression of dipping structures on the cut face of the core while maintaining representative features in both archive and working halves (Fig. F2). To ensure a consistent protocol for whole-core imaging (see “[Core section image analysis](#)”), the splitting line was drawn so that the working half was on the right side of the line with the core upright. The working half of each piece was marked with a “W” to the right of the splitting line. Where magmatic fabrics were present, cores were marked for splitting with the fabric dipping to the east (090°) in the IODP CRF. This protocol was sometimes overridden by the presence of special features (e.g., xenoliths, mineralized patches, and dike margins) that were subdivided between the archive and working halves to ensure preservation and/or allow shipboard or postcruise sampling.

Once the split line was drawn, the curator secured the plastic spacers permanently with acetone between individual pieces into matching working and archive half split core liners. Spacers were mounted into the liners with the angle brace facing uphole. This ensured that the top of each piece had the same depth as the top of the curated interval for each bin. The length of each bin was entered into Sample Master as Bin Length. The cumulative length of all bins, including spacers, was entered as the Curated Length of the section. Oriented pieces were recorded at this stage. The caliper length (longest vertical dimension) of each piece was also measured by the curator and entered into Sample Master as Piece Length (Fig. F4). Once all curatorial information had been entered and uploaded, the empty section half with bins was placed over the full half and taped together in a few places to dry and equilibrate to core laboratory conditions (usually <1 h from arrival from the catwalk).

Once thermally equilibrated, the magnetic susceptibility and natural gamma radiation (NGR) signal of each section was measured using the shipboard Whole-Round Multisensor Logger (WRMSL) and the Natural Gamma Radiation Logger (NGRL), respectively (see “[Whole-Round Multisensor Logger measurements](#)” and “[Natural Gamma Radiation Logger](#)”), and the outer cylindrical surfaces of whole-round pieces were scanned with the adapted Section Half Imaging Logger (SHIL) using the split line marking for registration (see “[Core section image analysis](#)”).

Each piece of core was then split into archive and working halves, with the positions of plastic spacers between pieces maintained in both halves. Piece halves were labeled sequentially from the top of each section, beginning with number 1; reconstructed groups of piece halves were assigned the same number but were lettered consecutively. Pieces were labeled only on the outer cylindrical surfaces of the core. If the piece was oriented with respect to the way up, an arrow was added to the label, pointing to the top of the section. Digital images of the dry, cut faces of archive halves were captured with the SHIL (see “[Core section image analysis](#)”). Sections were then transferred to the Section Half Multisensor Logger (SHMSL) where laser piece height, color reflectance, and contact probe magnetic susceptibility were measured (see “[Section Half Multisensor Logger measurements](#)”).

Following sample curation, whole-round and section half measurement and imaging, and splitting (Fig. F3), the archive section halves of each core were described by expedition scientists, and observations were recorded using the DESClogik interface and uploaded into the LIMS database (for details, see individual disciplinary sections in this chapter). Archive section halves were also passed through the cryogenic magnetometer for magnetic remanence measurements (see “[Paleomagnetism](#)”).

Digital color close-up images were taken of particular features for illustrations in the summary of each site, as requested by individual scientists. Working section halves of cores were sampled for both shipboard characterization of cores and shore-based studies. Samples were routinely taken for shipboard physical properties (minicore or 8 cm<sup>3</sup> cube), paleomagnetic (minicore or 8 cm<sup>3</sup> cube), thin section (billet or slab), and geochemical (billet, slab, or quarter round) analyses, as described in the sections below. Each extracted sample was logged into the LIMS database using the Sample Master program, including the sample type and either the shipboard analysis (test) conducted on the sample or the name of the investigator receiving the sample for postcruise analysis.



Records of all samples taken from the cores were stored in the LIMS database and are accessible online ([iodp.tamu.edu/tasapps/](http://iodp.tamu.edu/tasapps/)). Extracted samples were sealed in plastic vials, cubes, or bags and were labeled.

Following shipboard initial scientific observations, measurements, and sampling, both core halves were shrink-wrapped in plastic to prevent rock pieces from moving out of sequence during transit. Working and archive halves were then put into labeled plastic tubes, sealed, and transferred to cold-storage space aboard the drilling vessel. At the end of Expedition 335, cores were transferred from the ship for permanent storage at the IODP Gulf Coast Repository in College Station, Texas (USA).

## Information architecture

### Laboratory Information Management System

The USIO LIMS database is an infrastructure to store all operational, sample, and analytical data produced during a drilling expedition. The LIMS database comprises an Oracle database and a custom-built asset management system, along with numerous web services to exchange data with information capture and reporting applications. More than 30 data capture applications, most of them USIO custom tools built to support specific shipboard workflows, collect information and store it in the LIMS database. Several data retrieval applications are available to access the data from the LIMS database for different purposes (Fig. F5).

### Data capture tools

All samples collected during Expedition 335 were registered in the LIMS database using the Sample Master application. The program has workflow-specific interfaces to meet the needs of different users. Sample registration begins with the driller entering information about the hole and then the cores retrieved from the hole. IODP personnel entered additional core information, sections, pieces, and any other subsamples taken from these, such as cubes or thin section billets. One interface is designed for visiting scientists so they can autonomously enter subsample information according to the sampling plan.

Five imaging systems available on the *JOIDES Resolution* were used to produce six types of images:

1. Whole-round section surface (360°) images using the converted SHIL, used for the first time during Expedition 335 (see “[Core section image analysis](#)”);
2. Section half surface images using the SHIL;

3. Core composite images combining multiple section half images into the traditional “core table” view;
4. Close-up images taken to meet special imaging needs not covered with routine line scan images;
5. Whole-area thin section images using a custom-built system; and
6. Photomicrographs using commercial cameras mounted on optical microscopes.

All images were uploaded to the LIMS database immediately after capture and were accessible via browser-based reports. Images were provided in at least one generally usable format (JPG, TIFF, or PDF) and in multiple formats if appropriate.

Physical properties, paleomagnetic, and geochemistry analytical systems in the shipboard laboratories were used to capture instrumental data, as described in the following sections. In cases where no further user interaction was required, the data upload to the LIMS database was triggered automatically. In cases where quality control or data processing was needed before upload, the user triggered the upload to the LIMS database when the data were ready.

Descriptive and interpretive information (DESCINFO) was captured using the DESClogik custom software application, and all information was stored in the LIMS database. This system was still relatively new, and significant development occurred during Expedition 335 in terms of worksheet configuration for hard rock descriptions and application feature development. The main DESClogik interface is a spreadsheet with extensive data entry and data validation support. The columns and tabs are entirely configurable by USIO staff based on users’ definitions of what information should be collected (see “[Core description overview](#)”). USIO staff then enables entry columns based on sets of parameters that make up the DESCINFO data structure.

### Data retrieval

Data tables were mostly populated using the recently deployed LIMS Reports (Fig. F5), where the user selects the type of desired information from ~30 available reports, selects a hole (and cores and sections), and uses additional report-specific filters, if desired, to view a report online or download information in a standard comma-separated value (CSV) file. For information reporting not yet implemented in LIMS Reports (a beta version was used during Expedition 335), the original Web Tabular Report (WTR) was used to access data. Information retrieved from the WTR generally represents all valid data stored in the

LIMS database for a given analysis, but the formats are not always user friendly.

Another alternative for retrieving data from the LIMS database was to use LIMS2Excel, a highly configurable Java-based data extractor where users can save a specific configuration for any combination of data parameters and export it into a Microsoft Excel workbook.

Many data sets could also be viewed on LIMSpeak, a browser-based application that plots cores, sections, and samples along with a user-selected data set, including images and other data sets, against depth. The application is particularly useful for monitoring data acquisition, real-time quality control, and browsing images.

## Core description overview

### Work flow

Three teams were formed to describe igneous petrology, alteration and metamorphic petrology, and structural geology in all core sections and thin sections prepared onboard. This disciplinary team approach ensured that all members of a specialty group were able to see all recovered material and work in a coordinated fashion to produce consistent data sets. The teams were each assigned a 12 h shift, spaced out to provide sufficient time and space for each team to examine the cores and also to ensure overlap with the other teams for information exchange. The igneous petrology team started at 2400 h and was responsible for defining igneous units in the recovered section. The alteration and metamorphism group worked 0600–1800 h, and the structural geology team started at 1200 h. Daily science meetings with the entire expedition Shipboard Scientific Party were held to avoid the development of singular department achievement philosophies.

### Descriptive data capture workbooks

At the beginning of the expedition, each group defined observables as Excel spreadsheet columns, and those specifications were subsequently implemented as columns, tabs, and workbooks in the DESClogik application. Observable parameters were of three types: controlled values, free text, and numbers. For the controlled value columns, subject matter experts defined specific value lists that were configured in DESClogik as drop-down lists to facilitate consistent data capture. These values are defined in each description team's section. Free text fields had no constraints and were used for comments. Number columns were used to log abundance percentage, size, intensity, and rank (for plotting) of physical constituents, texture, and structures.

The three teams defined 640 data capture columns. Columns were arranged in tabs and workbooks as agreed upon within each description team and among the three teams. Arrangements were optimized to support the description workflow and to avoid overlaps and gaps in data collection (Table T2).

### Section summary graphic (visual core descriptions)

With all observables specified, the science party selected a few of the parameters to be represented graphically on the section summary graphic, historically referred to as the visual core descriptions (VCDs). All the information for the VCDs was retrieved from the LIMS database via the LIMS2Excel tool. VCD information was plotted as symbols, patterns, and line plots with depth, along with some instrumental data, using the commercial plotting program Strater. Tabulated data summaries for the sections were generated using DESClogik and printed next to the plots postcruise. All information displayed on the VCDs was plotted or otherwise collected from the LIMS database in a semiautomated process supported by USIO staff.

## Igneous petrology

Rock description procedures during Expedition 335 closely followed those used during IODP Expeditions 304/305 (Blackman, Ildefonse, John, Ohara, Miller, MacLeod, and the Expedition 304/305 Scientists, 2006) and 309/312 (Teagle, Alt, Umino, Miyashita, Banerjee, Wilson, and the Expedition 309/312 Scientists, 2006). These, in turn, were based on ODP Leg 209 and earlier “gabbro” legs (ODP Legs 118, 147, 153, and 176) to maintain a relatively high degree of uniformity. As during Legs 176, 206, and 209 and Expeditions 304/305 and 309/312, core descriptions were performed by the entire igneous petrology team working together. Each member was responsible for one or more aspects of the description (igneous contacts, textures, mineral modes, and habits) to ensure consistency of recorded observations throughout the core, but commonly the entire team would work together, particularly when defining units and contacts.

Recovered core was described macroscopically and microscopically, and its characteristics were entered into the LIMS database through the DESClogik portal. Key information was entered into the Section-Unit summary tab in DESClogik. This information was then used for the production of VCDs, which summarize the description of each section of core (see “[Core descriptions](#)”). A key to symbols used on the VCDs is given in Figure F6.

## Igneous units and contact logs

The first step in describing core was the identification of unit boundaries on the basis of the presence of contacts, chilled margins, changes in primary mineralogy, color, grain size, and structural or textural variations. Igneous units in Hole 1256D were numbered continuously from the end of Expedition 312, starting with Unit 1256D-96. Lithologically and texturally similar pieces from consecutive core sections were curated as belonging to the same unit. In order to preserve important information about igneous stratigraphy without defining an unreasonable number of units within a single core, subunits were designated in cases where there were marked changes in texture without accompanying changes in mineralogy, or vice versa. In addition, crosscutting veins and thin dikes were generally designated as subunits. Where contacts deviated from horizontal within the core reference frame, their depth was logged at their midpoint. The igneous unit and contact log (see Table T4 in the “Site 1256” chapter) provides information about unit boundaries and a brief description of each unit. For each unit, the table lists unit number, depth (in meters below seafloor) of its top, core-section-interval and piece number of the top of the unit, unit thickness, lithology, a description of the upper and lower boundaries, and a unit description.

## Macroscopic core description

Macroscopic descriptions were divided into the following categories.

### Lithology

#### Plutonic rocks

Plutonic rocks were classified on the basis of abundance, grain size, and texture of their primary minerals (as inferred prior to alteration), based on the International Union of Geological Sciences (IUGS) system (Streckeisen, 1974; Le Maitre, 1989; Le Maitre et al., 2002). This classification defines the following rocks (Figs. F7, F8):

- Troctolite: olivine + plagioclase >95%, olivine >10%, and plagioclase >10%.
- Olivine gabbro: olivine + plagioclase + clinopyroxene, none of which is <5%.
- Gabbro or diorite: plagioclase + clinopyroxene >95%, plagioclase >10%, clinopyroxene >10%, and quartz <5%.
- Gabbronorite: plagioclase + clinopyroxene + orthopyroxene, none of which is <5%.

- Quartz diorite: quartz 5%–20% of quartz + alkali feldspar + plagioclase (QAP), with alkali feldspar <10% of QAP.
- Tonalite: quartz 20%–60% of QAP, with alkali feldspar <10% of QAP.
- Trondhjemite: tonalite with total mafic mineral content <10%.

In the IUGS classification, diorite is distinguished from gabbro by the anorthite content of plagioclase, with diorites having plagioclase containing <50 mol% An and gabbros having plagioclase containing >50 mol% An. Because this cannot be characterized during macroscopic description, we used the following convention: if a gabbroic rock contained quartz (<5%) or primary amphibole, indicating a relatively high degree of fractionation, the rock was classified as diorite. If no quartz or primary amphibole was observed, the rock was classified as gabbro.

Minor modifications to the IUGS system were made to divide the rock types more accurately on the basis of significant differences rather than arbitrary cutoffs based on the abundance of a single mineral. We have attempted to follow as closely as possible the descriptions from Leg 209 (Kelemen, Kikawa, Miller, et al., 2004) and Expeditions 304/305 (Blackman, Ildefonso, John, Ohara, Miller, MacLeod, and the Expedition 304/305 Scientists, 2006) and 309/312 (Teagle, Alt, Umino, Miyashita, Banerjee, Wilson, and the Expedition 309/312 Scientists, 2006) to facilitate inter-site comparison.

For gabbroic rocks, the following modifiers based on modal mineralogy are used:

Disseminated oxide = 1%–2% Fe-Ti oxide.

Oxide = >2% Fe-Ti oxide.

Olivine-bearing = 1%–5% olivine.

Orthopyroxene-bearing = 1%–5% orthopyroxene.

Troctolitic = 5%–15% clinopyroxene; >20% olivine.

Olivine-rich = >70% olivine.

Anorthositic = >80% plagioclase.

Additional descriptive modifiers are defined as follows:

Leucocratic = light colored, high proportions of plagioclase.

Micro = dominant grain size < 1 mm.

Doleritic = fine- or medium-grained gabbroic rocks with dominant ophitic or subophitic textures.

One rock type recovered during Expedition 335 contains high proportions (85%–95%) of apparently albitic plagioclase associated with minor amounts of Fe-Ti oxides, titanite, amphibole, and epidote; quartz

appears to be absent. These rocks have been classified as albitite.

### Volcanic rocks

For volcanic and hypabyssal rocks, we used the following definitions:

- Basalt: all igneous rocks of basaltic composition in the grain size range glassy to fine grained.
- Dolerite: holocrystalline, fine- to medium-grained rocks of basaltic composition with well-developed subophitic or ophitic textures.

In English language usage, the term “dolerite” is European in origin and functionally equivalent to the North American usage of diabase, which is the IODP standard term. However, in Japanese, the term diabase has a distinctly different meaning, referring to strongly altered (green) basaltic rocks, and is expressed differently in Kanji script. This usage of diabase is also prevalent in Europe. We therefore agreed to use dolerite.

Basalt was divided according phenocryst content, using the following convention:

Aphyric = <1% phenocrysts.

Sparsely phyrical = 1%–5% phenocrysts.

Moderately phyrical = >5%–10% phenocrysts.

Highly phyrical = >10% phenocrysts.

If present, phenocryst phases were placed as modifiers in front of the rock name with a hyphen in between. If <1% phenocrysts is present the rock is given the modifier “aphyrical.”

## Mineralogy

### Plutonic rocks

In oceanic plutonic rocks, the primary rock-forming minerals are olivine, plagioclase, clinopyroxene, orthopyroxene, amphibole, Fe-Ti oxide, sulfide, and quartz. The following data are recorded in the LIMS database for each primary silicate:

- Visually estimated modal percent: in fresh rocks this represents the modal mineralogy as observed; in (partially) altered rocks this represents the estimated igneous modes prior to alteration. Where a mineral occurs in trace quantities (i.e., too low to assign a meaningful percentage), 0.1% is recorded. Accessory phases are also noted where observed. Modal estimates were made independently for each phase by a different team member and summed. If the total deviated significantly from 100%, the unit was reexamined by the team and estimates were adjusted. Where totals were close to 100%, the mode of the most abundant mineral (generally plagioclase) was adjusted, retaining the original estimates of phases that occur in minor

abundance (generally oxides, olivine, and/or orthopyroxene). The rationale behind this procedure was that the absolute uncertainty in estimating modal proportions is largest for the most abundant minerals.

- Grain size: minimum, median, and maximum for each mineral phase.
- Mineral shape: euhedral, subhedral, and anhedral. Where oxides and sulfides form aggregates, they are divided into angular aggregates, amoeboid aggregates, and interstitial aggregates.
- Mineral habit:
  - Equant = aspect ratio < 1:2.
  - Subequant = aspect ratio 1:2 to 1:3.
  - Tabular = aspect ratio >1:3 to 1:5.
  - Elongate = aspect ratio > 1:5.
  - Interstitial.
  - Poikilitic.

The first four terms apply predominantly to subhedral or euhedral grains, the latter two generally to anhedral grains.

### Volcanic rocks

In volcanic and hypabyssal rocks, the groundmass, phenocrysts (if any), and vesicles were described. For the groundmass, grain size was recorded using the following definitions:

Glassy.

Cryptocrystalline = <0.1 mm.

Microcrystalline = 0.1–0.2 mm.

Fine grained = >0.2–1 mm.

Medium grained = >1–5 mm.

Coarse grained = >5–30 mm.

For phenocrysts, the abundance (in percent); maximum, minimum, and median grain size (in millimeters); and shape were recorded for each phase. For vesicles, abundance (in percent); vesicularity; size distribution; minimum, maximum, and modal size (in millimeters); roundness (rounded, subrounded, or well rounded); sphericity (highly spherical, moderately spherical, or slightly spherical or elongate); filling (in percent); and fill composition were documented. If vesicles are elongate, the direction is noted.

## Contacts

For contacts between units, the type, definition, geometry, and interpretation were described. Where the contact was not recovered this was noted.

Contact types are

- Grain size: units on either side have markedly different grain sizes,



- Modal: units on either side have markedly different mineral proportions, or
- Color: units on either side have markedly different primary (i.e., not alteration-related) color.

If contacts were characterized by combinations of the above parameters, the terms were combined (e.g., “grain size and modal contact”).

Where contacts are obscured by deformation and metamorphism, they are called

- Sheared: an interval with deformation fabric is in contact with an undeformed interval,
- Foliated: both intervals have deformation fabrics, or
- Tectonic: the contact appears to be the result of faulting.

Contact definitions describe how well defined a contact is, using the terms sharp, gradational, and sutured (contacts where individual mineral grains interlock across the contact). Contact geometry can be planar, curved, or irregular.

Following description, contacts are interpreted as being extrusive, intrusive, or igneous. The latter term is used for contacts in plutonic rocks where the units on either side of the contact were interpreted to form part of the same igneous package (e.g., a modal contact between cumulate layers or a grain size contact in a graded sequence).

The term dike refers to any sharp, well-defined, and relatively thick (>1 cm) crosscutting feature formed by injection of magma. This contrasts with igneous vein, which describes a thin (<1 cm) crosscutting feature formed by injection of magma with generally less well defined contacts. Dikes and veins are generally designated as subunits, as described above in [“Igneous units and contact logs.”](#)

## Texture

Textures are defined on the basis of three categories: grain size, grain size distribution, and the relationships between different grains.

Grain sizes were defined as follows:

Glassy.

Cryptocrystalline = <0.1 mm.

Microcrystalline = 0.1–0.2 mm.

Fine grained = >0.2–1 mm.

Medium grained = >1–5 mm.

Coarse grained = >5–30 mm.

Pegmatitic = >30 mm.

For plutonic rocks, grain size distributions are classed as equigranular where all minerals are of similar size and inequigranular where grain size varies significantly. Inequigranular textures are further divided

into seriate (continuous range of crystal sizes), vari-textured (domains with contrasting grain size), or poikilitic (relatively large oikocrysts enclosing smaller crystals, termed chadacrysts, of one or more other minerals). For volcanic rocks, grain size distribution applies to phenocrysts only, using the terms unimodal where all phenocrysts are of similar size, bimodal where they define two size populations, or seriate where they form a continuous range of sizes.

The following terms were used to describe the textural relationships between different silicate grains (Fig. F9):

- Granular: aggregation of grains of approximately equal size.
- Intergranular: coarser grains (typically plagioclase) form a touching framework of the rock with interstices filled by crystalline material.
- Intersertal: coarser touching grains form a framework of the rock with interstices filled by glass.
- Subophitic: partial inclusion of plagioclase in clinopyroxene.
- Ophitic: total inclusion of plagioclase in clinopyroxene.
- Comb structure: comblike arrangement of crystals growing inward from a contact.
- Dendritic: branching arrangement of elongate crystals.

Similar to silicate minerals, the textures of oxide and sulfide minerals are described in terms of grain size and their relationship to adjacent minerals. In plutonic rocks, oxides commonly occur as aggregates, and for grain size determination an aggregate is counted as a single grain.

Layering, where present, is divided into modal layering and grain size layering; when neither term describes the observations well, the term “layering (other)” is used, and the nature of layering is described in the comments. In all cases, the geometry of layering is described as being sharp, gradational, or irregular.

## Thin section descriptions

Each thin section was photographed in both plane-polarized light (PPL) and cross-polarized light (XPL) (see TS\_ORIGINAL\_IMAGES\_335\_335(312) in IMAGES in [“Supplementary material”](#)). Thin section descriptions closely follow the procedure for macroscopic core descriptions. Where a thin section contained areas with different primary (i.e., not alteration-related) lithology, mineralogy, and/or texture, these were defined as domains (e.g., Domain 1, Domain 2, and so on). For thin sections with multiple igneous domains, a map of the domains is shown in

the full thin section photomicrograph (see Fig. F10 for an example). Domains were described separately and their relative abundance was noted.

The following data were recorded and entered into the LIMS database through separate tabs within the Thin Section workbook in DESClogik.

### Lithology and texture

- Rock name (based on thin section observations), using the same definitions as those for macroscopic descriptions.
- Number of igneous domains within the thin section.
- Nature of igneous domains, if any (e.g., contact between two units, mix of two lithologies in one section, or presence of texturally different regions within one thin section).
- Igneous domain relative abundance (in percent).
- Igneous domain number within the thin section (igneous Domain 1, igneous Domain 2, igneous Domain 3, and so on); this parameter identifies each domain described in the mineralogy tab.
- Igneous domain lithology name. If only one domain is present, this is identical to the rock name.
- Igneous domain grain size modal name (glassy, cryptocrystalline, microcrystalline, fine grained, medium grained, coarse grained, or pegmatitic).
- Igneous domain grain size distribution (equigranular, seriate, varitextured, or poikilitic).
- Igneous domain texture (granular, subophitic, ophitic, granophyric, porphyritic, intergranular, intersertal, variolitic, or granoblastic. The latter refers to a fine-grained granular metamorphic texture describing a high-grade metamorphic overprinted, as defined during Expedition 312 [Teagle, Alt, Umino, Miyashita, Banerjee, Wilson, and the Expedition 309/312 Scientists, 2006]).

### Mineralogy

- Igneous domain number: the igneous domains defined in the lithological-textural description.
- Igneous domain mineralogy: abundance (in percent) of primary minerals preserved; estimated abundance (in percent) of primary minerals prior to alteration; computed value of mineral replacement by alteration; minimum size, maximum size, median size, shape, habit, and special features of primary minerals, using the same conventions as during macroscopic description; individual comments for primary minerals; and

absorption colors/pleochroism for clinopyroxene, orthopyroxene, and amphibole.

For plagioclase, a qualifier for zoning was recorded, using the following convention:

- 0 = none.
- 1 = zoning is rare and weakly developed.
- 2 = abundant zoning that can range from weak to strong.
- 3 = nearly ubiquitous, generally strong zoning.

The type of zoning in plagioclase was also documented:

- Continuous: zoning is optically continuous from core to rim.
- Discontinuous: zoning occurs from core to rim, but with distinct break(s).
- Patchy: zoning occurs in patches randomly throughout the grain.
- Oscillatory.

## Geochemistry

During Expedition 335, chemical analyses of representative rock samples were performed using ICP-AES for major and trace element analyses and gas chromatography for CO<sub>2</sub> and H<sub>2</sub>O analyses. An effort toward evaluation of the microbial populations present in Hole 1256D was envisioned, and appropriate samples were to be collected for shore-based analysis. However, sampling was not possible because of limited recovery. Nevertheless, this methodology is described in this section for completeness.

### Sample preparation for geochemistry

Samples were prepared from ~10 cm<sup>3</sup> of rock for gabbro and granoblastic basalt and 50 cm<sup>3</sup> for Sample 335-1256D-Run02-EXJB, a junk basket basalt (see Table T3 in the “Site 1256” chapter [Expedition 335 Scientists, 2012b]). This sample was prepared from roughly 1 cm size gravel by careful separation from the sand, which made up most of the junk basket material. Other samples were cut from cores or from large rock cobbles sampled by junk baskets during fishing runs, using a diamond saw blade. Whenever possible, a thin section billet was taken from the same rock fragment. All outer surfaces were ground on a diamond-impregnated disk to remove saw marks and altered rinds resulting from drilling. Each cleaned sample was placed in a beaker containing isopropanol and ultrasonicated for 15 min. The isopropanol was decanted and the samples were ultrasonicated twice in nanopure deionized water for 10 min. The cleaned pieces were then dried for 10–12 h at 110°C.

The clean, dry whole-rock samples were crushed to <1 cm chips between two disks of Delrin plastic in a hydraulic press. The rock chips were then ground to a fine powder in a tungsten carbide mill in a SPEX 8510 shatterbox. After grinding, a  $5.00 \pm 0.05$  g aliquot of the sample powder was weighed on a Mettler Toledo balance and ignited at  $1025^\circ\text{C}$  for 4 h to determine weight loss on ignition (LOI) with an estimated precision of 0.02 g (0.4%).

The standard shipboard procedure for digestion of rocks and subsequent ICP-AES analysis is described in ODP *Technical Note 29* (Murray et al., 2000). The following protocol is an abbreviated form of this procedure with minor changes and additions.

After determination of LOI,  $100.0 \pm 0.2$  mg aliquots of the ignited whole-rock powders were weighed and mixed with  $400.0 \pm 0.5$  mg of lithium metaborate ( $\text{LiBO}_2$ ) flux that had been preweighed on shore. Standard rock powders and full procedural blanks were included with unknowns in each ICP-AES run. A check on grinding contamination contributed by the tungsten carbide mills was performed during Leg 206 and was found to be negligible for the elements analyzed onboard (Shipboard Scientific Party, 2003). All samples and standards were weighed on the Cahn C-29 microbalance (designed to measure on a moving platform), with weighing errors conservatively estimated to be  $\pm 0.02$  mg.

A 10 mL aliquot of 0.172 mM aqueous LiBr solution was added to the flux and rock powder mixture as a nonwetting agent to prevent the cooled bead from sticking to the crucible. Samples were then individually fused in Pt-Au (95:5) crucibles for ~12 min at a maximum temperature of  $1050^\circ\text{C}$  in a Bead Sampler NT-2100 (internally rotating induction furnace). After cooling, beads were transferred to 125 mL high-density polypropylene bottles and dissolved in 50 mL 10% dilution of concentrated trace metal grade  $\text{HNO}_3$  (thereafter referred to as 10%  $\text{HNO}_3$ ), aided by shaking with a Burrell wrist-action bottle shaker for 1 h. Samples were then ultrasonicated for ~1 h after shaking to ensure complete dissolution of the glass bead. After digestion of the glass bead, the solution was passed through a  $0.45 \mu\text{m}$  filter into a clean 60 mL wide-mouth high-density polypropylene bottle. Next, 1.25 mL of this solution was pipetted into a plastic vial and diluted with 8.75 mL of 10%  $\text{HNO}_3$  to bring the total volume to 10 mL. The final solution-to-sample dilution factor for this procedure was ~4000. Dilutions were conducted using a Brinkman Dispensette. During Expedition 335, stock standard solutions were sonicated for 1 h prior to final dilution and analysis to ensure a homogeneous solution.

## ICP-AES

### Analyses

Major and trace element concentrations of standards and samples were determined using a Teledyne Leman Labs Prodigy ICP-AES instrument. The analyzed elements and the wavelengths used for sample analysis during Expedition 335 are provided in Table T3. Certified international rock reference materials, calibration and drift solutions, and chemical procedure blanks were included with the unknown samples for each sample run. Detection limits (Table T4) were calculated as three times the standard deviation of the mean for blank solution measurements.

The ICP-AES plasma was ignited at least 30 min before each sample run to allow the instrument to warm up and stabilize. After the warm-up period, a zero-order search was performed to check the mechanical zero of the diffraction grating. After the zero-order search, the mechanical step positions of emission lines were tuned by automatically searching with a 0.002 nm window across each emission peak using the BAS-140 standard (basalt interlaboratory standard created during ODP Leg 140 in Hole 504B; Sparks and Zuleger, 1995; Bach et al., 1996) prepared in 10%  $\text{HNO}_3$ . During the initial setup, an emission profile was selected for each peak, using BAS-140, to determine peak-to-background intensities and set the locations of background levels for each element. The Prodigy data acquisition software uses these background locations to calculate the net intensity for each emission line. The photomultiplier voltage was optimized by automatically adjusting the gain for each element using the standard with the highest concentration for that element.

ICP-AES data presented in “Geochemistry” in the “Site 1256” chapter (Expedition 335 Scientists, 2012b) were acquired using the Prodigy software. The intensity curve for each element is defined by 20 measurements within the designated wavelength window. The user selects the two background points that define the baseline. The Prodigy software integrates the area delineated by the baseline and the intensity curve. Each sample was analyzed four times from the same dilute solution within a given sample run. For several elements, measurements were made at two wavelengths (e.g., Si at 250.690 and 251.611 nm) (Table T3). For each run, the wavelength yielding the best calibration line was identified and used for determining concentrations.

A typical ICP-AES run included

- A set of five to seven certified rock standards, chosen for their wide range of compositions, in order to calibrate the analyses (basalt JB-1A, BIR-1, and

BAS-140; granite JG-1A and JG-2; peridotite JP-1; gabbro MRG-1; and pyroxenite ROA-3);

- Up to 20 unknown samples;
- A drift-correcting sample (BAS-140) spiked with Co and analyzed every fourth sample position and at the beginning and end of each run;
- Blank solutions run near the beginning and end of each run; and
- 3 “check” standards chosen for their composition similar to that of the analyzed material (basalts BAS-140 and JB-1A and gabbro MRG1) run as unknowns.

A 10% HNO<sub>3</sub> wash solution was run for 90 s between each sample analysis. Each sample analysis is the average of four measurements. The check standards were used to test analytical accuracy and reproducibility of the obtained data.

### Data reduction for ICP-AES

Following each sample run, raw intensities were transferred to a data file and all analyses were corrected for drift. A drift correction was applied to each element by linear interpolation between drift-monitoring solutions run every fourth analysis. After drift correction, a calibration line for each element was calculated using the results for the certified rock standards. Concentrations used for the calibrations were compiled values from the literature recalculated on a volatile-free basis; compiled values were from Govindaraju (1994) for basalt JB-1A and BIR-1, granite JG-1A and JG-2, peridotite JP-1, and gabbro MRG-1 and from Remaidi (1993) and Sparks and Zuleger (1995), respectively, for laboratory-standards pyroxenite ROA-3 and basalt BAS-140. Element concentrations in the samples were then calculated from the relevant calibration lines.

Estimates of accuracy and precision of major and trace element analyses were based on replicate analyses of check standards, the results of which are presented in Table T4. Run-to-run relative standard deviation by ICP-AES was generally  $\pm 1\%$  for major elements and  $\pm 2\%$  for trace elements. Accuracy was better than 2% for major elements and better than 5% for most trace elements, with the exception of low concentration data for Ni, Sc, and Zn.

### Volatile measurements

Volatile contents were measured using gas chromatography (GC) separations on a Thermo Electron Corporation CHNS analyzer (Flash EA 1112 Series). The procedure was based on methods used during Leg 209 (Shipboard Scientific Party, 2004) and Expedition 304/305 (Expedition 304/305 Scientists,

2006). The samples were splits of powders prepared for ICP-AES and were generally taken near thin section billets. The powders were heated to 110°C for 12 h to remove adsorbed moisture and were stored in a desiccator prior to analysis.

Sample sizes were typically 50 mg. Powders were weighed and packed into tin crucibles and loaded into a carousel autosampler. Samples were then heated at 900°C in a resistance furnace in the presence of oxygen for ~75 s. Nitrogen, hydrogen, carbon, and sulfur released from the sample were oxidized and swept into a separation column (Thermo Scientific Multisep column HaySep-A, P/N 260-079-20) using helium as the carrier gas and then into the thermal conductivity detector. Samples were exposed to a vertically mounted quartz reactor tube containing (in packing order) quartz wool, tungsten(VI) oxide (WO<sub>3</sub>; 0.6–1.68 mm), quartz wool, and reduced Cu (0.7 mm), all inside the resistance furnace. Sulfite gas originating from sulfide minerals was oxidized to SO<sub>2</sub>, and SO<sub>3</sub> was released from any sulfate minerals present in the sample. A single sample analysis required ~20 min. During this time, signal intensity at the detector was continuously recorded, and nitrogen, hydrogen, carbon, and sulfur separated by the GC were measured sequentially at ~71, 103, 399, and 807 s. Once it was established that the hydrogen and sulfur peaks were not completely separated, the use of V<sub>2</sub>O<sub>5</sub> (catalyst for sulfur oxidation) was discontinued, in order to minimize the effect of the sulfur peak on the hydrogen peak (measured as H<sub>2</sub>O). All measurements reported here were run without V<sub>2</sub>O<sub>5</sub>. Because the hydrogen peak was fairly wide (long in duration) and peak heights were quite low, it was deemed necessary to run a blank crucible between all samples, which limited the number of samples that could be run in one carousel. Nitrogen and sulfur contents were not measured because of low levels and poor peak resolution (for sulfur).

### Standards, blanks, and results

Aliquots of 80 mM L-(+)-cysteine hydrochloride ([HSCH<sub>2</sub>CHNH<sub>2</sub>COOH·HCl]·H<sub>2</sub>O at 5, 10, 20, 30, 40, 50, and 60  $\mu$ L) were used for primary calibration of the instrument. Blanks were determined using empty tin crucibles and were typically run between all samples. Concentrations for each sample were calculated from the integrated peak areas of the respective gases relative to those for the standard using a linear regression. Regressions of peak areas versus standard sizes yielded correlation coefficients >0.98. The certified international rock reference material (peridotite) JP-1 (Imai et al., 1995; [georem.mpch-mainz.gwdg.de/](http://georem.mpch-mainz.gwdg.de/)) and the internal laboratory standard BAS-140 were routinely measured to monitor



analytical accuracy and reproducibility. Typical analytical sessions included multiple analyses of each of these standard rocks and duplicates of each unknown sample. Because of instrumental drift and the time duration of each run, it was necessary to run a complete standard curve before each set of samples. Results of the GC analyses for BAS-140 and JP-1 during Expedition 335 are presented in Table T5. Based on nine runs, the reproducibility of JP-1 and BAS-140 was better than 8% for CO<sub>2</sub> and better than 10% for H<sub>2</sub>O. Average CO<sub>2</sub> concentrations obtained for JP-1 overlap published values (Imai et al., 1995) within 5%, and values for BAS-140 are in reasonable agreement with values reported during Expedition 304 (Expedition 304/305 Scientists, 2006). Average H<sub>2</sub>O contents for both BAS-140 and JP-1 are higher than reported and accepted values by ~29%. We attribute the anomalously high values to contamination of the hydrogen peaks by sulfur (and the difficulties in separating the two overlapping peaks) and consider the H<sub>2</sub>O data to be systematically overestimated but include the data in table because the relative abundances may be a guide for future studies. Detection limits, optimistically calculated as three times the standard deviation of all the blank analyses, are 0.01 wt% for CO<sub>2</sub> and 0.02 wt% for H<sub>2</sub>O. In comparing the GC volatile analyses to the LOI results, it is also important to bear in mind that conversion of Fe<sup>2+</sup> to Fe<sup>3+</sup> during ignition may produce a gain in weight that is 11.1% of the percentage of ferrous Fe contained in the sample. This can lead to LOI analyses that have lower volatile concentrations than those determined by GC analysis.

### Microbiology

An effort toward evaluation of the microbial populations present in Hole 1256D was envisioned during Expedition 335, by collecting appropriate samples for shore-based analysis. The goal of these microbiological analyses was to characterize the endolithic microbes associated with the oceanic crust. The specific analytical plan included extraction of DNA and amplification of genes of interest (i.e., 16S rRNA gene and functional genes) for describing microbial community diversity and potential function. The goal was to compare the data to existing studies of microbial life in basaltic oceanic crust on the Juan de Fuca Ridge eastern flank (IODP Expedition 327; Orcutt et al. 2010, 2011). Unfortunately, no samples were collected for microbiology analysis.

### Planned sampling procedure

To determine the extent of contamination from drilling fluid, a solution containing 0.5 μm fluorescent

microspheres is deployed with the core catcher. The solution is prepared by combining nanopure water with 2 mL concentrated microsphere solution (Fluoresbrite, Carboxylate YG; cat. 15700) in a 40 mL volumetric flask. The solution is placed into a small whirlpack bag and tied to the core catcher with the expectation that it will burst with the first recovered core. Beads on the outside of the core indicate dispersion of the microspheres on the external portion of the core; beads detected on the interior of the core indicate the presence of permeable pathways wider than 0.5 μm, suggesting that contamination of the interior of the core may have occurred.

Upon arrival in the core laboratory, a section of the core is evaluated as a potential microbiological sample by visual inspection with minimal handling and before splitting. Handling of the core is limited to those wearing ethanol-rinsed gloves. The scientist in charge of sampling should collaborate with the petrologists to determine a suitable intact sample for microbiological analysis (ideally a ≥10 cm length piece with at least one vein/fracture or signs of alteration). A photograph is taken of the sample before removing it from the core liner. The sample is picked up with a sheet of baked aluminum foil, wrapped in aluminum foil, placed in a sterile whirlpak bag, labeled, and immediately transferred to the -80°C freezer. Following the cruise, the samples are shipped on dry ice.

Details of microbiological sampling and evaluation of contamination is given in Smith et al. (2000).

## Alteration and metamorphism

The characteristics of hydrothermal alteration and contact metamorphism of rocks recovered during Expedition 335 were determined using visual inspection of the core, microscopic thin section descriptions, and X-ray diffraction (XRD) analyses. Visual observations on the core were recorded in the alteration log and the vein and halo log (Tables T6, T7) and are provided as Excel files in DESCLOGIK\_WORKBOOKS\_335 in DESCRIPTIONS in “[Supplementary material](#).” Shipboard observations of alteration and metamorphism were recorded using the DESClogik worksheet interface and uploaded to the LIMS database. Alteration and metamorphism of igneous rocks were described in terms of pervasive background alteration, localized alteration patches (zones of more intense alteration), hydrothermal veins and alteration halos, presence of recrystallized domains (xenoliths of contact metamorphosed rock fragments in gabbro), breccia clasts, and breccia clasts with alteration halos. Each logged

interval may represent multiple pieces or core sections.

## Macroscopic core description

### Background alteration

Alteration textures were recorded in the alteration log, and features were described using the following terms in order to document variations and heterogeneities in alteration style and intensity:

- Pervasive: uniform alteration style and intensity throughout the rock.
- Patchy: pervasive background alteration with local alteration patches.
- Recrystallized: pervasive background alteration where the rocks are recrystallized to granoblastic contact metamorphic assemblages.
- Clasts: breccia clasts enclosed in a matrix of secondary minerals.
- Clasts with halos: breccia clasts that contain alteration halos and are enclosed in a matrix of secondary minerals.

For each alteration textural type, the following features were observed and recorded for background alteration (the entire interval or the host rock for patches and recrystallized domains):

- Color,
- Percentage of rock altered to secondary phases,
- Percentage of each primary mineral replaced, and
- Secondary minerals replacing primary minerals.

For each textural category, the volume percentage of alteration was estimated and classified using the following scale:

- Fresh = <2% by volume alteration products.
- Slight = 2%–9%.
- Moderate = 10%–49%.
- High = 50%–95%.
- Complete = >95%.

The following data were recorded for patchy textural intervals:

- The pervasive background alteration information for the rock hosting the patches (as above);
- The size (<1, 1–3, or >3 cm), shape (round, irregular, elongate, or network), and area percentage of patch in the rock or interval;
- The total percentage of alteration (secondary phases) in the patches; and
- The primary mineral alteration and secondary phases present (as in the background alteration).

Recrystallized alteration texture comprises pervasive background alteration where the rock is recrystallized to granoblastic contact metamorphic assem-

blages (based on examination of thin sections and previous work) (Teagle, Alt, Umino, Miyashita, Banerjee, Wilson, and the Expedition 309/312 Scientists, 2006; Koepke et al., 2008; France et al., 2009; Alt et al., 2010). For recrystallized intervals, background alteration was recorded as described above for pervasive background alteration. Recrystallization degree was classified on a scale from 0 to 6, based on the classification from Teagle, Alt, Umino, Miyashita, Banerjee, Wilson, and the Expedition 309/312 Scientists (2006) (Fig. F11). Recrystallization begins with the growth of isolated micrometer-sized pyroxene granules replacing clinopyroxene and developing as small inclusions in clinopyroxene and reaches “partial” replacement where the igneous texture begins to disappear because of recrystallization to granular pyroxene. Samples were classified as strongly recrystallized if all minerals are replaced but the igneous texture is not completely erased. In completely recrystallized samples, the igneous texture is obliterated and overprinted by an equigranular granoblastic assemblage of secondary pyroxene, plagioclase, ilmenite, and magnetite.

Xenoliths of dike rock are variably recrystallized to granoblastic contact metamorphic assemblages and were described as recrystallized domains. The abundance of these was estimated, and the pervasive background alteration of the host rock was recorded as described above.

An alteration and metamorphism summary description was entered in DESClogik so it could be added to the VCDs. The alteration intensity plotted on the VCDs corresponds to the background alteration intensity. The VCDs also contain a summary statement of the alteration characteristics for each unit in a section.

### Veins and alteration halos

The frequency of veins per 10 cm interval of core was recorded in the alteration log as vein density on a scale of 0 to 5:

- 0 = no veins,
- 1 = <1 vein per 10 cm,
- 2 = 1–5 veins per 10 cm,
- 3 = 6–10 veins per 10 cm,
- 4 = 11–20 veins per 10 cm, and
- 5 = >20 veins per 10 cm.

For each vein, the depth interval, width, attitude (vertical or inclined), connectivity, boundary (diffuse or sharp), and color and mineralogy (with each mineral estimated as a percentage of the vein) were recorded in the vein and halo log. The classification used for vein connectivity is shown in Figure F6. The orientations of veins in oriented core pieces were sys-

tematically measured (see “[Structural geology](#)”). Alteration halos representing zones of increased alteration adjacent to veins were described by width, color, and secondary mineral percentages in the Halo comments column of the vein and halo log. Vein nets and breccia were recorded on the vein and halo log in the Alteration feature column, noting the depth interval, total volume percent secondary minerals, and percentages of individual secondary phases. Breccia clasts were to be described in the alteration log, but such features were not encountered in the Expedition 335 cores.

### Thin section description

Thin sections of basement rocks recovered during Expedition 335 were examined to confirm macroscopic identifications of secondary minerals and establish the distribution, occurrence, and abundance of secondary minerals with depth in the core. The amount of alteration/recrystallization was determined, along with the mode of occurrence of vesicle and void fillings, vein composition, and primary mineral replacement. Chronological relationships between different secondary minerals or parageneses were recorded.

Data were recorded in the thin section log in DESClogik for each alteration domain present within a thin section, including background, patch, recrystallized domain, and vein. Data recorded for each secondary mineral present include

- Estimates of secondary mineral percentage,
- The primary mineral(s) replaced, and/or
- Texture as a comment.

Digital photomicrographs were taken to document features described in thin sections. A summary description was entered in DESClogik so it could be added to the thin section report. The recrystallization degree (from 0 for not recrystallized to 6 for complete recrystallization; details are given in Fig. [F11](#)) was also added in the thin section log.

### X-ray diffraction

Phase identification of whole rocks, patches, or vein material was aided by XRD analyses using a Bruker D-4 Endeavor diffractometer with a Vantec-1 detector using nickel-filtered  $\text{CuK}\alpha$  radiation. XRD was performed on small amounts of powder (usually ~20 mg) as smear slides or pressed onto sample holders. Instrument conditions were

Voltage = 40 kV.

Current = 40 mA.

Goniometer scan (bulk samples)  $2\theta = 4^\circ\text{--}70^\circ$ .

Step size = 0.0087°.

Scan speed = 0.2 s/step.

Divergence slit = 0.3°, 0.6 mm.

## Structural geology

This section outlines the techniques used for macroscopic and microscopic description of structural features observed in Hole 1256D igneous rocks. During Expedition 335, scientists generally followed the same conventions for structural studies used during Expeditions 304/305 (Expedition 304/305 Scientists, 2006) and 309/312 (Expedition 309/312 Scientists, 2006), which were based on previous ODP hard rock drilling legs (118, 131, 135, 140, 141, 147, 148, 153, 176, 206, 209; Shipboard Scientific Party 1989, 1991, 1992a, 1992b, 1992c, 1993a, 1993b, 1995, 1999a, 1999b, 2003, 2004). Definitions of structural measurements and descriptive parameters, along with corresponding description dictionaries, were further refined as part of the process of configuring the new core description software application DESClogik for hard rock descriptions. DESClogik was used to enter and upload the information into the LIMS database (see “[Information architecture](#)”). Details specific to structural features were illustrated with comments and sketches in STRUCTURE\_SKETCHES\_335 in DESCRIPTIONS in “[Supplementary material](#).”

Expedition 312 plutonic cores were redescribed using the same techniques and methods to ensure consistency in descriptions of Hole 1256D plutonic rocks (see STRUCTURE\_LOGS\_312\_335 in DESCRIPTIONS in “[Supplementary material](#)”). An attempt was made to restore orientations of important structures into the geographic reference frame using available paleomagnetic data (see “[Structural restoration: geographic reorientation](#)”), and obtained orientations were recorded to generate a coherent data set for the Hole 1256D plutonic section (see STRUCTURE\_LOGS\_312\_335 in DESCRIPTIONS in “[Supplementary material](#)”).

### Structural measurements

Structural features, categorized as magmatic, crystal-plastic, and brittle, were logged in centimeters from the top of each section. Descriptions of all features were recorded using curated depths so that “structural intervals” could be correlated with lithologic core descriptions. Depth intervals of structures were recorded as the distance from the top of the section to the top and bottom of the feature. Depth to a midpoint of a structure was recorded for the structures with measurable width, such as veins or intervals with a magmatic foliation.

Structures on the archive half were measured relative to the standard IODP CRF (see “[Core reference](#)”).

**frame for sample orientation”** Fig. F2). The plane normal to the axis of the borehole is referred to as the horizontal plane. On this plane, a 360° net is used with pseudosouth (180) pointing into the archive half and pseudonorth (000) pointing out of the archive half (Fig. F12). The cut surface of the core, therefore, is a vertical plane striking 090–270.

Apparent dip angles of planar features were measured on the cut face of the archive half of the core. To obtain a true dip value, a second apparent dip reading was obtained, where possible, in a section perpendicular to the core face (second apparent orientation, middle diagram, in Fig. F12). The two apparent dips and dip directions (or one apparent direction combined with the strike) measured for each planar feature were used to calculate the dip and dip direction in the core reference frame. If the feature intersected the upper or lower surface of the core piece, measurements of the strike were made in the core reference frame, recorded as the trend (strike) of a line with zero dip angle, and combined with an apparent dip measurement, measured on the cut surface of the core, to calculate the true dip value (right sketch in Fig. F12). If a feature was exposed on the surface of the core (i.e., a fracture defining the top or bottom of a piece), the true dip and dip azimuth were measured directly on the feature with no need for another measurement or a calculation (not illustrated). True dip and dip direction (azimuth) were calculated using the Stereonet plotting program developed by Allmendinger ([www.geo.cornell.edu/geology/faculty/RWA/programs/](http://www.geo.cornell.edu/geology/faculty/RWA/programs/)) and then imported into DESClogik.

### Macroscopic core description and terminology

We examined all material from both the working and archive halves. Sketches of structures and orientation measurements were made from the archive half, but observations on working-half pieces were also made for certain features that were better exposed on the working half. For each section, detailed structural information was described and sketched on handwritten forms and subsequently entered into Excel spreadsheet logs, as described above. This information was then input into the DESClogik framework. The sketches were scanned and are archived in STRUCTURE\_SKETCHES\_335 in DESCRIPTIONS in **“Supplementary material.”**

The DESClogik workbooks contain data on location, types of structures, their intensity, and orientations. We separated the structural data into three categories:

1. Magmatic fabrics,
2. Crystal-plastic fabrics, and
3. Brittle structures (faults and fractures).

Other structural features not included in the structure workbook include contacts and veins. Magmatic structures and textures, including igneous contacts, compositional banding, and textural banding were described and their orientations recorded in the Contacts and the Texture tab in the igneous petrology workbook (see **“Igneous petrology”**) using the method described above. Veins, defined here as fractures filled with secondary minerals, were described and their orientations recorded in the Veins and Halos tab in the metamorphic petrology workbook (see **“Alteration and metamorphism”**). The most representative and/or prominent structural features in the cores recovered during Expedition 335 are plotted on the VCDs. These are intensity of magmatic and crystal-plastic fabric alignment; density of brittle fractures; and precise locations of observed prominent structures, such as igneous contacts, magmatic banding and magmatic veins (see **“Igneous petrology”**), veins, vein networks, hydrothermal breccia (see **“Alteration and metamorphism”**), cataclastic zones, breccia, shear veins, faults, fractures (except for horizontal irregular fractures; see **“Brittle deformation”**), and folds, where recognizable.

Short explanations for terms and abbreviations used in the respective categories are given below. We followed the terminology based on Ramsay and Huber (1983), Twiss and Moores (1992), Davis (1984), and Passchier and Trouw (1996).

### Magmatic fabrics

Magmatic fabrics were defined macroscopically by shape-preferred orientation (SPO) of primary minerals with no evidence of crystal-plastic deformation. Descriptions of magmatic fabric include the following:

- Symmetry of magmatic fabric: linear (L), planar (S), planar-linear (L-S), or nondetectable.
- Magmatic fabric intensity accompanied by intensity rank: (0) isotropic, (1) weak, (2) moderate, or (3) strong (Fig. F13).
- Sense of shear: normal (n), reverse (r), dextral (d), sinistral (s), or a combination of these (nd, ns, rd, or rs).
- Comments: name and general shape of fabric elements were described together with crosscutting relationships, shape and boundary features (i.e., planar, curved, or irregular), and anything else of interest.



- SPO of mineral phases or groups of mineral phases with modal percent of measured mineral phases, shape ratio, and orientation of SPO long axis (see “[Quantitative shape-preferred orientation analysis](#)”).
- Orientation (dip azimuth and dip angle of planar fabric, as well as trend and plunge of lineation, where measurable) of magmatic fabric.

### Crystal-plastic fabrics

Crystal-plastic fabrics (CPFs) are lineations or foliations defined by grains exhibiting plastic strain. Descriptions for CPFs include the following:

- Symmetry: linear (L), planar (S), planar-linear (L-S), or nondetectable.
- Intensity accompanied by intensity rank: (0) undeformed, (1) weakly foliated/lineated, (2) strongly foliated/lineated, (3) porphyroclastic/protomylonitic, (4) mylonitic, or (5) ultramylonitic (Fig. [F13](#)).
- Boundary geometry (i.e., shear zone boundary): planar, irregular, curved, concordant, or discordant.
- Boundary sharpness: sharp or diffuse.
- Sense of shear: normal (n), reverse (r), dextral (d), sinistral (s), or a combination of these (nd, ns, rd, or rs).
- Comments: name and general shape of minerals that define CPFs together with crosscutting relationships, spacing, shape features, and anything else of interest.
- SPO of mineral phases or groups of mineral phases with modal percent of measured mineral phases, shape ratio, and orientation of SPO long axis (see “[Quantitative shape-preferred orientation analysis](#)”).
- Orientation (dip azimuth and dip angle of planar fabric, as well as trend and plunge of lineation, where measurable).

### Quantitative shape-preferred orientation analysis

Quantitative SPO analysis of plagioclase-rich leucocratic patches was applied to Expedition 312 Gabbro 1, where grains were recognizable in close-up photographs.

SPO analysis involves three successive processes: image acquisition, image processing, and image analysis:

1. Image acquisition: close-up photographs of wet archive-half cores were taken with a digital camera at 300 dpi, a focal length of 50 mm, and a

ruler scale in centimeters; analyzed pieces were oriented and free of veins and fractures.

2. Image processing: rectangular digital images in JPEG format were processed using Photoshop CS 4 and the following three successive steps (Fig. [F14](#)): (a) convert image to gray scale, (b) threshold image at digital number (DN) = 60, and (c) invert to binary, 1-bit monochrome image so that objects of interest (i.e., plagioclase grains) are black on a white background.
3. Image analysis: analysis of the 1-bit image was performed using the Intercepts software, 2003 version (Launeau et al., 1990, 2010; Launeau and Robin, 1996). Software settings are given in Figure [F15](#).

The main results of SPO analysis are the modal percentage of the analyzed phase, the shape ratio of the SPO ellipse, and the angle between the ellipse long axis and core axis, recorded in a clockwise sense from the core face.

The current SPO methodology provides consistent results when SPO shape ratio > 1.01. Specimens with shape ratio < 1.01 were thus considered methodologically isotropic, and those with shape ratio > 1.01 were considered methodologically anisotropic. Practically, magmatic and crystal-plastic fabrics are macroscopically visible only when shape ratio > 1.05. When compared to the intensity of macroscopic fabric alignment (magmatic or crystal plastic), specimens are ranked as follows:

- Specimens with SPO shape ratio  $\leq 1.05$  are regarded as macroscopically isotropic (rank 0),
- Specimens with  $1.05 < \text{SPO shape ratio} \leq 1.2$  are regarded as weak (rank 1),
- Specimens with  $1.2 < \text{SPO shape ratio} \leq 2.0$  are regarded as moderate (rank 2), and
- Specimens with SPO shape ratio > 2.0 are regarded as strong (rank 3).

### Brittle deformation

In the Brittle deformation tab, we described and measured features including faults, defined as fractures with shear displacement, and joints, defined as fractures with no shear displacement. We used fracture as a general term, indicating brittle failure with or without displacement. Microfault was used when describing faults with <1 mm of related width of deformation or faults with displacement measurable at core scale. Shear veins, defined here as fractures with secondary mineralization and a recognizable shear sense (such as slickenlines and fibrous mineral growth), were logged independently in the Brittle deformation tab, with orientation of slickenlines and sense of shear, where measurable. Orientations of

open fractures that occur along the broken surface of veins were also recorded in the Brittle deformation tab rather than in the Vein tab. Descriptions for the Brittle deformation tab include the following:

- Semibrittle versus brittle classification: any feature involving both brittle and crystal-plastic deformation (i.e., melt-filled fractures).
- Type of fault rock: fault gouge, fault breccia (for noncohesive rocks), cataclasite, hydrothermal breccia, magmatic breccia, or pseudotachylite. Microfault and shear veins were also identified here. The type of fault rocks may be accompanied by identifiers describing fabric alignment such as foliation and lineation.
- Clast/matrix ratio (in percent).
- Sense of shear: normal (n), reverse (r), dextral (d), sinistral (s), or a combination of these (nd, ns, rd, or rs).
- Fault offset (in millimeters) where measurable.
- Trend and plunge of slickensides/slickenlines/slickenfibers.
- Intensity of cataclastic deformation and intensity rank: (0) undeformed, (1) minor fracturing with no significant grain size reduction, (2) moderate fracturing without grain size reduction, (3) dense anastomosing fracturing with incipient grain size reduction, (4) well-developed grain size reduction with evidence for clast rotation (independent particulate flow), or (5) cataclastic (Fig. F13).
- Density (count per 10 cm) of subhorizontal (<20°) irregular fractures with density scale: (0) no fracture, (1) <2 fractures per 10 cm, (2) 2–5 fractures per 10 cm, or (3) >5 per 10 cm or rubble.
- Density of fractures (except for subhorizontal irregular fractures) with density scale: (0) no open fracture, (1) <1 fracture per 10 cm, (2) 1–5 fractures per 10 cm, or (3) >5 fractures per 10 cm.
- Fracture morphology: planar, curved, concave, irregular, stepped, splayed, anastomosing, or Riedel array (Fig. F16).
- Fracture thickness (in millimeters): closed fracture/joint has 0 mm thickness by definition.
- Comments: crosscutting relationships and morphology of termination of fracture.
- Orientation (dip azimuth and dip angle) of fracture and trend and plunge of associated lineation.

Subhorizontal irregular fractures are identified as irregular or concave, horizontal to subhorizontal (<20°) fractures, without secondary mineralization, at the piece ends and/or confined in a piece, and

may be related to drilling-induced fracture or pre-existing anisotropy of the rocks.

## Microstructures

To better characterize different types of deformation, we studied the microstructural features of interesting and/or prominent mesoscopic structures. Thin sections of recovered material were examined in order to

- Confirm macroscopic descriptions of structures,
- Characterize the microstructure of the rocks,
- Document crystal-plastic overprints of magmatic fabrics,
- Provide information on the kinematics of brittle and brittle-ductile deformation,
- Identify temporal relationships between magmatic and crystal-plastic deformation and alteration processes, and
- Document major structural zones and downhole variations.

For descriptions of microstructures, the terminology of Passchier and Trouw (1996) was used. Shipboard thin sections were oriented; the orientation is given relative to the core reference frame and was marked on each thin section (Fig. F2). Marking two directions is necessary to achieve unambiguous orientation of thin sections cut parallel to the cut surface of the core. Orientation of structures measured during the macroscopic core description was confirmed, and macroscopic observations were refined by the microscopic description. Digital photomicrographs and sketches were taken and annotated to document features described in thin sections (see STRUCTURE\_SKETCHES\_335 in DESCRIPTIONS in “[Supplementary material](#).” Microstructural notes were entered into the Structures tab in the thin section workbook of DESClogik.

Structural domains were introduced into the Structural tab in the thin section workbook. Several terms were introduced in the macroscopic descriptions, such as “bands” and “patches,” that might have different deformation mechanisms in different parts of a thin section. These terms are nongenetic and are meant to describe inhomogeneous distributions of phases and aggregates of phases. Such inhomogeneous distributions of phases were separated into structural domains for the documentation of microstructures and described separately.

We generally followed terminology used during Expedition 312 (Expedition 309/312 Scientists, 2006). Additional classifications and terminology were incorporated from Legs 153, 176, and 209 and Expedi-

tion 304/305 (Expedition 304/305 Scientists, 2006). In the Structure tab of the thin section description workbook, we described the following microscopic features for each structural domain:

- Type of microstructure: magmatic, submagmatic, crystal plastic, cataclastic, or metamorphic.
- Morphology of grain boundary: straight, curved, serrate, polygonal, complex, or varied.
- Intensity of magmatic fabric: isotropic, weak, moderate, or strong.
- Intensity of static recrystallization: absent, weak, strong, partial, or complete.
- Presence of submagmatic fracture: absent, rare, or common.
- Intensity of crystal-plastic undulose extinction: absent, weak, moderate, strong, complete, patchy, or subgrains.
- Morphology of crystal-plastic subgrain boundaries: straight, curved, serrate, or polygonal.
- Presence of crystal-plastic deformation twinning: absent, rare, or common.
- Intensity of crystal-plastic dynamic recrystallization: absent, weak, strong, or complete.
- Intensity of overall crystal-plastic fabric with intensity rank: (0) absent, (1) weakly foliated/lineated, (2) strongly foliated/lineated, (3) porphyroclastic/protomylonitic, (4) mylonitic, or (5) ultramylonitic. Sense of shear estimated from crystal-plastic fabric: normal (n), reverse (r), dextral (d), or sinistral (s).
- Clast/matrix ratio (in percent) of cataclasite/brittle fracture.
- Size (in millimeters) of clasts in cataclasite/brittle fracture.
- Intensity of cataclastic fabric and intensity rank: (0) undeformed, (1) minor fracturing with no significant grain size reduction, (2) moderate fracturing without grain size reduction, (3) dense anastomosing fracturing with incipient grain size reduction, (4) well-developed grain size reduction with evidence for clast rotation (independent particulate flow), or (5) cataclastic.

### Additional work on Hole 1256D plutonic section

#### Structural restoration: geographic reorientation

We attempted to azimuthally reorient structures into the geographic reference frame using a compilation of paleomagnetic data consisting of Expedition 335 shipboard data and unpublished Expedition 312 postcruise data of R. Anma and D.S. Wilson (See “Paleomagnetism” in the “Site 1256” chapter [Expedition 335 Scientists, 2012b]). Stable endpoint

remanence directions determined using principal component analysis (PCA) may be used to perform a first-order reorientation of structures in individual core pieces by making the following assumptions: (1) the sampled section records a normal polarity remanence, (2) the stable remanence for each core piece approximates the time-averaged geomagnetic field direction at the site at the time of accretion, and (3) no significant tilting of the section has occurred. Structures may then be reoriented by applying a simple rotation to core pieces around the axis of the hole to align piece declinations with north. The first assumption is supported by General Purpose Inclination Tool (GPIT) data (see Teagle, Alt, Umino, Miyashita, Banerjee, Wilson, and the Expedition 309/312 Scientists, 2006) that indicate normal polarity of the plutonic section and by U-Pb ages of Gabbro 1 (15.04 Ma  $\pm$  0.18 m.y. and 15.06 Ma  $\pm$  0.37 m.y.; R. Anma, unpubl. data) that coincide with normal polarity Chron C5Bn.2n (15.034–15.155 Ma; Cande and Kent, 1995). However, Gabbro 2 yielded a U-Pb age of 15.20 Ma  $\pm$  0.17 m.y. (R. Anma, unpubl. data), falling within reversed polarity Chron C5Br (15.155–16.014 Ma; Cande and Kent, 1995). We note that assuming a reversed polarity (i.e., original south declination) in the restoration process would reverse the dip direction of restored structures but would not affect their restored strike.

#### Magnetic susceptibility measurements on split core

To support the delineation of magmatic fabric units, a series of magnetic susceptibility measurements were made on split cores. These measurements were performed using the Bartington MS2 magnetic susceptibility meter and the surface probe MS2F, which has a measuring volume equivalent to a half sphere of 40 mm diameter (see “Physical properties”). Measurements were performed on the center of fresh pieces, chosen to be as homogeneous, representative, and free of veins as possible. Measurements were taken at an average spacing of 50 cm depending on core recovery. The values are given in  $10^{-5}$  (SI).

### Paleomagnetism

During Expedition 335, routine shipboard paleomagnetic and magnetic anisotropy experiments were carried out. Remanent magnetization was measured on archive section halves and on discrete cube samples taken from the working halves. Continuous archive section halves were demagnetized in an alternating field (AF), whereas discrete samples were subjected to either stepwise AF demagnetization, thermal demagnetization, or a combination of low-temperature de-

magnetization followed by either AF or thermal treatment. Given the low recovery during Expedition 335, experiments were also conducted on a suite of discrete samples cut from gabbroic rocks recovered during Expedition 312. Because the azimuthal orientations of core samples recovered by rotary drilling are not constrained, all magnetic data are reported relative to the sample core coordinate system. In this system,  $+x$  points into the working section half (i.e., toward the double line),  $+z$  is downcore, and  $+y$  is orthogonal to  $x$  and  $z$  in a right-hand sense (Fig. F2).

## Archive section half remanent magnetization data

### Measurement and filtering

The remanent magnetization of archive section halves was measured at 2 cm intervals using the automated pass-through direct-current superconducting quantum interference device (DC-SQUID) cryogenic rock magnetometer (2G Enterprises model 760R). An integrated inline AF demagnetizer (2G model 600), capable of applying peak fields up to 80 mT, was used to progressively demagnetize the core. Demagnetization was conducted in 5 mT steps up to 80 mT, but data from demagnetizations above 60 mT were found to be contaminated by instrument-induced anhysteretic magnetization and were discarded.

With strongly magnetized materials, the maximum intensity that can be reliably measured (i.e., with no residual flux counts) is limited by the slew rate of the sensors. At a track velocity of 2 cm/s it is possible to measure archive section halves with a magnetization as high as  $\sim 10$  A/m (Expedition 304/305 Scientists, 2006; Expedition 330 Scientists, 2012). Although the baseline values measured just prior to and just after the archive section half measurements are not saved in the database, the baseline drift, and thus the number of residual flux counts, can be determined indirectly from the archived directional data. We used LabView software developed by Jeff Gee (WebTabularToMag; Expedition 330 Scientists, 2012) to reconstruct the baseline drift, allowing the residual flux counts to be logged while converting the data for further processing.

The compiled version of the LabView software (SRM\_SAMPLE) used during Expedition 335 is SRM version 318. This incorporates two modifications to the program and the Galil motor system (Expedition 330 Scientists, 2012). First, the speed at which the archive section was moved when not measuring has been increased to 20 cm/s. Second, simultaneous sampling of the magnetometer axes has been incor-

porated into the magnetometer software. During Expedition 330, these changes together resulted in substantial time savings (on the order of 0.5 h per section with 6–8 demagnetization steps) and also allowed multiple measurements at each interval for weakly magnetized cores. Hence, these modifications have been retained for Expedition 335.

The response functions of the pick-up coils of the DC-SQUID sensors have a full width of 7–8 cm at half height (Parker and Gee, 2002). Therefore, data collected within  $\sim 4$  cm of piece boundaries (or voids) are significantly affected by edge effects. Consequently, data points within 4.5 cm of piece boundaries (as documented in the curatorial record) were filtered out prior to further processing. To further reduce artifacts, any pieces smaller than 10 cm were removed from section trays prior to measuring/demagnetizing and replaced afterward.

Remanent magnetization directions were calculated for each 2 cm measurement using PCA (Kirschvink, 1980). Note that the intensity reported for such PCA directions represents the length of the projection of the lowest and highest treatment vectors used in the PCA calculation onto the best-fit direction. Because the origin is not included in the PCA calculation and the remanence remaining after the highest treatment may be significant, resulting ChRM intensity values will be systematically lower than those derived from the remanence at the lowest demagnetization step adopted for the PCA calculation.

## Discrete sample data

### Measurement and instrumentation

All discrete samples taken from working-half cores for shipboard magnetic analysis were 8 cm<sup>3</sup> cubes. Although standard 2.5 cm diameter minicores are more commonly used, cubic samples were preferred, as they should have a more precisely determined vertical reference (based on a saw cut perpendicular to the core length) than the minicores, where the fiducial arrow on the split-core face must then be transferred to the long axis of the sample. For core sections recovered during Expedition 335, discrete samples for shipboard analysis were severely restricted by the limited number of oriented core pieces (i.e., those where the way up of the piece is known unambiguously). Samples from the legacy working-half cores from Expedition 312 were likewise limited by the degree of sample depletion of oriented pieces resulting from extensive postcruise sampling by the scientific community.

Remanent magnetization of discrete samples was measured exclusively with the JR-6A spinner magnetometer, following tests of the reliability of discrete



measurements on the 2G superconducting rock magnetometer (SRM) that showed significant scatter in remanence directions measured in different sample orientations (see “[Reliability of discrete sample measurements using the 2G superconducting rock magnetometer](#)”). For samples measured on the spinner magnetometer, the automated sample holder was used, providing the most accurate discrete sample remanent magnetization directions and intensities. Measurements of the empty automatic sample holder after subtracting the stored holder magnetization yielded intensities on the order of  $4.0 \times 10^{-6}$  A/m, representing the practical noise limit of the system.

Discrete samples were subjected to stepwise AF demagnetization using the DTech AF demagnetizer (model D-2000), capable of peak fields up to 200 mT. Fourteen AF demagnetization steps were used, with 5 mT steps up to 40 mT and 10 mT steps up to a maximum peak field of 100 mT. The residual magnetic field at the demagnetizing position in this equipment was ~25 nT.

Discrete samples were thermally demagnetized using a Schonstedt Thermal Demagnetizer (model TSD-1), capable of demagnetizing samples up to 700°C. The total magnetic field along the length of the TSD-1 access tube is illustrated in Figure F17, demonstrating that the sample cooling chamber between 68 and 106 cm (measured from the outside of the access door) has a maximum field of <20 nT. Each sample boat for thermal demagnetization included as many as nine samples, and sample orientations were varied at alternative steps to allow any interaction between adjacent samples to be identified. Samples were held at the desired temperature for 40 min prior to cooling in the low-field chamber. Magnetic susceptibility was measured (using a Bartington MS2F point magnetic susceptibility meter) after every heating step to monitor thermal alteration of magnetic minerals during heating.

A subset of discrete samples was subjected to low-temperature demagnetization (Merrill, 1970; Dunlop, 2003; Yu et al., 2003) prior to subsequent AF or thermal demagnetization in order to test the efficiency of low-temperature demagnetization in removing substantial secondary drilling-related magnetizations. Low-temperature demagnetization involves cooling samples in a liquid nitrogen bath ( $T = 77^\circ\text{K}$ ) and allowing them to warm back up to room temperature in a very low-field environment. This cools the samples to below the Verwey transition of magnetite (Dunlop, 2003), resulting in a loss of magnetic remanence by multidomain grains upon subsequent warming to ambient temperature. This technique was employed in shore-based paleomagnetic

analysis of discrete samples from gabbroic rocks recovered from Atlantis Massif in IODP Hole U1309D (Morris et al., 2009) and successfully removed a large proportion of the drilling-related magnetization that is presumed to be carried by coarse, multidomain magnetite grains. During shipboard experiments, a suitable low-field environment was provided by a three-layer cylindrical mu-metal shield with removable end caps. Precise measurement of the field inside the shield was difficult to achieve because the cable from the three-axis fluxgate magnetometer probe prevents the end caps from being fitted tightly to the shield. Nevertheless, holding the three end caps in place manually indicated that the internal field is <25 nT (with a ship orientation of  $230^\circ$  and shield long-axis orientation of  $\sim 320^\circ$ ). This was sufficiently low to allow the low-temperature demagnetization treatment to be performed successfully.

### Reliability of discrete sample measurements using the 2G superconducting rock magnetometer

The large-aperture 2G SRM is designed principally to measure the magnetization of whole-core and section half samples. Measurements of discrete samples on the SRM are known to be affected by factors such as the alignment of the DC-SQUID sensors and discrete sample tray (Shipboard Scientific Party, 2004) and inhomogeneity in sample shape or in the distribution of remanence carriers. Uncertainties in the reliability of SRM discrete sample measurements were highlighted during Expedition 330 (Expedition 330 Scientists, 2012) using a suite of reference samples previously analyzed at the Scripps Institution of Oceanography. Here we further assess the reliability of discrete measurements made in different SRM sample positions across a range of intensities of magnetization. The SRM discrete measurement software allows all 24 possible orientations of a cubic sample (relative to the DC-SQUID axes) to be measured in turn. We used this capability to repeatedly measure anhysteretic remanent magnetizations (ARMs) imparted in different directions on a set of seven previously demagnetized samples (using AF demagnetization to stepwise decrease ARM intensities between four measurement runs). At each intensity level, samples were measured in the full set of 24 SRM positions. To provide an independent determination of the direction and intensity of remanence at each level, samples were also measured using the AGICO JR-6A spinner magnetometer using the automatic three-position holder and high (87.7 rev/s) rotation speed. Repeat measurements with this instrument showed <1° directional variability and <1% intensity variability. In addition, the practical noise

level of the JR-6A during shipboard operations ( $4.0 \times 10^{-6}$  A/m) was at least one order of magnitude lower than that of the SRM ( $4.4 \times 10^{-5}$  to  $9.6 \times 10^{-5}$  A/m). Hence the JR-6A determinations provide suitable reference directions to compare with the SRM measurements.

Results for six samples are shown in the equal area stereographic projections in Figure F18 (the seventh sample was magnetized along its z-axis and is omitted for clarity). The variation of circular standard deviation (CSD) with remanence intensity for all samples is shown in Figure F19. In order to allow visual comparison of the resulting distributions at each remanence level, SRM data (black symbols in Fig. F18) have been rotated around a vertical axis to align the JR-6A reference directions with azimuths of  $045^\circ$ ,  $135^\circ$ ,  $225^\circ$ , and  $315^\circ$  in decreasing order of remanence intensity (red triangles in Fig. F18). At all intensity levels there is considerable scatter in remanence directions and intensities across the 24 measuring positions. Even when intensities are of the order of 1 A/m, averaging of data from multiple positions is required to yield directions of magnetization within  $2^\circ$  of the JR-6A reference values for all samples. Orientation-related scatter increases dramatically with decreasing intensity, becoming extreme at intensities  $< 20$  mA/m (with CSD values  $> 10^\circ$ , reaching a maximum of  $56^\circ$ ). Such intensities are routinely encountered at high treatment levels during demagnetization experiments (and as natural remanent magnetization intensities in sedimentary rocks). Given the uncertainties in determining remanence directions demonstrated by this experiment and the need for multiple measurements to provide meaningful results even at high intensities, it is clearly preferable to use the AGICO JR-6A system for discrete sample analyses.

### Anisotropy of low-field magnetic susceptibility

In addition to standard paleomagnetic measurements, the anisotropy of low-field magnetic susceptibility was determined for all discrete samples using the KLY 4S Kappabridge with the software AMSSpin (Gee et al., 2008). The susceptibility tensor and associated eigenvectors and eigenvalues were calculated offline following the method of Hext (1963). All bulk susceptibility values reported for discrete samples are based on a sample volume of  $8 \text{ cm}^3$ .

### Inclination-only analysis

For azimuthally unoriented cores, the simple arithmetic mean of inclination data will be biased to shallower values (e.g., Kono, 1980; McFadden and Reid, 1982; Arason and Levi, 2010). To compensate for this

bias, we have used the inclination-only statistics of Arason and Levi (2010) to calculate the overall mean inclination for the cored interval and appropriate subintervals.

Although the Arason and Levi technique is more robust than previous inclination-only methods (e.g., Kono, 1980; McFadden and Reid, 1982), this technique nonetheless fails to converge under certain circumstances. For example, if inclinations are steep and the scatter is substantial or if dual polarities (also with steep inclination) are present, no maximum likelihood estimate is possible. Hence this method is unsuitable for analysis of steep drilling-induced magnetization.

## Physical properties

Shipboard measurements of physical properties were undertaken to characterize recovered core material and other rocks. These data are used to link the geological observations made on the core to the results of downhole logging and regional geophysical survey results (seismic profiles, magnetic surveys, and so on).

Prior to physical property measurements, whole-round cores were allowed to thermally equilibrate for 4 h to ambient room temperature.

All core sections were run through the Whole-Round Multisensor Logger (WRMSL) to measure gamma ray attenuation (GRA) density and magnetic susceptibility. The Natural Gamma Radiation Logger (NGRL) was used to measure gamma radiation for whole-round sections. We also applied a filter to remove data acquired from gaps and cracks between core pieces (e.g., magnetic susceptibility data plot in the VCDs), the process of which is described in detail below (see “Data filtering”). We did not use the *P*-wave logger on the WRMSL, as these measurements require full-diameter core and good coupling to the liner. This is generally not the case for hard rock cores.

Following whole-round measurements and core splitting, the archive half of the core was passed through the Section Half Multisensor Logger (SHMSL) for measurement of magnetic susceptibility with a Bartington MS2E1 contact sensor probe and color reflectance with an Ocean Optics photospectrometer. The SHMSL uses a laser to record piece heights, which can locate gaps and cracks between pieces of the core. These laser profile data, together with GRA density data, were used to filter whole-round and split-half measurements (see “Data filtering”).

Thermal conductivity was measured on pieces from either the archive or working half of the split core sections, depending on the availability of suitable material. Discrete samples (~8 cm<sup>3</sup> cubes) were taken from Expedition 312 and 335 working section halves for physical properties and paleomagnetic measurements. Sampling was intentionally limited to preserve material for postcruise analyses. Shipboard samples were located close to where shipboard geochemistry and thin section samples were taken. Discrete samples were used for compressional wave (*P*-wave) velocity measurements in three orthogonal directions following the standard IODP convention (Fig. F2), and moisture and density (MAD) measurements were used to determine bulk density and porosity.

A comprehensive discussion of methodologies and calculations used in the *JOIDES Resolution* physical properties laboratory is presented in Blum (1997). Throughout the cruise, we uploaded raw and “processed” data to the LIMS database.

### Whole-Round Multisensor Logger measurements

GRA bulk density and magnetic susceptibility were measured nondestructively with the WRMSL. The sampling interval for WRMSL measurements was set at 1 cm with an integration time of 5 s for each data point to allow both instruments to acquire values from the same location downcore. Calibration was verified after each core measurement by passing a freshwater-filled calibration core through the WRMSL. The nominal accuracy of the calibrated instruments is 1%–2%.

### Gamma ray attenuation bulk density

The GRA densiometer on the WRMSL operates by passing gamma rays from a <sup>137</sup>Cs source through a whole-round core into a 75 mm × 75 mm sodium iodide detector located directly below the core. The input gamma ray peak has a principal energy of 0.662 MeV and is attenuated as it passes through the core. Attenuation of gamma rays, mainly by Compton scattering, is related to electron density, which is related to material bulk density by

$$\rho_b = \rho_e w / 2\sum N,$$

where

- $\rho_b$  = bulk density,
- $\rho_e$  = electron density,
- $w$  = molecular weight, and
- $N$  = atomic number of elements in the material.

For the majority of elements and for rock forming minerals,  $2\sum N/w$  is ~1, whereas for hydrogen  $2\sum N/w = 1.9841$ . Therefore, for a known thickness of sample the gamma ray count is proportional to density. Calibration of the GRA densiometer was performed using a core liner filled with freshwater and aluminum density standards. Recalibration was performed if the measured density of the freshwater standard was not  $1.00 \pm 0.02$  g/cm<sup>3</sup>. The spatial resolution of the GRA densiometer is <1 cm.

### Magnetic susceptibility

Magnetic susceptibility,  $\kappa$ , is a dimensionless measure of the degree to which a material can be magnetized by an external magnetic field:

$$\kappa = M/H \text{ (SI)},$$

where  $M$  is the magnetization induced in the material by an external field with a strength  $H$ . Magnetic susceptibility varies in response to the type and concentration of magnetic grains, making it useful for the identification of compositional variations.

The WRMSL measures volume magnetic susceptibility using a Bartington Instruments MS2 meter coupled to a MS2C sensor coil with a diameter of 8.8 cm and operating at a frequency of 0.565 kHz. During Expedition 335, the instrument was set to record SI units with an integration period of ~1 s, to give a sensitivity of  $1 \times 10^{-5}$  SI. The core diameter is smaller than the sensor coil aperture. The instrument output ( $\kappa_{\text{MEAS}}$ ) depends on the diameter of the core ( $d$ ) passing through the coil diameter ( $D$ ), so a correction factor ( $\kappa_{\text{REL}}$ ) is necessary to convert the instrument output to true volume susceptibility ( $\kappa$  in SI), where  $\kappa_{\text{REL}} = 3.45(d/D)^3$  (Bartington Instruments Ltd., 2011). The sensor is nominally calibrated for core where  $d/D = 0.66$ , so for the sensor in the WRMSL (where  $D = 8.8$  cm), the correction factor is 1.0 and  $\kappa = \kappa_{\text{MEAS}}$  if  $d = 5.8$  cm. During Expedition 335, where the core diameter varied in an unpredictable manner both within and between core pieces, a single correction factor was not justified, and therefore no corrections were applied to WRMSL magnetic susceptibility measurements; instead, raw data are reported in instrument units.

The along-core response curve of the MS2C coil has a full width of half maximum (FWHM) of ~4 cm (Blum, 1997) and is consistent with the decay in magnetic intensity with distance from a dipole (Fig. F20). Therefore, measurements of susceptibility from core pieces <8 cm long will significantly underestimate magnetic susceptibility by more than 10%.

The Bartington sensor has a maximum output threshold of 9,999 instrument units, so any readings  $\geq 10,000$  lose the most significant digit and are “wrapped” around to lower values. Observations that we judged to be in error, based on high susceptibility values of neighboring analyses and examination of the core, were corrected by adding 10,000. The few corrected magnetic susceptibility data are the only unfiltered data  $\geq 10,000$ . The corrected data are archived as “processed” data to the LIMS database.

### Natural Gamma Radiation Logger

Gamma rays are emitted from rocks primarily as a result of the radioactive decay of  $^{40}\text{K}$  and the decay of isotopes in the decay series of  $^{238}\text{U}$  and  $^{232}\text{Th}$ . Measurement of NGR from the recovered core provides an indication of the concentration of these elements and can also be used to correlate core with the down-hole gamma ray logs (e.g., Révillon et al., 2002).

The NGRL installed on the *JOIDES Resolution* was designed and built at the IODP-USIO at Texas A&M University (USA; Vasilyev et al., 2011). The main NGR detector unit consists of eight sodium iodide (NaI) scintillator detectors ( $\sim 500 \text{ in}^3$  each), seven plastic scintillation detectors, 22 photomultipliers, and passive lead shielding. The eight NaI detectors are spaced every 20 cm in the detector; the detectors themselves are semicylindrical annuli around the lower half of the core (each crystal is  $\sim 13$  cm wide along the core). Detectors are shielded by lead to reduce the measurement of external gamma radiation, and the NGRL also employs seven plastic scintillation detectors that detect and actively suppress the effect of high-energy gamma and muon components of cosmic radiation. The NGRL was calibrated using  $^{137}\text{Cs}$  and  $^{60}\text{Co}$  sources to identify peaks at 662 and 1330 keV, respectively.

Background measurements of an empty core liner counted for 20,000 s ( $>5$  h) were made upon arrival at Site 1256 (19 April 2011). Over the 100–3000 keV integration range, background counts averaged 4–5 cps and contributed  $\sim 80\%$  of the uncorrected total counts for the low-radioactivity mafic rocks measured during Expedition 335.

A single measurement run with the NGRL provides a total of 16 measurements at 10 cm intervals over a 150 cm section of core. To achieve a 10 cm interval using the NGRL’s eight sensors spaced every 20 cm, the NGRL records two sets of measurements offset by 10 cm. Readings at the ends of core sections are automatically corrected for the reduced signal because of an inferred “missing” volume of material, assuming the core is truncated perpendicular to the z-direction

at 0 cm and at a user-specified distance along the section. Total counts are routinely summed over the range of 100–3000 keV.

The quality of the energy spectrum measured depends on the concentration of radionuclides in the sample and on the counting time, with longer counting times providing better counting statistics. A live counting time of 1800 s (30 min) was set in each position (total live count time of 1 h per section). Improved counting statistics allow qualitative identification of the main contributors to the energy spectra (i.e.,  $^{40}\text{K}$  and intermediate isotopes in the  $^{232}\text{Th}$  and  $^{238}\text{U}$  decay chains). To this end, we extracted counts for the energy windows recommended by the International Atomic Energy Agency ([www-pub.iaea.org/mtcd/publications/pdf/te\\_1363\\_web.pdf](http://www-pub.iaea.org/mtcd/publications/pdf/te_1363_web.pdf)) for K, effective Th, and effective U (Table T8). Results provide a qualitative indication of the relative concentrations of each element. However, interference of energy spectra from each element’s decay series means that counts in each energy window include counts due to the decay of other radiogenic elements. For example, counts in the U window will include counts from the Th decay chain (and to a much lesser extent K), and counts in the K window will include counts from the decay chains of both Th and U. During Expedition 335, comparisons made between the counts in each window are thus qualitative. By building a database of well-resolved background-corrected spectra, the separation of  $^{40}\text{K}$ ,  $^{232}\text{Th}$ , and  $^{238}\text{U}$  contributions from the measured spectra will be straightforward once well-defined standards become available and the sensitivity matrix and/or stripping ratios are defined.

### Thermal conductivity

Thermal conductivity ( $k$ ) is a material property that describes how heat is transported through a material. At steady state, it is the constant of proportionality between the spatial temperature ( $T$ ) gradient and the heat-flux ( $q$ ) down-gradient, such that

$$q = -k\nabla T.$$

Thermal conductivities of rocks depend on many factors, including temperature, pressure, porosity, type of saturating fluid, and the composition, distribution, and alignment of mineral phases. Thermal conductivity was measured on split core pieces under ambient conditions using a Teka TK04 system. All measurements were made at room temperature and pressure and were not corrected for in situ conditions.

This system measures thermal conductivity by transient heating of the sample with a known heating power and geometry. Changes in temperature with



time during heating are recorded and used to calculate thermal conductivity. Heating power can be adjusted for each sample; as a rule of thumb, heating power in watts per meter is set to be approximately two times the expected thermal conductivity in watts per meter degree Kelvin. The temperature of the superconductive needle probe has a quasi-linear relationship with the natural logarithm of the time after the initiation of heating (Blum, 1997). The TeKa TK04 device uses a complex “special approximation method” (SAM) to calculate conductivity and to assess the fit of the heating curve. This method fits discrete windows of the heating curve to the theoretical temperature ( $T$ ) with time ( $t$ ) function:

$$T(t) = A_1 + A_2 \ln(t) + A_3 [\ln(t)/t] + (A_4/t),$$

where  $A_{1-4}$  are constants that are calculated by linear regression.  $A_1$  is the initial temperature, whereas  $A_2$ ,  $A_3$ , and  $A_4$  are related to geometry and material properties surrounding the needle probe. Having defined these constants (and how well they fit the data), the apparent conductivity ( $k_a$ ) for the fitted curve is time dependent and given by

$$k_a(t) = q/4\pi\{A_2 + A_3[1 - \ln(t)/t] - (A_4/t)\},$$

where  $q$  is the input heat flux. The maximum value of  $k_a$  and the time,  $t_{\max}$ , at which it occurs on the fitted curve are used to assess the validity of that time window for calculating the thermal conductivity. The best solutions are those where  $t_{\max}$  is greatest, and these solutions are selected for output. Fits are considered good if  $k_a$  has a maximum value,  $t_{\max}$  is large, and the standard deviation of the least-squares fit is low. For each heating cycle, several values are output that can be used to assess the quality of the data, including “logarithm of extreme time” (LET), which should be large, the number of solutions ( $N$ ), which should also be large, and the contact value, which assesses contact resistance between the probe and the sample and should be small (or uniform for repeated measurements).

Half-space determinations of thermal conductivity were made with a needle probe embedded in the bottom of a Plexiglas block with a thermal conductivity of 0.184 W/(m·K). Heat is assumed to be transferred through the sample, and the TK04 documentation indicates that heat flow through the Plexiglas block itself is only significant for sample thermal conductivities < 1 W/(m·K). Good thermal contact with the heating needle is required, so the split face of the samples was polished with 120-gauge silicon carbide powder. Tests conducted on Section 312-1256D-223R-3A (Piece 2) during Expedition 335 showed

negligible improvement using finer polishing grit (2.201 ± 0.015 W/[m·K] before polishing, 2.240 ± 0.028 W/[m·K] after polishing with 120-gauge silicon carbide powder, and 2.237 ± 0.035 W/[m·K] after polishing with 320-gauge silicon carbide powder).

We avoided the use of silicone thermal contact gel that could contaminate the core. Empirical tests with both a certified MACOR ceramic standard ( $k = 1.637 \pm 0.033$  W/[m·K]) and a gabbro sample suggested that deionized (DI) water or seawater ( $k = \sim 0.6$  W/[m·K]) can be used to improve sample/needle contact and provide consistent analyses within the analytical error (2%). Measurements without contact fluid yield more variable results, with most analyses >2% different from the expected conductivity (Table T9; Fig. F21).

Samples were saturated and left to equilibrate to room temperature in a seawater vacuum saturator for >24 h, and then the sample and sensor needle were equilibrated at room temperature in an isolated Styrofoam-covered seawater bath for at least 15 min prior to measurement. Isolation of the sample and sensor needle eliminated the effect of small but rapid temperature changes introduced by air currents in the laboratory, as well as the ship’s motion. The instrument internally measures temperature drift and does not begin a heating run until sufficient thermal equilibrium is attained.

Core pieces were measured at irregular intervals downhole (approximately one sample per section) depending on the availability of homogeneous and relatively vein/crack-free pieces long enough to be measured without edge effects (pieces >7 cm long; i.e., longer than the instrument needle). The MACOR ceramic standard was analyzed frequently between measurements to check the calibration and consistency of results (Table T9).

### Section Half Multisensor Logger measurements

The SHMSL was used to measure spectral reflectance and magnetic susceptibility on archive section halves. An electronic platform moves along a track above the section half, recording the sample height using a laser sensor. The laser establishes the location of the bottom of the section; then the platform reverses the direction of movement, moving from bottom to top taking measurements of point magnetic susceptibility and spectral reflectance data at 1 cm intervals.

### Color reflectance spectrometry

Reflectance from the section half was measured using an Ocean Optics Inc. system for ultraviolet

through visible to near-infrared light (171–1100 nm wavelength at 2 nm intervals). Each measurement takes ~5 s to acquire. Spectral data are routinely reduced to the  $L^*a^*b^*$  color system for output and presentation, in which  $L^*$  is luminescence,  $a^*$  is the blue–yellow value, and  $b^*$  is the red–green value. The color reflectance spectrometer calibrates on two spectra, pure white (reference) and pure black (dark). Color calibration was conducted approximately every 12 h.

### Point magnetic susceptibility

Point magnetic susceptibility is measured using a Bartington MS2E contact probe with a flat 15 mm diameter sensor operating at a frequency of 0.580 kHz. The sensor takes and averages three measurements at 1 s intervals to an accuracy of 5%. The area of response of the MS2E sensor is 3.8 mm × 10.5 mm, with a depth response of 50% at 1 mm and 10% at 3.5 mm, providing higher resolution measurements than the whole-round magnetic susceptibility instrument (Bartington Instruments, 2011). Units are reported in dimensionless SI units on a volume basis. The point magnetic susceptibility meter was calibrated by the manufacturer before installation on the ship. The probe is zeroed in air before each measurement point, and a background magnetic field is measured and removed from the data before being output.

As with the Bartington MS2C sensor on the WRMSL, the MS2 recorder attached to the SHMSL has an output threshold of 9999 SI and truncates the most significant digit for measurements >9999 SI. Following processing to remove data from within 1 cm of piece edges (see “[Data filtering](#)”), data were manually corrected and archived. We manually checked the data points, compared them to the data from the magnetic susceptibility coil on the WRMSL, and found a few spurious points that were corrected from the upper part of Section 335-1256D-214R-2 (see “[Physical properties](#)” in the “Site 1256” chapter).

### Discrete sample measurements

Cubes (~8 cm<sup>3</sup>) were cut from working section halves and non-core samples for discrete measurements of *P*-wave velocity and MAD. Physical property measurements were conducted following the thermal demagnetization temperature step of 100°C. The samples were then passed on to the paleomagnetists for further measurements.

### Moisture and density

Mass and volume measurements on discrete samples were made to determine water content, bulk and dry

density, porosity, and void ratio. MAD data are also used for comparison with GRA bulk density data from the WRMSL. The shipboard MAD facility for hard rock samples consists of a vacuum water saturator, a dual balance system, and a hexapycnometer.

#### *Vacuum water saturator*

We used a vacuum pump system to ensure complete saturation of discrete samples. The system consists of a plastic chamber filled with seawater. A vacuum pump then removes air from the chamber, essentially sucking air from pore spaces. Samples were kept under vacuum for at least 24 h. During this time, pressure in the chamber is monitored periodically, via a gauge attached to the vacuum pump, to ensure a stable vacuum. After removal from the saturator, cubes are stored in sample containers filled with seawater to maintain saturation.

#### *Dual balance system*

A dual balance system was used to measure both wet and dry masses. Two analytical balances (Mettler-Toledo XS204) compensate for ship motion; one acts as a reference and the other measures the unknown (i.e., a sample). A standard mass of similar value to that of the sample was placed on the reference balance to increase accuracy. Using a reference mass within ~10% of the sample mass, an accuracy of 0.005 g is readily attainable. After wet mass determinations and *P*-wave measurements and prior to the determination of dry masses, samples were placed in an oven at 105° ± 5°C for 24 h and then allowed to cool in a desiccator.

#### *Hexapycnometer system*

The hexapycnometer is an IODP custom-built system using six Micromeritics cell units, custom electronics, and custom control programs. The system measures dry sample volume using pressurized helium-filled chambers with a precision of 0.02 cm<sup>3</sup>. At the start of the expedition, and whenever the helium gas tank is changed, shipboard technicians perform a calibration using stainless steel spheres of known volume. For a measurement five cells were run that contain unknowns and one cell that contains two stainless steel calibration spheres (3 and 7 cm<sup>3</sup>) with a total volume of ~10 cm<sup>3</sup>. Calibration spheres were cycled through the cells to identify any systematic error and/or instrument drift. Spheres are assumed to be known to within 1% of their total volume. Individual volume measurements were preceded by three purges of the sample chambers with research grade (99.995% or better) helium heated to 28°C, followed by three data acquisition cycles.

### Moisture and density calculations

For density calculations, both mass and volume are first corrected for the salt content of the pore fluid:

$$M_s = [s(M_w - M_d)]/(1 - s),$$

where

- $s$  = pore water salinity,
- $M_s$  = mass of salt,
- $M_d$  = dry mass of the sample, and
- $M_w$  = wet mass of the sample.

Grain density ( $\rho_g$ ) is determined from the dry mass ( $M_d$ ) and dry volume ( $V_d$ ) measurements:

$$\rho_g = (M_d - M_s)/[V_d - M_s/\rho_s],$$

where  $\rho_s$  = density of salt (2.257 g/cm<sup>3</sup>).

The salt-corrected mass of pore water ( $M_{pw}$ ) is calculated as

$$M_{pw} = (M_w - M_d)/(1 - s).$$

Then, the volume of pore water ( $V_{pw}$ ) is

$$V_{pw} = M_{pw}/\rho_{pw} = (M_w - M_d)/[(1 - s)\rho_{pw}],$$

where we assume the density of the pore fluid ( $\rho_{pw}$ ) = 1.024 g/cm<sup>3</sup> (from calculations of fluid sampled at ~713 m in the hole; Teagle, Alt, Umino, Miyashita, Banerjee, Wilson, and the Expedition 309/312 Scientists, 2006).

To calculate sample bulk density ( $\rho_b$ ), first compute bulk volume:

$$V_b = V_d + V_{pw}$$

Then,

$$\rho_b = M_w/V_b.$$

### Porosity calculation

Porosity ( $\phi$ ) is calculated from the two volume parameters above:

$$\phi = V_{pw}/V_b.$$

### Compressional wave velocity

*P*-wave velocity ( $V_p$ ) measurements of hard rock samples were performed on the same discrete cube samples that were used for MAD and paleomagnetic determinations.  $V_p$  measurements were performed on seawater-saturated samples immediately after wet mass determinations were made. Measurements were made using the *x*-axis caliper contact transducers on

the  $V_p$  gantry. Samples were oriented following standard IODP conventions, and measurements were made in the *x*-, *y*-, and *z*-directions for each cube (Fig. F2). The system uses Panametrics-NDT Microscan delay line transducers, which transmit at 0.5 MHz. The peak of the first arrival was identified automatically by the installed IODP software. The complete waveform is stored with the data if reanalysis is deemed necessary. Shipboard visual checks of the picks appeared satisfactory. The distance between transducers was measured with a built-in linear voltage displacement transformer (LDVT).

Measurements on standards were conducted as frequently as necessary. Calibration was made with a series of acrylic cylinders of differing thicknesses and a known  $V_p$  of 2750 ± 20 m/s. In a set of 25 calibration measurements, there was no systematic drift over time with the mean value of 2753 ± 22 m/s, which is well within a 2% error margin and is very close to certified acrylic velocity of 2750 m/s. Individual results deviate from the “true” value by up to 2%. Further extensive test runs on standards confirmed the accuracy of 1%–2%. Instrument performance is worse on copper cylinders (which are more suitable for the hard rock calibration because of high rigidity and velocity). In a set of 12 measurements on copper cylinders, the mean was 4798 ± 80 m/s (1σ error), which is within the expected 2% error margin, but individual measurements may deviate by as much as 4% from the mean. This result most likely reflects the errors in the measurement of the shorter traveltimes through the faster velocity medium.

At the beginning of Expedition 335, >300  $V_p$  measurements were taken on 11 discrete gabbro samples from Expedition 312 cores to constrain the repeatability and uncertainty of  $V_p$  measurements, and thereby to define the optimum protocol for shipboard  $V_p$  measurements.

First, we conducted  $V_p$  measurements following Expedition 312 protocol. The surfaces of seawater-saturated cubes were wiped to remove excess water. The cubes were weighed for MAD analysis, and then  $V_p$  measurements were performed in three orthogonal directions, adding a drop of deionized water to the cube surface (according to the standard procedure) to improve coupling between the sample and the transducers. Each measurement was repeated three times to provide an estimate of the precision (Table T10).

One concern identified during Expedition 335 was that the majority of samples show a systematic increase in  $V_p$  values for each repeated measurement (Fig. F22). Large variations in  $V_p$  measured in orthog-

onal directions within each sample were also observed.

To investigate the causes of these increasing  $V_p$  values, we conducted 10 sets of repeat measurements on the same cube (Sample 335(312)-231R-3W, 52–54 cm; PP/PMAG), adding deionized water to cube surfaces for each measurement on each of three directions (Fig. F23; Table T11). A similar systematic increase in  $V_p$  was observed for each direction, until after approximately seven measurements when the results stabilized. The average increase in velocity before reaching a plateau value is ~600 m/s. Caliper separation was constant for each repeat reading, and measurements of standards before and after sample measurements allowed instrumental drift to be ruled out. So the systematic increase in velocity is produced by a decrease in the measured transit time, which we hypothesize reflected the resaturation of surfaces after they had been dried during wet mass measurements.

To test this hypothesis, we made repeat measurements of a sample under different conditions of surface saturation: without water added, with deionized water added to surfaces, and fully submerged in seawater bath during measurement. Measured  $V_p$  values decreased as the cube surface dried out (drying was qualitatively assessed as the sample surface color became lighter during the measurements) (Fig. F24; Table T12), suggesting that the saturation of the sample surfaces has a large effect on measured  $V_p$ .

To improve measurement precision, the saturation of sample surfaces needs to be constant for all measurements. We therefore constructed a seawater bath to maintain a constant surface saturation during  $V_p$  measurements of discrete samples (Fig. F25). The seawater bath has an open top to allow direct contact between the minicube and the upper transducer and a thin flexible rubber membrane at the bottom to provide good coupling with the lower transducer. The container was filled with seawater to ~1 mm above the sample to provide complete saturation and to avoid flooding the upper transducer. Measurements conducted using the seawater bath were more consistent than those conducted without the bath. The mean of standard deviations is 25 m/s with the bath, 135 m/s for wet surfaces without the bath, and 157 m/s for dry surfaces.

The presence of the membrane changed the elastic properties of the system, lowering velocity measurements compared to the plateau for saturated measurements without the seawater bath. To correct the effect of this rubber membrane, we made measurements on standards with and without the seawater bath. Repeat measurements under both saturated

and dry conditions for acrylic, copper, and aluminum standards indicate that the membrane is  $0.298 \pm 0.033$  mm thick and adds  $0.333 \pm 0.030$   $\mu$ s to the recorded traveltime (See PWAVE\_CALIBRATION\_BATH in PHYSPROP in “[Supplementary material](#)”). Measurements made with the seawater bath can thus be corrected using

$$V_p = (s - 0.298 \text{ mm}) / (t - 0.333 \mu\text{s}),$$

where  $s$  is the measured caliper separation and  $t$  is the measured sonic traveltime. This correction increases the measured velocity of gabbroic samples by ~600 m/s.

### Data filtering

Data obtained from the WRMSL, NGRL, and SHMSL are used to determine natural variations in physical properties, but a large degree of measured variation can be attributed to systematic errors associated with the geometry of the recovered core, specifically because of measurements that were taken (1) close to the ends of sections and pieces, (2) over cracks within pieces, or (3) on pieces that were not ideal 66 mm diameter cylindrical cores for which the system is calibrated. For bulk volumetric measurements (magnetic susceptibility on the WRMSL and NGR on the NGRL), corrections can be made that account for the reduced volume of material in the vicinity of the sensor. For point measurements (GRA, reflection spectroscopy color [RSC], and point magnetic susceptibility [MSPOINT]), gaps and irregular core surfaces can lead to poor data, and these should be removed before the data are interpreted. We therefore filtered the data to remove and/or correct measurements that are affected by geometrical departures from a continuous cylindrical core 66 mm in diameter.

A filtering algorithm was developed to remove data points from gaps and cracks using GRA density data from the WRMSL and the laser profile height from the SHMSL to identify gaps. GRA density data are sensitive to the bulk density of the rock in an area of ~1 cm<sup>2</sup>. Gaps between pieces or fractures can generate anomalously low densities, and as the densities of rocks vary by less than an order of magnitude and are greater than water (1 g/cm<sup>3</sup>), it is relatively easy to define a threshold filter that uses density to identify gaps or sections of the core with a reduced volume of material. This method of filtering is particularly effective for core recovered during Expedition 335 and core reanalyzed from Expedition 312, where porosity is low and bulk density is relatively constant. Laser profile height data from the SHMSL pro-



vides an independent method to identify core pieces.

### Data culling

Using GRA density and laser profile data, we defined gaps in the core on the basis of a threshold value below which gaps were defined (1 g/cm<sup>3</sup> for whole-round GRA density and <2 cm for laser profile data). In addition, gaps were defined where significant horizontal gradients in the data occurred (>0.2 g/cm<sup>3</sup> per centimeter for GRA density and >1 cm per centimeter for laser profile height). Visual inspection suggested that these two parameters defined all significant piece edges and gaps in the sections. Once gaps were defined, data were removed (culled) from gaps and for a distance adjacent to the gap that was specified by the instrument's resolution or sensor size (Table T13). Given the low resolution of the NGRL, no gap filtering was attempted for NGR data.

### Predictive filtering of magnetic susceptibility data

The simple culling of data points within a certain distance of piece edges is a useful first-order filter. However, for the magnetic susceptibility meter attached to the WRMSL the response curve indicates that the minimum length of pieces that can be analyzed to give >90% of the true magnetic susceptibility is ~8 cm. During Expeditions 312 and 335, very few pieces longer than 8 cm were recovered; thus, only ~10% of data reanalyzed from Expedition 312 is retained, whereas <1% of data from Expedition 335 core is retained after a simple culling filter is applied. Simple culling of the data therefore retains little data for interpretation. Consequently, we developed and applied a filter defined by the response curve of the MS2C meter (Fig. F20). Using the distribution of known gaps to define a gap function  $g(x)$ , where  $g(x) = 1$  for core and  $g(x) = 0$  for gaps between core,  $g(x)$  can be convolved with the instrument response curve to specify the magnitude of correction required (Fig. F26). Clearly, this method requires the location of the gaps to be accurately known, and errors associated with the correction are greater closer to piece edges. Despite this caveat, synthetic tests show that, theoretically, this filter can be used to determine the magnetic susceptibility of pieces <8 cm in length (e.g., the interval from 10 to 30 cm).

In practice, we defined and applied this filter in three separate ways:

1. Using gaps defined from GRA density data to make a simple binary input that was convolved with the response function,
2. Using gaps defined by the laser profile height data to make a simple binary input filter that was convolved with the response function, and
3. Using normalized GRA density to define a normalized function of material volume (assuming constant grain density) that was convolved with the MS2C response curve.

The results of these three filters are averaged to define a single output value (Fig. F27); we take this approach (1) so that the different data used to define the filters (GRA density and laser profile data) are treated independently and (2) to provide an independent assessment of the error in the filters based on the standard deviation of the three filtered results, in addition to errors defined by uncertainty in the filter definition.

### Scaling archive-half data measured by WRMSL

For WRMSL magnetic susceptibility of Expedition 312 archive section half measurements, results were compared with SHMSL point magnetic susceptibility data. Despite scatter due to the different resolutions of the two measurements, a linear trend was observed, indicating a best-fit scaling factor of ~1.8. This scaling factor accounts most likely for both the decreased volume of measuring section halves and for the fact that the Expedition 312 core is not 58 mm in diameter.

GRA density measurements of section halves are significantly lower than full core section measurements (~1–1.2 g/cm<sup>3</sup>). Calculated density is dependent on the volume of analyzed material according to attenuation of waves and generally obeys an exponential decay function with distance; it follows that the scaling factor for GRA density measured for a core of reduced diameter can be approximated by

$$\rho_{\text{scale}} = \rho_{\text{obs}}(D/d),$$

where

- $D$  = diameter of core for which the instrument is calibrated,
- $d$  = diameter of the measured core,
- $\rho_{\text{obs}}$  = output GRA density, and
- $\rho_{\text{scale}}$  = corrected GRA density.

For section half measurements,  $d = \sim 28$  mm and we assume  $D = 66$  mm, so measurements are scaled by ~2.3. Following this correction, archive-half mea-

measurements are directly comparable to Expedition 312 GRA density measurements and discrete sample density measurements.

### Magnetic susceptibility measurements on non-core samples

We used a Bartington MS2F handheld susceptometer to measure susceptibility of non-core samples recovered during Expedition 335. After zeroing the probe in air, we measured rock samples by placing the probe at the surface of the samples. The instrument has an operating frequency of 0.580 kHz (Bartington Instruments Ltd., 2011). Measured values are approximately the same as true volume susceptibility of the material.

## Downhole logging

Downhole logs are measurements of physical, chemical, and structural properties of the formation surrounding a borehole that are made after completion of drilling. Data are continuous with depth (at vertical sampling intervals ranging from 2.5 mm to 15 cm) and are measured in situ. Sampling is intermediate between laboratory measurements on core samples and geophysical surveys and provides a necessary link for the integrated understanding of physical properties on all scales.

Logs can be interpreted in terms of the stratigraphy, lithology, mineralogy, and geochemical composition of the formation. They also provide information on the status and size of the borehole and on possible deviations or deformations induced by drilling, formation stress, or instability, such as breakouts or fractures. When core recovery is incomplete or disturbed, log data may provide the only way to characterize the formation. These data can be used to determine the actual thickness of individual units or lithologies when contacts are not recovered, to constrain the depth of features in the cores, or to identify intervals such as breccias that are often not recovered. When core recovery is good, log and core data complement one another and may be interpreted together. In particular, the imaging tools provide oriented images of the borehole wall than can help reorient the recovered core within the geographic reference frame.

### Operations

Logs are recorded with a variety of tools combined into several tool strings, which are run down the hole after completion of drilling operations. Only one tool string was successfully deployed during Expedition 335: the triple combination, or “triple

combo” (porosity, density, and resistivity) (Fig. F28; Table T14). The Formation MicroScanner (FMS)-sonic (electrical images of the borehole wall and sonic velocity) and the Ultrasonic Borehole Imager (UBI; borehole images) were scheduled to run, but a failure during the FMS-sonic deployment prevented us from recording these data.

Initially, a temperature log was also planned to record formation equilibrium temperature before drilling. A vertical seismic profile was also scheduled at the end of the expedition to tie the newly drilled section to the seismic surveys and the seismic Layer 2/3 boundary. The efforts necessary to reach the bottom of the hole at the beginning of the expedition and the limited new penetration precluded the deployment of these tools.

During hole cleaning operations, high-viscosity drilling fluids were regularly pumped into the hole to flush out debris. At the end of the last magnetic fishing run, the hole was circulated with seawater, and the fluid below ~1250 mbsf was displaced by freshwater. Freshwater (i.e., resistive water) was used to reduce the contrast in resistivity between the highly resistive gabbroic rocks and the borehole fluid and to enhance the quality of the images (Blackman et al., 2006; Shipboard Scientific Party, 1999b).

Each tool string deployment is a logging “run,” starting with the assembly of the tool string and the necessary calibrations. The tool string is sent down to the bottom of the hole while recording a partial set of data and then pulled up at a constant speed, typically 250–300 m/h, to record the main data. During each run, the tool string can be lowered down and pulled up the hole several times for quality control or to try to increase the circumferential coverage of the imaging tools (see “[Logged properties and tool measurement principles](#)”). Each lowering or hauling-up of the tool string while collecting data constitutes a “pass.” During each pass, incoming data are recorded and monitored in real time on the surface MAXIS system. A logging run is complete once the tool string has been brought to the rig floor and disassembled.

### Logged properties and tool measurement principles

The logs recorded during Expedition 335 are listed in Table T15. More detailed information on individual tools and their geological applications may be found in Ellis and Singer (2007), Goldberg (1997), Lovell et al. (1998), Rider (1996), Schlumberger (1989), and Serra (1984, 1986). A complete online list of acronyms for the Schlumberger tools and measurement

curves is available at [www.slb.com/modules/mnemonics/index.aspx](http://www.slb.com/modules/mnemonics/index.aspx).

### Borehole temperature

Each tool string deployed during Expedition 335 included the Modular Temperature Tool (MTT) to measure borehole fluid temperature. The MTT was designed at the Lamont-Doherty Earth Observatory (LDEO) to be able to resolve centimeter-scale temperature variations at typical logging speeds of 250–300 m/h. It uses two temperature sensors: a fast responding thermocouple and a highly accurate resistance temperature detector (RTD). The sonde also contains an accelerometer for depth correction and is combined with a specially designed cartridge to allow data transmission through the Schlumberger string and wireline.

One additional temperature measurement was made during each logging run by a sensor included in the Logging Equipment Head with Tension and Mud Temperature (LEH-MT) cable head and processed by the Enhanced Digital Telemetry Cartridge (EDTC) (see “[Auxiliary logging equipment](#)”).

Because logs are recorded shortly after coring, borehole temperature is highly perturbed by the large amounts of seawater circulated during the drilling process. However, temperature changes observed over several hours between successive logging runs provide a measure of the thermal rebound of the borehole fluid toward the formation temperature. The rate of thermal rebound can be modeled to estimate equilibrium temperature profiles (Bullard, 1947; Lachenbruch and Brewer, 1959).

### Natural radioactivity

The Hostile Environment Natural Gamma Ray Sonde (HNGS) measures the natural radioactivity in the formation. It uses two bismuth germanate scintillation detectors and five-window spectroscopy to determine concentrations of K, Th, and U, whose radioactive signals dominate the natural radiation spectrum. The HNGS filters out gamma ray energies below 500 keV, eliminating sensitivity to bentonite or KCl in the drilling mud and improving measurement accuracy.

The EDTC used to communicate data to the surface includes a sodium iodide scintillation detector to measure the total natural gamma ray emission. It is not a spectral tool, but it provides high-resolution total gamma ray for each pass that allows for precise depth match processing between logging runs and passes.

### Density

Formation density was measured with the Hostile Environment Litho-Density Sonde (HLDS). The sonde contains a radioactive cesium ( $^{137}\text{Cs}$ ) gamma ray source (622 keV) and far and near gamma ray detectors mounted on a shielded skid, which is pressed against the borehole wall by an eccentricizing arm. Gamma rays emitted by the source undergo Compton scattering, where gamma rays are scattered by electrons in the formation. The number and energy of scattered gamma rays that reach the detectors is proportional to the density of electrons in the formation, which is in turn related to bulk density. Porosity may be derived from this bulk density if the matrix (grain) density is known. Good contact between the tool and borehole wall is essential for good HLDS logs; poor contact results in underestimation of density values.

The HLDS also measures photoelectric absorption as the photoelectric effect (PEF). Photoelectric absorption of the gamma rays occurs when their energy is reduced below 150 keV after being repeatedly scattered by electrons in the formation. Because PEF depends on the atomic number of the elements encountered, it varies with the chemical composition of the minerals present and can be used for the identification of some minerals (Bartetzko et al., 2003; Blackman et al., 2006).

### Porosity

Formation porosity was measured with the Accelerator Porosity Sonde (APS). The sonde includes a minitron neutron generator that produces fast (14.4 MeV) neutrons, along with five neutron detectors (four epithermal and one thermal) positioned at different distances from the minitron. The tool's detectors count neutrons that arrive after being scattered and slowed by collisions with atomic nuclei in the formation.

The highest energy loss occurs when neutrons collide with hydrogen nuclei, which have practically the same mass as the neutron. In contrast, neutrons simply bounce off heavier elements without losing much energy. If the hydrogen content is high, as in high-porosity formations, many neutrons are slowed and captured by the formation and the count rate will be low. When hydrogen content is low, fewer neutrons are absorbed and more reach the detector. However, in igneous and hydrothermally altered rocks, hydrogen may be present in alteration minerals, which can result in an overestimation of porosity values in these rocks.

Upon reaching thermal energies (0.025 eV), neutrons are captured by the nuclei of Cl, Si, B, and

other elements, resulting in a gamma ray emission. This neutron capture cross section ( $\Sigma_f$ ) is also measured by the tool and allows us to identify such elements.

### Electrical resistivity

The High-Resolution Laterolog Array (HRLA) tool provides six resistivity measurements with different depths of investigation (including the borehole, or mud resistivity, and five measurements of formation resistivity with increasing penetration into the formation). The sonde sends a focused current into the formation and measures the intensity necessary to maintain a constant drop in voltage across a fixed interval, providing direct resistivity measurement. The array has one central source electrode and six electrodes above and below it, which serve alternatively as focusing and returning current electrodes. By rapidly changing the role of these electrodes, a simultaneous resistivity measurement at six penetration depths is achieved. The tool is designed to ensure that all signals are measured at exactly the same time and same tool position and to reduce the sensitivity to “shoulder bed” effects when crossing sharp beds thinner than the electrode spacing. The design, which eliminates the need for surface reference electrodes, improves formation resistivity evaluation compared to the traditional dual laterolog sonde that was used in earlier expeditions to Hole 1256D.

Typically, igneous minerals found in crustal rocks are electrical insulators, whereas sulfide and oxide minerals as well as ionic solutions like pore water are conductors. In most rocks, electrical conduction occurs primarily by ion transport through pore fluids and thus is strongly dependent on porosity. Electrical resistivity, therefore, can be used to evaluate alteration, porosity, and fluid salinity.

### Acoustic velocity

The Dipole Sonic Imager (DSI) generates acoustic pulses from various sonic transmitters and records the full waveforms with an array of eight receivers. The waveforms are then used to calculate the sonic velocity in the formation. The omnidirectional monopole transmitter emits high-frequency (5–15 kHz) pulses to extract the compressional velocity ( $V_p$ ) of the formation, as well as the shear velocity ( $V_s$ ) when it is faster than the sound velocity in the borehole fluid. The same transmitter can be fired in alternance at a lower frequency (0.5–1 kHz) to generate Stoneley waves that are sensitive to fractures and variations in permeability (Hornby et al., 1989). The DSI also has two orthogonal dipole transmitters (0.5–3.5 kHz), which allow the measurement of shear

wave velocity in “slow” formations, where  $V_s$  is slower than the velocity in the borehole fluid. However, in formations such as the basement penetrated in Hole 1256D,  $V_s$  can be measured from the monopole waveforms. These higher frequency waveforms usually provide a sharper shear arrival and more accurate estimate of  $V_s$  than either of the dipole sources.

### Formation MicroScanner

The FMS provides high-resolution electrical resistivity images of the borehole wall. The tool has four orthogonal arms and pads, each containing 16 button electrodes that are pressed against the borehole wall during the recording. A focused current is emitted from the button electrodes into the formation, with a return electrode near the top of the tool. The “buttons” are arranged in two diagonally offset rows of eight electrodes each (see insert in Fig. F28), and the intensity of the current passing through each one is recorded at a vertical sampling rate of 2.54 mm ( $1/10$  inch). By combining these measurements with the acceleration and orientation data recorded by the GPIT (see “[Accelerometry and magnetic field measurement](#)”), processing transforms the raw data into oriented high-resolution images that reveal the geologic structures of the borehole wall. Features such as fractures, breccias, pillows, or flows can be resolved. The images are oriented to magnetic north, so that the dip and direction (azimuth) of features in the formation can be measured. Because the pads cover only ~25% of the borehole wall, two full passes are usually recorded along the entire open hole in order to try to increase the azimuthal coverage of the images.

### Ultrasonic borehole images

The UBI uses a rotating ultrasonic transducer to record acoustic images of the borehole wall (see insert in Fig. F28). The transducer emits ultrasonic pulses at a frequency of 250 or 500 kHz (low and high resolution, respectively), which are reflected by the borehole wall and then received by the same transducer. Both the amplitude and traveltime of the reflected signal are measured. Continuous rotation of the transducer and the upward motion of the tool produce a complete map of the borehole wall. The amplitude depends on the reflection coefficient of the borehole fluid/rock interface, the position of the UBI tool in the borehole, the shape of the borehole, and the roughness of the borehole wall. Fractures or other variations in the character of the drilled rocks can be recognized in the amplitude image. The recorded traveltime image gives detailed information about the shape of the borehole. Amplitude and



traveltime are recorded with a reference to magnetic north by means of the GPIT (see “[Accelerometry and magnetic field measurement](#)”), permitting the orientation of the images and observed features. The full 360° coverage of the UBI images can also provide a measure of the local stress through identification of borehole breakouts in the direction of the minimum principal horizontal stress (Bell and Gough, 1983). Such subvertical features are more elusive to FMS images because of the partial azimuthal coverage provided by the four pads.

### Accelerometry and magnetic field measurement

The primary purpose of the General-Purpose Inclinerometry Tool (GPIT), which includes a three-component accelerometer and a three-component magnetometer, is to determine the acceleration and orientation of the imaging tools during wireline logging. Because of the failure to deploy the imaging tools during Expedition 335, the GPIT was only used to estimate downhole tool motion and evaluate the performance of the new heave compensator.

### Auxiliary logging equipment

#### *Cable head*

The Schlumberger Logging Equipment Head (LEH, or cable head) measures tension at the very top of the wireline tool string, which diagnoses difficulties in running the tool string up or down the borehole or when exiting or entering the drill string or casing. The LEH-MT, used for the first time in IODP during Expedition 335, also includes a temperature sensor on its outside to measure the borehole fluid temperature, or “mud temperature.”

#### *Telemetry cartridges*

Telemetry cartridges are used in each tool string to allow the transmission of the data from the tools to the surface. In addition, the EDTC, also used for the first time in IODP during Expedition 335, includes a sodium iodide scintillation detector to measure the total natural gamma ray emission of the formation. This gamma ray log was used to match the depths between the different passes and runs. Temperature measurements from the LEH-MT are also processed by the EDTC before being sent to the surface for real-time monitoring.

#### *Joints and adapters*

Because the tool strings combine tools of different generations and with various designs, they include several adapters and isolation joints between individual tools to allow communication, avoid interfer-

ences (mechanical, acoustic, or electrical), or position the tool properly in the borehole. The knuckle joints in particular are used to allow some of the tools such as the HRLA to remain centralized in the borehole while the overlying HLDS and APS are pressed against the borehole wall. All of these additions are included and contribute to the total length of the tool strings in Figure [F28](#).

### Log data quality

The principal factor affecting log data quality is the condition of the borehole. If the borehole diameter is too large or varies over short intervals because of washouts and ledges made of layers of different materials, logs from tools that require good contact with the borehole wall (i.e., the FMS and density tools) may be degraded. Deep investigation measurements such as gamma ray, resistivity, and sonic velocity, which do not require contact with the borehole wall, are generally less sensitive to borehole conditions. Very narrow (“bridged”) sections will also cause irregular log results.

The quality of the logging depth determination depends on several factors. The depth of the logging measurements is determined from the length of the cable played out from the winch on the ship. Uncertainties in logging depth occur because of ship heave, cable stretch, and cable slip. Similar uncertainties in coring depth occur because of incomplete recovery or ship heave. Tidal changes in sea level also have an effect, with an amplitude of >1 m at the time of logging Hole 1256D. All of these factors generate some discrepancy between core sample depths, logs, and individual logging passes. To minimize the effect of ship heave on logging depths, a new hydraulic wireline heave compensator (WHC) was used to adjust the wireline length for rig motion during wireline logging operations.

### Wireline heave compensator

Expedition 335 continued evaluation of the new WHC system. The system is designed to compensate for the vertical motion of the ship and maintain a steady motion of the logging tools. It uses vertical acceleration measurements made by a motion reference unit (MRU), located under the rig floor near the center of gravity of the ship, to calculate the vertical motion of the ship. It then adjusts the length of the wireline by varying the distance between two sets of pulleys through which the cable passes. Real time measurements of uphole (surface) and downhole acceleration are made simultaneously by the MRU and by the GPIT tool, respectively. A LDEO-developed software package allows these data to be analyzed and compared in real time, displaying the actual mo-

tion of the logging tool string and enabling evaluation of the efficiency of the compensator.

### Logging data flow and log depth scales

Data for each wireline logging run were monitored in real time and recorded using the Schlumberger MAXIS 500 system. The initial logging data are referenced to the rig floor. After logging was completed, all logging depths were shifted to the seafloor. This is usually done by identifying the seafloor from a step in gamma ray, but in the case of Hole 1256D all depths were adjusted so that the bottom of the casing was at 269 mbsf. Using the gamma ray log, individual passes were interactively depth matched with one reference pass, in this case the main pass of the triple combo. The resulting data were made available to the science party within a day after their acquisition.

Downhole log data were also transferred onshore to LDEO for standardized data processing. In addition to a standardized depth matching, corrections are made to certain tools and logs, documentation for the logs (with an assessment of log quality) is prepared, and data are converted to ASCII for the conventional logs and to GIF for the FMS and UBI images. Schlumberger GeoQuest's GeoFrame software package is used for most of the processing.

### Core section image analysis

During Expedition 335, external surfaces of whole-round core sections were scanned using an experimental system involving multiple passes through the IODP Section Half Imaging Logger (SHIL). In addition, all archive section halves were imaged with the same SHIL, following a long tradition using film photography or digital imaging. Core imaging during this expedition had four main objectives:

1. To provide a comprehensive suite of digital core images, including both unrolled 360° and section half surface images, to aid petrological interpretation;
2. To identify and measure planar features on unrolled 360° images for comparison with core structural analysis and integration with structures measured on geographically oriented FMS and UBI images (see [“Formation MicroScanner”](#) and [“Ultrasonic borehole images”](#));
3. To correlate core images with FMS and UBI images of the borehole wall to determine true core depth as opposed to curated depth in intervals with <100% recovery; and
4. To match structures observed on core images with FMS and UBI images, as well as to reorient core pieces and associated structural data to

magnetic north obtained from the GPIT on the FMS and UBI tool strings.

Core orientation is particularly important for Expedition 335 because Site 1256 is at low paleolatitude, which means the paleomagnetic inclination will be nearly horizontal and the magnetic polarity will be indeterminate from azimuthally unoriented cores. Similarly, without a known polarity, the paleomagnetic declination cannot be used to orient the core for structural analyses or for the determination of anisotropy of physical properties. Site 1256 is sufficiently close (<10 km) to the magnetic Anomaly 5Bn/5Br boundary that the polarity cannot simply be assumed. In order to determine the source of marine magnetic anomalies, which is one of the expedition objectives, estimating the true, rather than the relative, paleomagnetic direction is critical and can only be accomplished if the core is oriented.

### SHIL core scanning system

To avoid the expense of renting a dedicated 360° core scanner (e.g., the DMT Color CoreScan system deployed during Leg 206 and Expedition 309/312, among other expeditions), an experimental system was developed at IODP-USIO to use the existing, higher resolution SHIL generally used for section half surfaces to image the outer surface of the core. The main element of this system is an aluminum frame that can simultaneously hold the cylindrical pieces of a single core section and rotate them in 90° increments (Fig. F29). The frame consists of four aluminum strips ~155 cm × 4 cm in dimension, all of which latch at each end into a pair of rotatable spindles. Each strip is milled with a concave surface that rests against the core pieces. Four images of the core surface are later processed to simulate a continuous image of the unrolled 360° surface.

### Methodology

On each core piece, a vertical red line was drawn with a wax pencil to define the core split. Convention is such that, with the core upright, the archive half is to the left of this line and the working half is to the right (Fig. F2). The split line therefore corresponds to the 90° direction (+y) in the core-reference coordinates used for structural geology and paleomagnetism. When the core images are processed to a simulated unrolled image, nonhorizontal planar structures (e.g., veins, faults, or fractures) should produce sinusoidal-shaped curves. These can be matched to similar-shaped features imaged along the borehole wall by the four pads of the FMS or by the UBI logging tools. Other distinct petrological features or structures that are imaged on the outer surface of the core and the borehole wall can be simi-

larly matched to determine the depth of the core in the borehole and reorient the core azimuth (e.g., MacLeod et al., 1994; Morris et al., 2009).

In detail, the process for generating the simulated unrolled image includes the following steps:

1. The vertically oriented pieces for a single section are placed at their curated relative depths within the aluminum frame, with two aluminum strips in place to hold the core and two removed for access.
2. After the frame is moved to the SHIL, three aluminum strips secure the core surface and one is removed to allow imaging.
3. After imaging one surface, one aluminum strip is replaced, the section is turned 90°, and the next strip is removed to allow imaging.

This process is repeated to generate four images. These images are combined in a simulated unrolled image using a computer program written in C language that uses core diameter as the parameter to relocate pixels, stretching each image for the conversion from orthogonal to unrolled view and assembling them into a composite image with the image width scaled to the core circumference. The source code for this program is provided in `WHOLE_ROUND_IMAGE_CODE` in `PHYSPROP` in **“Supplementary material.”**

For matching core-surface features to borehole features, one generally must assume the features are planar to extrapolate across the material destroyed by the drill bit. An obvious point to consider is that the vertical extent of a planar feature will scale with the ratio of the borehole diameter to the core diameter, generally between 4 and 5 cm. A less obvious point is that the usual presentation of images looking inward toward the core surface but outward toward the borehole wall results in mirroring geometric relations, with clockwise downcore (increasing angle in IODP coordinates) left-to-right in the logging image but right-to-left in the core surface image. Generally at least three planar features in a large piece from a high-recovery core will be required for unambiguous orientation. Unfortunately, neither FMS nor UBI tools were successfully deployed during Expedition 335, so orientation of pieces below ~1410 mbsf from Expeditions 312 and 335 requires future logging.

## Underway geophysics

While transiting between Costa Rica, Site 1256, and Panama during Expedition 335, we collected 3.5 and

12 kHz echo sounder and magnetometer data. Because the exact location of Site 1256 is well established based on analysis of site survey data and drilling during Leg 206 and Expedition 309/312, no additional surveys were conducted.

Navigation data were acquired throughout the expedition with two Ashtec GG24 GPS+GLONASS receivers with antennas mounted on the starboard stack aft of the moonpool. The datum is the moonpool. GPS fixes were recorded by WinFrog navigation software.

The time datum for all underway geophysics activities is Universal Time Coordinated (UTC) (similar to Greenwich Mean Time), as provided from the Ashtec receivers. If communication between an Ashtec receiver and the satellite is interrupted, the receiver uses its own internal clock to maintain the time base. The WinFrog navigation system displays UTC time many times per second, but the internal clock is not synchronized to UTC.

Magnetic data were acquired with Marine Magnetics SeaSpy proton magnetometer towed 500 m behind the ship. Values of total field intensity were acquired approximately every 3 s using the SeaLINK program from Marine Magnetics.

Underway 3.5 and 12 kHz echo sounder data were acquired using a SyQwest Bathy 2010 CHIRP sub-bottom profiler and bathymetric echo sounder: the 3.5 kHz frequency was obtained with a 12 × TR-109 transducer array driven by a 10 kW power amplifier, and the 12 kHz frequency was obtained with an EDO-323C transducer. Transducers are housed in the forward sonar dome. Data were processed in real time using a Raytheon CESP III (Correlator Echo Sounder Processor). Underway echo sounder data were recorded digitally as uncorrected depths using the program Bathy from SyQwest.

Uncorrected depths convert traveltime to nominal depth assuming a sound velocity of 1500 m/s in seawater. Corrected depths (using Matthews’s tables to allow for varying sound speed with depth and location in the ocean (Carter, 1980) are computed by postprocessing.

Transducer elements are 0.9 m below the keel of the ship and 18.4 m below the dual elevator stool (the reference datum for drilling activities). Water depth relative to sea level was obtained by adding 0.9 m and the mean draft (typically  $6.5 \pm 0.6$  m) to the corrected echo sounder depth.

Underway data are released to and archived by the National Geophysical Data Center at [www.ngdc.noaa.gov/mgg/geodas/trackline.html](http://www.ngdc.noaa.gov/mgg/geodas/trackline.html).

## References

- Alt, J.C., Laverne, C., Coggon, R.M., Teagle, D.A.H., Banerjee, N.R., Morgan, S., Smith-Duque, C.E., Harris, M., and Galli, L., 2010. Subsurface structure of a submarine hydrothermal system in ocean crust formed at the East Pacific Rise, ODP/IODP Site 1256. *Geochem., Geophys., Geosyst.*, 11:Q10010. doi:10.1029/2010GC003144
- Arason, P., and Levi, S., 2010. Maximum likelihood solution for inclination-only data in paleomagnetism. *Geophys. J. Int.*, 182(2):753–771. doi:10.1111/j.1365-246X.2010.04671.x
- Bach, W., Erzinger, J., Alt, J.C., and Teagle, D.A.H., 1996. Chemistry of the lower sheeted dike complex, Hole 504B (Leg 148): influence of magmatic differentiation and hydrothermal alteration. In Alt, J.C., Kinoshita, H., Stokking, L.B., and Michael, P.J. (Eds.), *Proc. ODP, Sci. Results*, 148: College Station, TX (Ocean Drilling Program), 39–55. doi:10.2973/odp.proc.sr.148.114.1996
- Bartetzko, A., Paulick, H., Iturrino, G., and Arnold, J., 2003. Facies reconstruction of a hydrothermally altered dacite extrusive sequence: evidence from geophysical downhole logging data (ODP Leg 193). *Geochem., Geophys., Geosyst.*, 4(10):1087. doi:10.1029/2003GC000575
- Bartington Instruments, Ltd., 2011. *Operation Manual for MS2 Magnetic Susceptibility System*: Oxford (Bartington Instruments, Ltd.).
- Bell, J.S., and Gough, D.I., 1983. The use of borehole breakouts in the study of crustal stress. In Zoback, M.D., and Haimson, B.C. (Eds.), *Hydraulic Fracturing Stress Measurements*: Washington (Natl. Acad. Press), 201–209.
- Blackman, D.K., Ildefonse, B., John, B.E., Ohara, Y., Miller, D.J., MacLeod, C.J., and the Expedition 304/305 Scientists, 2006. *Proc IODP*, 304/305: College Station, TX (Integrated Ocean Drilling Program Management International, Inc.). doi:10.2204/iodp.proc.304305.2006
- Blum, P., 1997. Physical properties handbook: a guide to the shipboard measurement of physical properties of deep-sea cores. *ODP Tech. Note*, 26. doi:10.2973/odp.tn.26.1997
- Bullard, E.C., 1947. The time necessary for a borehole to attain temperature equilibrium. *Mon. Not. R. Astron. Soc.*, 5(S5):127–130. doi:10.1111/j.1365-246X.1947.tb00348.x
- Cande, S.C., and Kent, D.V., 1995. Revised calibration of the geomagnetic polarity timescale for the Late Cretaceous and Cenozoic. *J. Geophys. Res., [Solid Earth]*, 100(B4):6093–6095. doi:10.1029/94JB03098
- Carter, D.J.T., 1980. *Echo-Sounding Correction Tables (Formerly Matthews' Tables)*: Taunton, Somerset, UK (Hydrographic Dept., Min. of Defence).
- Cordier, C., Clément, J.-P., Caroff, M., Hémond, C., Blais, S., Cotten, J., Bollinger, C., Launeau, P., and Guille, G., 2005. Petrogenesis of coarse-grained intrusives from Tahiti Nui and Raiatea (Society Islands, French Polynesia). *J. Petrol.*, 46(11):2281–2312. doi:10.1093/petrology/egi055
- Davis, G.H., 1984. *Structural Geology of Rocks and Regions*: New York (John Wiley and Sons, Inc.).
- Dunlop, D.J., 2003. Stepwise and continuous low-temperature demagnetization. *Geophys. Res. Lett.*, 30(11):1582. doi:10.1029/2003GL017268
- Ellis, D.V., and Singer, J.M., 2007. *Well Logging for Earth Scientists*, (2nd ed.): Dordrecht, The Netherlands (Springer).
- Expedition 304/305 Scientists, 2006. Methods. In Blackman, D.K., Ildefonse, B., John, B.E., Ohara, Y., Miller, D.J., MacLeod, C.J., and the Expedition 304/305 Scientists, *Proc. IODP*, 304/305: College Station, TX (Integrated Ocean Drilling Program Management International, Inc.). doi:10.2204/iodp.proc.304305.102.2006
- Expedition 309/312 Scientists, 2006. Methods. In Teagle, D.A.H., Alt, J.C., Umino, S., Miyashita, S., Banerjee, N.R., Wilson, D.S., and the Expedition 309/312 Scientists, *Proc. IODP*, 309/312: Washington, DC (Integrated Ocean Drilling Program Management International, Inc.). doi:10.2204/iodp.proc.309312.102.2006
- Expedition 330 Scientists, 2012. Methods. In Koppers, A.A.P., Yamazaki, T., Geldmacher, J., and the Expedition 330 Scientists, *Proc. IODP*, 330: Tokyo (Integrated Ocean Drilling Program Management International, Inc.). doi:10.2204/iodp.proc.330.102.2012
- Expedition 335 Scientists, 2012a. Expedition 335 summary. In Teagle, D.A.H., Ildefonse, B., Blum, P., and the Expedition 335 Scientists, *Proc. IODP*, 335: Tokyo (Integrated Ocean Drilling Program Management International, Inc.). doi:10.2204/iodp.proc.335.101.2012
- Expedition 335 Scientists, 2012b. Site 1256. In Teagle, D.A.H., Ildefonse, B., Blum, P., and the Expedition 335 Scientists, *Proc. IODP*, 335: Tokyo (Integrated Ocean Drilling Program Management International, Inc.). doi:10.2204/iodp.proc.335.103.2012
- France, L., Ildefonse, B., and Koepke, J., 2009. Interactions between magma and the hydrothermal system in the Oman ophiolite and in IODP Hole 1256D: fossilisation of dynamic melt lens at fast spreading ridges. *Geochem., Geophys., Geosyst.*, 10(10):Q10019. doi:10.1029/2009GC002652
- Gee, J.S., Tauxe, L., and Constable, C., 2008. AMSSpin: a LabVIEW program for measuring the anisotropy of magnetic susceptibility with the Kappabridge KLY-4S. *Geochem., Geophys., Geosyst.*, 9(8):Q08Y02. doi:10.1029/2008GC001976
- Goldberg, D., 1997. The role of downhole measurements in marine geology and geophysics. *Rev. Geophys.*, 35(3):315–342. doi:10.1029/97RG00221
- Govindaraju, K., 1994. 1994 compilation of working values and sample description for 383 geostandards. *Geostand. Newsl.*, 18(1). doi:10.1111/j.1751-908X.1994.tb00502.x
- Hext, G.R., 1963. The estimation of second-order tensors, with related tests and designs. *Biometrika*, 50(3–4):353–373. doi:10.1093/biomet/50.3-4.353
- Hornby, B.E., Johnson, D.L., Winkler, K.W., and Plumb, R.A., 1989. Fracture evaluation using reflected Stoneley-wave arrivals. *Geophysics*, 54(10):1274–1288. doi:10.1190/1.1442587

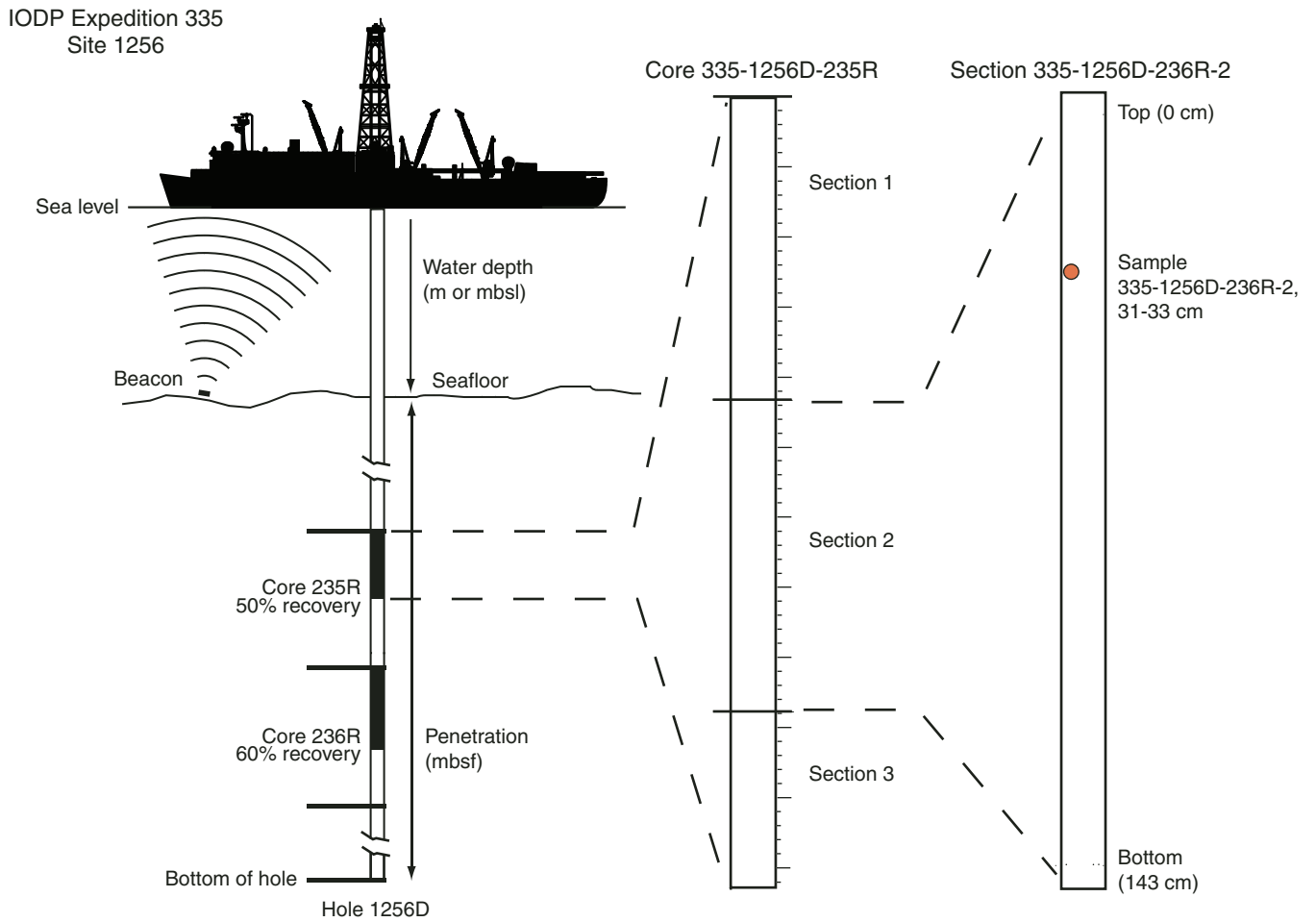


- Imai, N., Terashima, S., Itoh, S., and Ando, A., 1995. 1994 compilation of analytical data for minor and trace elements in seventeen GSJ geochemical reference samples, "igneous rock series." *Geostand. Geoanal. Res.*, 19(2):135–213. doi:10.1111/j.1751-908X.1995.tb00158.x
- Kelemen, P.B., Kikawa, E., Miller, D.J., et al., 2004. *Proc. ODP, Init. Repts.*, 209: College Station, TX (Ocean Drilling Program). doi:10.2973/odp.proc.ir.209.2004
- Kirschvink, J.L., 1980. The least-squares line and plane and the analysis of palaeomagnetic data. *Geophys. J. R. Astron. Soc.*, 62(3):699–718. doi:10.1111/j.1365-246X.1980.tb02601.x
- Koepke, J., Christie, D.M., Dziony, W., Holtz, F., Lattard, D., MacLennan, J., Park, S., Scheibner, B., Yamasaki, T., and Yamazaki, S., 2008. Petrography of the dike–gabbro transition at IDOP Site 1256 (equatorial Pacific): the evolution of the granoblastic dikes. *Geochem., Geophys., Geosyst.*, 9(7):Q07O09. doi:10.1029/2008GC001939
- Kono, M., 1980. Statistics of paleomagnetic inclination data. *J. Geophys. Res., [Solid Earth]*, 85(B7):3878–3882. doi:10.1029/JB085iB07p03878
- Lachenbruch, A.H., and Brewer, M.C., 1959. Dissipation of the temperature effect of drilling a well in Arctic Alaska. *U.S. Geol. Surv. Bull.*, 1083-C:73–106.
- Launeau, P., Archanjo, C.J., Picard, D., Arbaret, L., and Robin, P.-Y., 2010. Two- and three-dimensional shape fabric analysis by the intercept method in grey levels. *Tectonophysics*, 492(1–4):230–239. doi:10.1016/j.tecto.2010.06.005
- Launeau, P., Bouchez, J.-L., and Benn, K., 1990. Shape-preferred orientation of object populations: automatic analysis of digitized images. *Tectonophysics*, 180(2–4): 201–211. doi:10.1016/0040-1951(90)90308-U
- Launeau, P., and Robin, P.-Y.F., 1996. Fabric analysis using the intercept method. *Tectonophysics*, 267(1–4):91–119. doi:10.1016/S0040-1951(96)00091-1
- Le Maitre, R.W., 1989. *A Classification of Igneous Rocks and Glossary of Terms*: Oxford (IUGS, Blackwell).
- Le Maitre, R.W., Streckeisen, A., Zanettin, B., Le Bas, M.J., Bonin, B., Bateman, P., Bellieni, G., Dudek, A., Efremova, S., Keller, J., Lameyre, J., Sabine, P.A., Schmid, R., Sorensen, H., and Woolley, A.R. (Eds.), 2002. *Igneous Rocks: A Classification and Glossary of Terms: Recommendations of the International Union of Geological Sciences Subcommission on the Systematics of Igneous Rocks*: Cambridge (Cambridge Univ. Press).
- Lovell, M.A., Harvey, P.K., Brewer, T.S., Williams, C., Jackson, P.D., and Williamson, G., 1998. Application of FMS images in the Ocean Drilling Program: an overview. In Cramp, A., MacLeod, C.J., Lee, S.V., and Jones, E.J.W. (Eds.), *Geological Evolution of Ocean Basins: Results from the Ocean Drilling Program*. *Geol. Soc. Spec. Publ.*, 131(1):287–303. doi:10.1144/GSL.SP.1998.131.01.18
- MacLeod, C.J., Parson, L.M., and Sager, W.W., 1994. Reorientation of cores using the Formation MicroScanner and Borehole Televiwer: application to structural and paleomagnetic studies with the Ocean Drilling Program. In Hawkins, J., Parson, L., Allan, J., et al., *Proc. ODP, Sci. Results*, 135: College Station, TX (Ocean Drilling Program), 301–309. doi:10.2973/odp.proc.sr.135.160.1994
- McFadden, P.L., and Reid, A.B., 1982. Analysis of paleomagnetic inclination data. *Geophys. J. R. Astron. Soc.*, 69(2):307–319. doi:10.1111/j.1365-246X.1982.tb04950.x
- Merrill, R.T., 1970. Low-temperature treatments of magnetite and magnetite-bearing rocks. *J. Geophys. Res., [Solid Earth]*, 75(17):3343–3349. doi:10.1029/JB075i017p03343
- Morris, A., Gee, J.S., Pressling, N., John, B.E., MacLeod, C.J., Grimes, C.B., and Searle, R.C., 2009. Footwall rotation in an oceanic core complex quantified using reoriented Integrated Ocean Drilling Program core samples. *Earth Planet. Sci. Lett.*, 287(1–2):217–228. doi:10.1016/j.epsl.2009.08.007
- Murray, R.W., Miller, D.J., and Kryc, K.A., 2000. Analysis of major and trace elements in rocks, sediments, and interstitial waters by inductively coupled plasma–atomic emission spectrometry (ICP–AES). *ODP Tech. Note*, 29. doi:10.2973/odp.tn.29.2000
- Orcutt, B., Wheat, C.G., and Edwards, K.J., 2010. Subseafloor ocean crust microbial observatories: development of FLOCS (Flow-Through Osmo Colonization System) and evaluation of borehole construction materials. *Geomicrobiol. J.*, 27(2):143–157. doi:10.1080/01490450903456772
- Orcutt, B.N., Bach, W., Becker, K., Fisher, A.T., Hentscher, M., Toner, B.M., Wheat, C.G., and Edwards, K.J., 2011. Colonization of subsurface microbial observatories deployed in young ocean crust. *ISME J.*, 5:692–703. doi:10.1038/ismej.2010.157
- Parker, R.L., and Gee, J.S., 2002. Calibration of the pass-through magnetometer—II. Application. *Geophys. J. Int.*, 150:140–152. doi:10.1046/j.1365-246X.2002.01692.x
- Passchier, C.W., and Trouw, R.A.J., 1996. *Microtectonics*: Berlin (Springer-Verlag).
- Ramsay, J.G., and Huber, M.I., 1983. *The Techniques of Modern Structural Geology* (Vol. 1): *Strain Analysis*: London (Acad. Press).
- Remaïdi, M., 1993. Etude géochimique de l'association harzburgite, dunite et pyroxénite de l'Arroyo de la Cala (Massif de Ronda, Espagne) [Ph.D. thesis]. Université Montpellier 2, Montpellier, France.
- Révillon, S., Barr, S.R., Brewer, T.S., Harvey, P.K., and Tarnay, J., 2002. An alternative approach using integrated gamma-ray and geochemical data to estimate the inputs to subduction zones from ODP Leg 185, Site 801. *Geochem., Geophys., Geosyst.*, 3(12):8902. doi:10.1029/2002GC000344
- Rider, M.H., 1996. *The Geological Interpretation of Well Logs* (2nd ed.): Caithness (Whittles Publ.).
- Schlumberger, 1989. *Log Interpretation Principles/Applications*: Houston (Schlumberger Educ. Serv.), SMP–7017.
- Serra, O., 1984. *Fundamentals of Well-Log Interpretation* (Vol. 1): *The Acquisition of Logging Data*: Amsterdam (Elsevier).

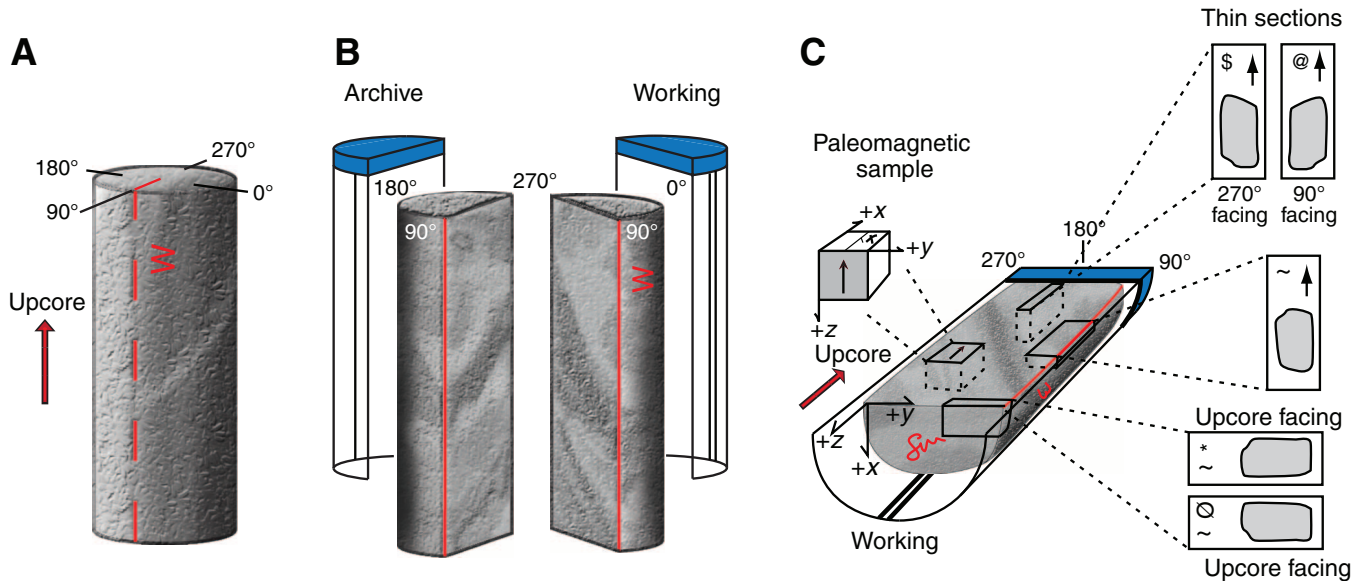
- Serra, O., 1986. *Fundamentals of Well-Log Interpretation* (Vol. 2): *The Interpretation of Logging Data*. Amsterdam (Elsevier).
- Shipboard Scientific Party, 1989. Introduction and explanatory notes. In Robinson, P.T., Von Herzen, R., et al., *Proc. ODP, Init. Repts.*, 118: College Station, TX (Ocean Drilling Program), 3–23. doi:10.2973/odp.proc.ir.118.101.1989
- Shipboard Scientific Party, 1991. Explanatory notes. In Taira, A., Hill, I., Firth, J.V., et al., *Proc. ODP, Init. Repts.*, 131: College Station, TX (Ocean Drilling Program), 25–60. doi:10.2973/odp.proc.ir.131.104.1991
- Shipboard Scientific Party, 1992a. Explanatory notes. In Behrmann, J.H., Lewis, S.D., Musgrave, R.J., et al., *Proc. ODP, Init. Repts.*, 141: College Station, TX (Ocean Drilling Program), 37–71. doi:10.2973/odp.proc.ir.141.105.1992
- Shipboard Scientific Party, 1992b. Explanatory notes. In Dick, H.J.B., Erzinger, J., Stokking, L.B., et al., *Proc. ODP, Init. Repts.*, 140: College Station, TX (Ocean Drilling Program), 5–33. doi:10.2973/odp.proc.ir.140.101.1992
- Shipboard Scientific Party, 1992c. Explanatory notes. In Parson, L., Hawkins, J., Allan, J., et al., *Proc. ODP, Init. Repts.*, 135: College Station, TX (Ocean Drilling Program), 49–79. doi:10.2973/odp.proc.ir.135.102.1992
- Shipboard Scientific Party, 1993a. Explanatory notes. In Alt, J.C., Kinoshita, H., Stokking, L.B., et al., *Proc. ODP, Init. Repts.*, 148: College Station, TX (Ocean Drilling Program), 5–24. doi:10.2973/odp.proc.ir.148.101.1993
- Shipboard Scientific Party, 1993b. Explanatory notes. In Gillis, K., Mével, C., Allan, J., et al., *Proc. ODP, Init. Repts.*, 147: College Station, TX (Ocean Drilling Program), 15–42. doi:10.2973/odp.proc.ir.147.102.1993
- Shipboard Scientific Party, 1995. Explanatory notes. In Cannat, M., Karson, J.A., Miller, D.J., et al., *Proc. ODP, Init. Repts.*, 153: College Station, TX (Ocean Drilling Program), 15–42. doi:10.2973/odp.proc.ir.153.10X.1995
- Shipboard Scientific Party, 1999a. Explanatory notes. In Dick, H.J.B., Natland, J.H., Miller, D.J., et al., *Proc. ODP, Init. Repts.*, 176: College Station, TX (Ocean Drilling Program), 1–42. doi:10.2973/odp.proc.ir.176.102.1999
- Shipboard Scientific Party, 1999b. Site 735. In Dick, H.J.B., Natland, J.H., Miller, D.J., et al., *Proc. ODP, Init. Repts.*, 176: College Station, TX (Ocean Drilling Program), 1–314. doi:10.2973/odp.proc.ir.176.103.1999
- Shipboard Scientific Party, 2003. Explanatory notes. In Wilson, D.S., Teagle, D.A.H., Acton, G.D., *Proc. ODP, Init. Repts.*, 206: College Station, TX (Ocean Drilling Program), 1–94. doi:10.2973/odp.proc.ir.206.102.2003
- Shipboard Scientific Party, 2004. Explanatory notes. In Kelemen, P.B., Kikawa, E., Miller, D.J., et al., *Proc. ODP, Init. Repts.*, 209: College Station, TX (Ocean Drilling Program), 1–75. doi:10.2973/odp.proc.ir.209.102.2004
- Smith, D.C., Spivack, A.J., Fisk, M.R., Haveman, S.A., Staudigel, H., and the Leg 185 Shipboard Scientific Party, 2000. Methods for quantifying potential microbial contamination during deep ocean coring. *ODP Tech. Note*, 28. doi:10.2973/odp.tn.28.2000
- Sparks, J.W., and Zuleger, E., 1995. Data report: chemical analyses of the Leg 140 reference sample. In Erzinger, J., Becker, K., Dick, H.J.B., Stokking, L.B. (Eds.), *Proc. ODP, Sci. Results*, 137/140: College Station, TX (Ocean Drilling Program), 353–355. doi:10.2973/odp.proc.sr.137140.041.1995
- Streckeisen, A., 1974. Classification and nomenclature of plutonic rocks recommendations of the IUGS subcommission on the systematics of igneous rocks. *Geol. Rundsch.*, 63(2):773–786. doi:10.1007/BF01820841
- Teagle, D.A.H., Alt, J.C., Umino, S., Miyashita, S., Banerjee, N.R., Wilson, D.S., and Expedition 309/312 Scientists, 2006. *Proc. IODP*, 309/312: Washington, DC (Integrated Ocean Drilling Program Management International, Inc.). doi:10.2204/iodp.proc.309312.2006
- Twiss, R.J., and Moores, E.M., 1992. *Structural Geology*: New York (Freeman).
- Vasiliev, M.A., Blum, P., Chubarian, G., Olsen, R., Bennignt, C., Cobine, T., Fackler, D., Hastedt, M., Houpt, D., Mateo, Z., and Vasilieva, Y.B., 2011. A new natural gamma radiation measurement system for marine sediment and rock analysis. *J. Appl. Geophys.*, 75:455–463. doi:10.1016/j.jappgeo.2011.08.008
- Wilson, D.S., Teagle, D.A.H., Acton, G.D., et al., 2003. *Proc. ODP, Init. Repts.*, 206: College Station, TX (Ocean Drilling Program). doi:10.2973/odp.proc.ir.206.2003
- Yu, Y., Dunlop, D.J., and Özdemir, Ö., 2003. On the resolution of multivectorial remanences. *Earth Planet. Sci. Lett.*, 208(1–2):13–26. doi:10.1016/S0012-821X(02)01149-4

**Publication:** 3 June 2012  
**MS 335-102**

**Figure F1.** Integrated Ocean Drilling Program (IODP) labeling scheme used for holes, cores, and sections, Expedition 335. mbsl = meters below sea level.



**Figure F2.** Core reference frame for structural and paleomagnetic orientation measurements, Expedition 335. **A.** The primary orientation of each core piece is up and down along the core axis. **B.** Coordinates in both archive and working section halves. **C.** Conventions for labeling samples and thin sections taken from the working section half.





**Figure F3.** Summary of the core handling and work flow, from coring to shipboard sampling, Expedition 335. For more information on Step 6, see Figure F2. Cur = Curator, ALO = Assistant Laboratory Officer, Struc. = structural geologists, Ig. Pet. = igneous petrologists, Phys. Props. = physical properties specialist, Ig. = igneous petrologists, Alt. = alteration specialists, TSB = thin section billet, XRD = X-ray diffraction sample, ICP = ICP-AES sample, Mag = paleomagnetism sample, PP = physical properties sample.

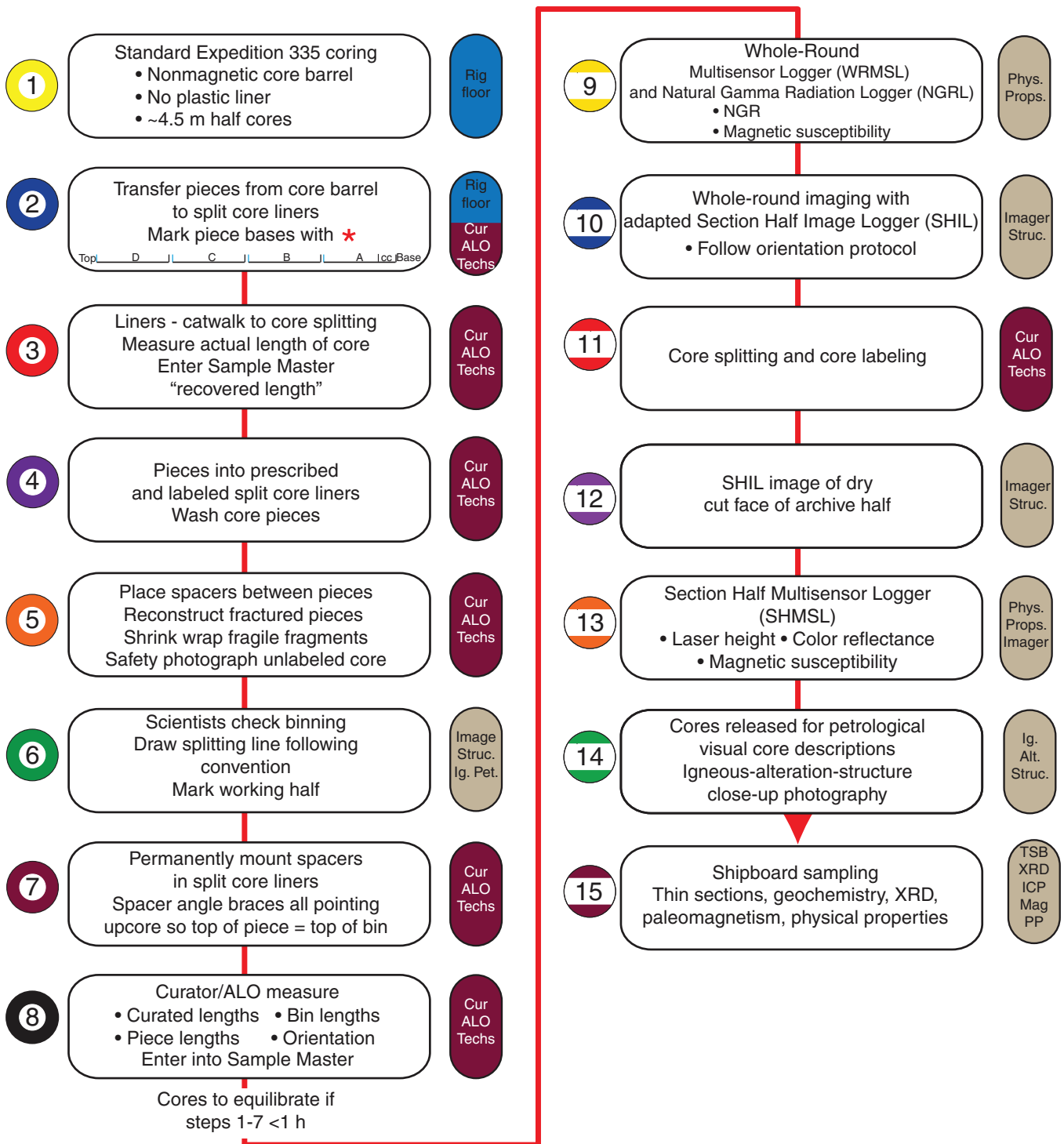
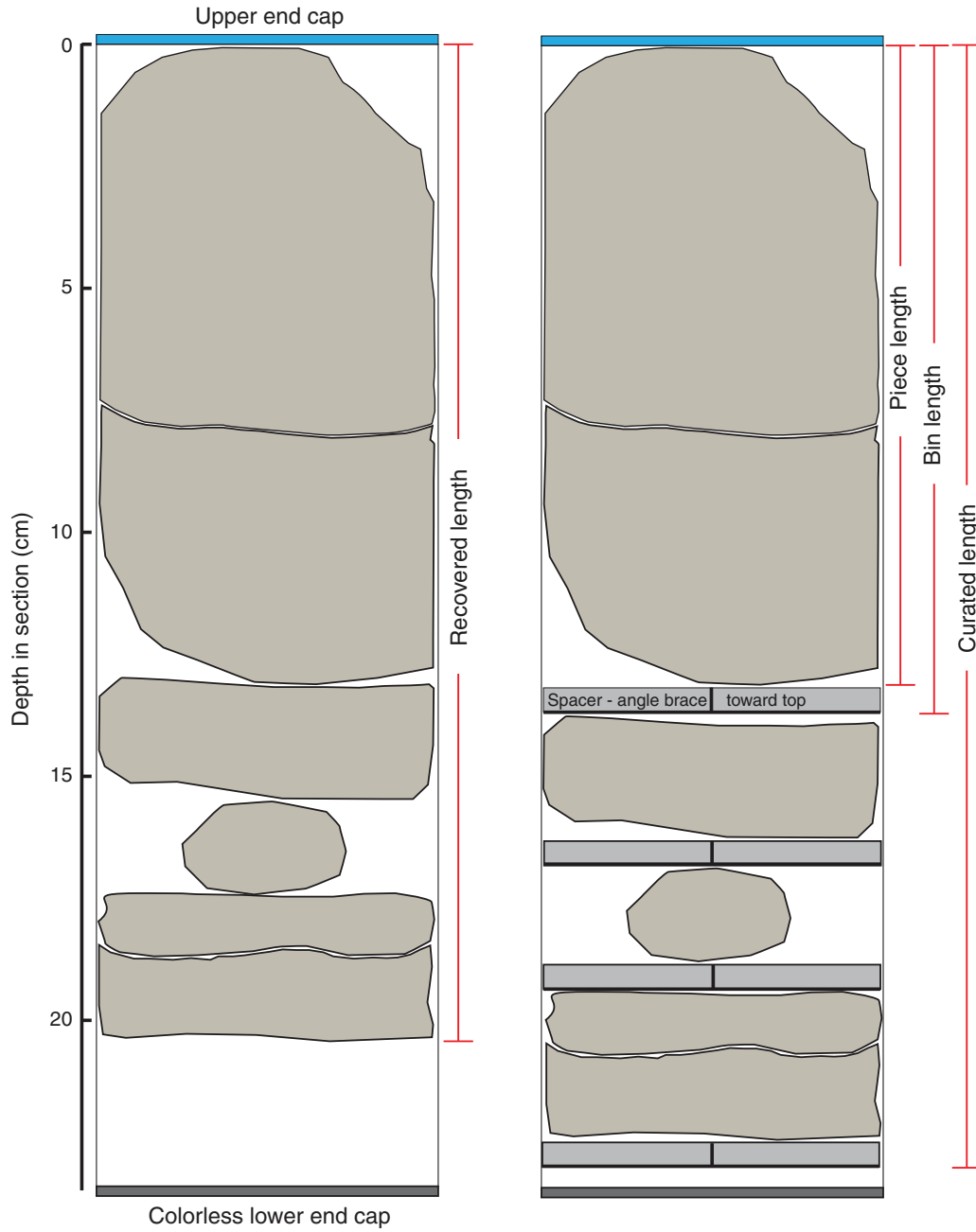


Figure F4. Piece and section lengths defined for curation and scientific purposes, Expedition 335.



**Figure F5.** Data flow diagram displaying major information capture applications, central LIMS database, data retrieval applications (light green), graphing applications (red), and final documents generated for the Expedition 335 *Proceedings* (yellow). All information is stored in the LIMS database before it is extracted and used for reporting. SHLF = section half, WR = whole round, CSV = comma-separated value, VCD = visual core description.

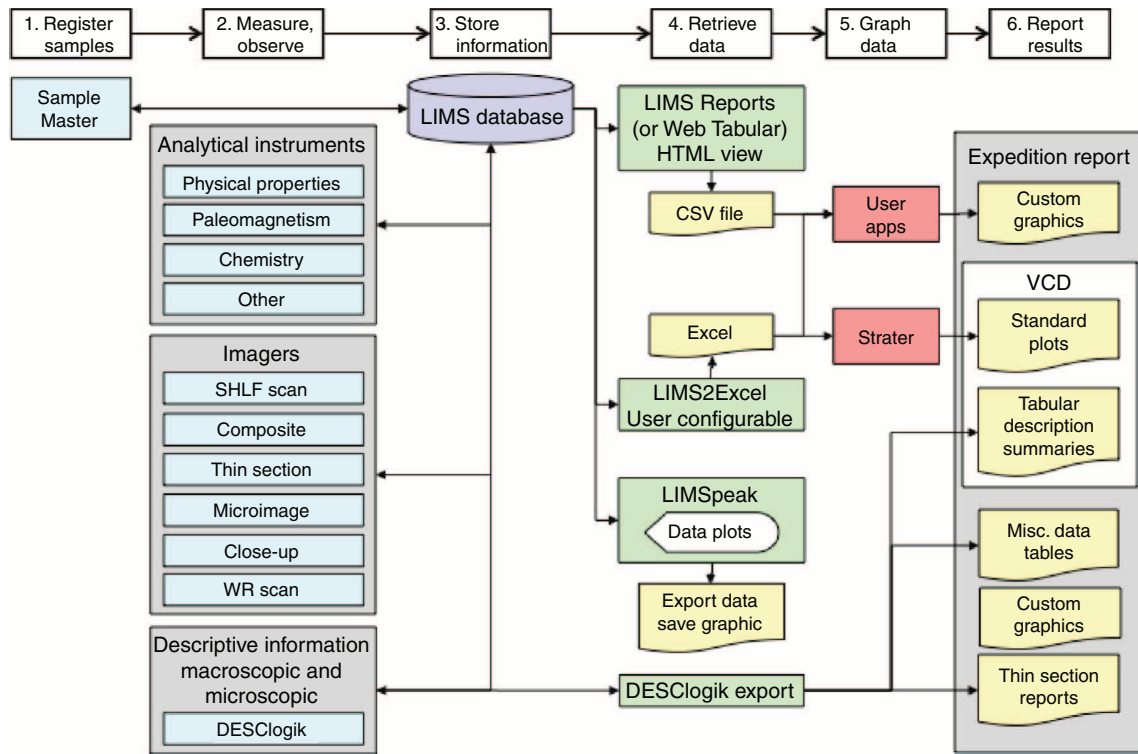
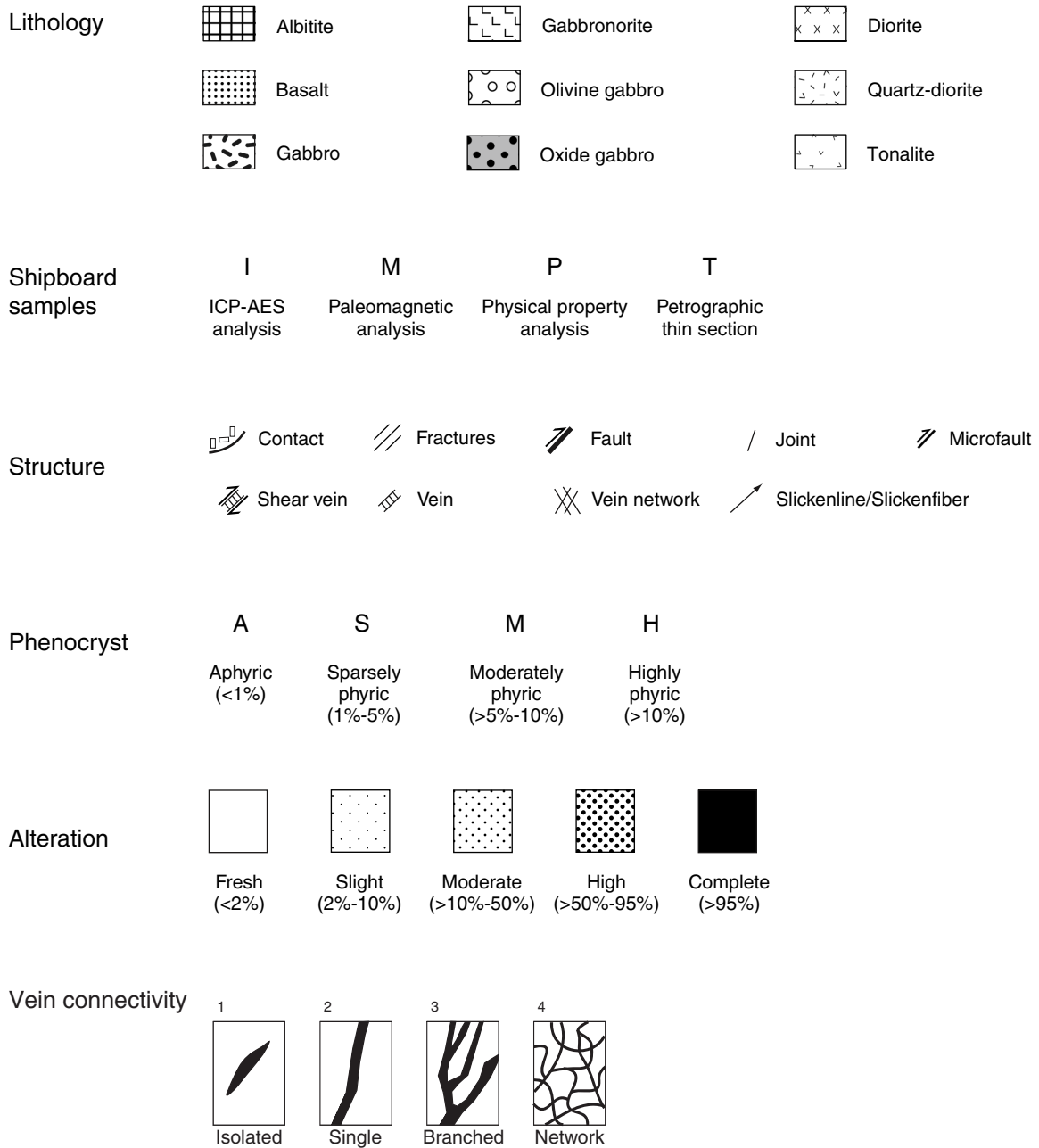
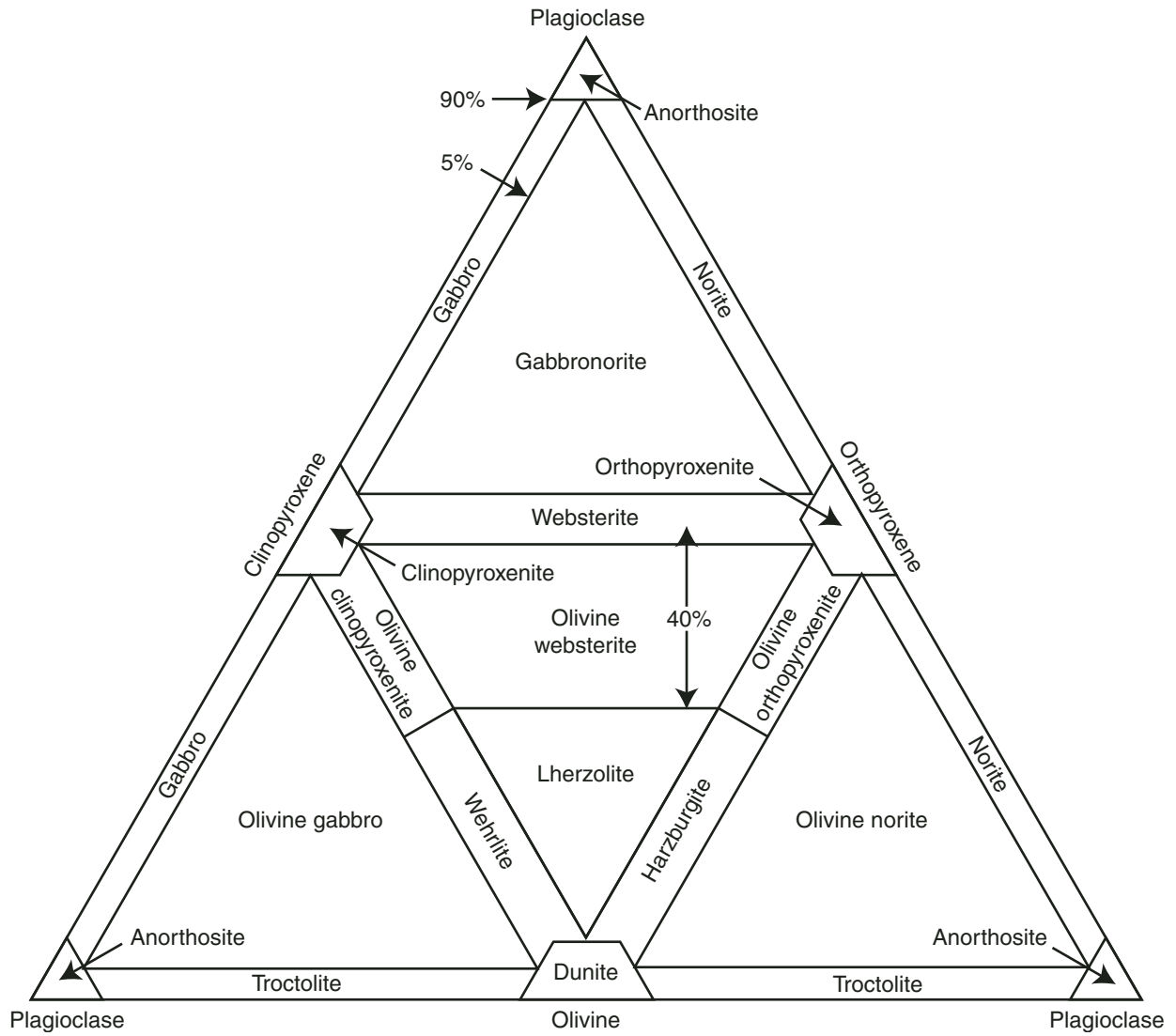


Figure F6. Symbols and abbreviations used in VCDs produced during Expedition 335.

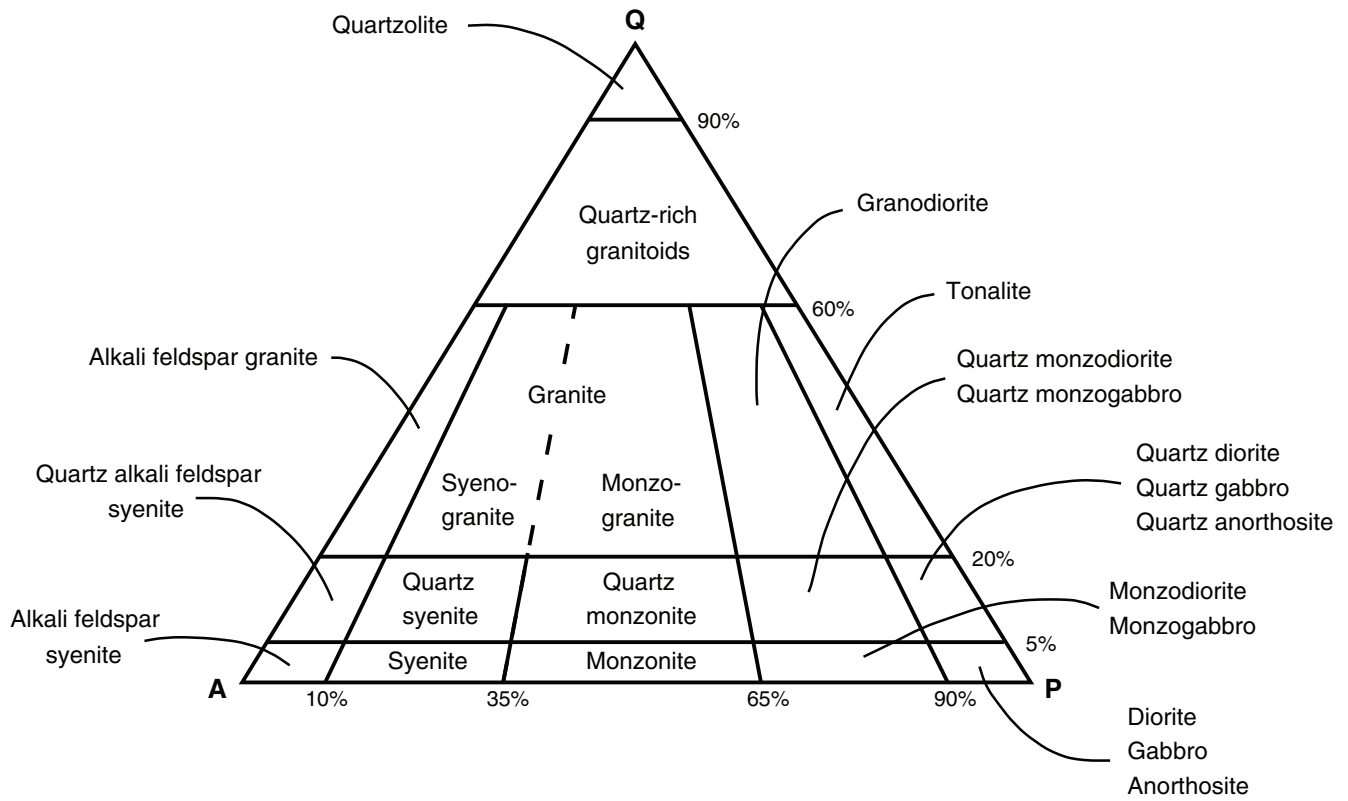




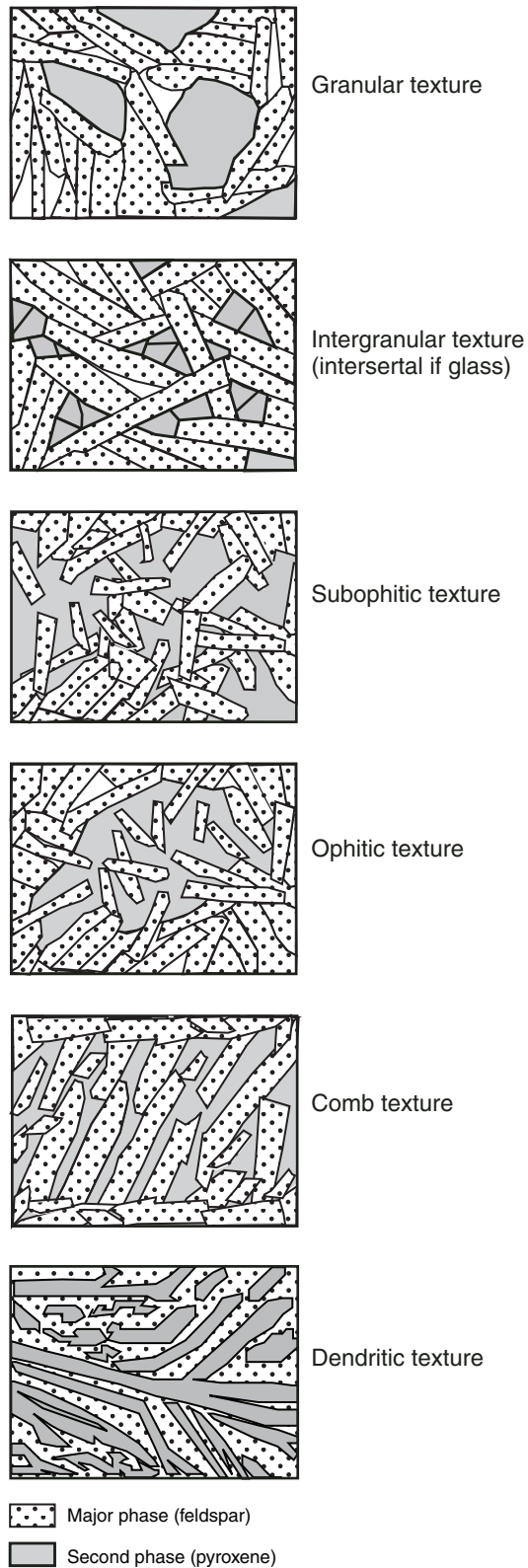
**Figure F7.** Modal classification scheme for mafic-ultramafic plutonic igneous rocks used during Expedition 335 (after Streckeisen, 1974).



**Figure F8.** Quartz-alkali feldspar-plagioclase (QAP) modal classification scheme for plutonic igneous rocks used during Expedition 335 (from Le Maitre et al., 2002).

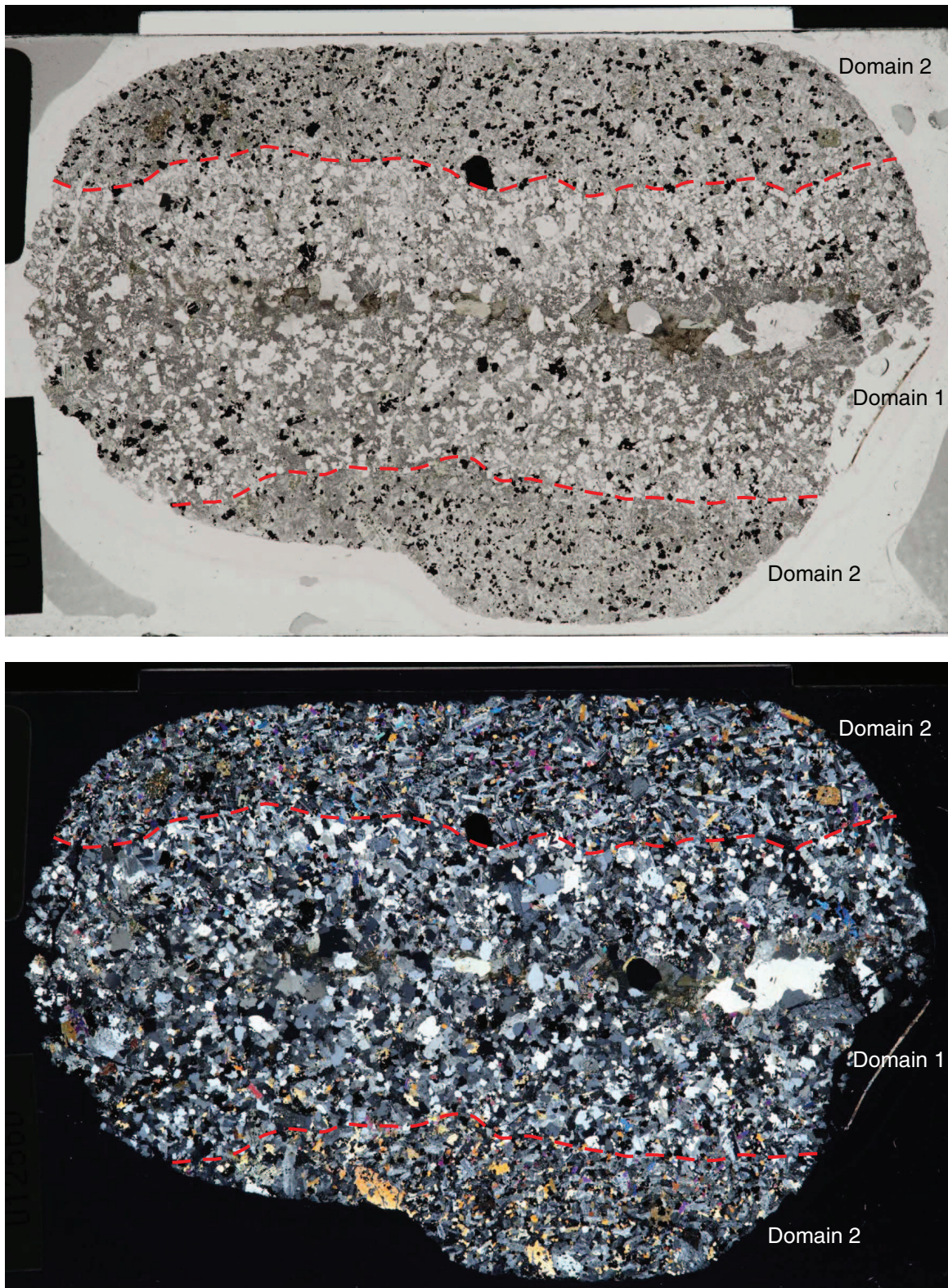


**Figure F9.** Textural classification for igneous rocks used during Expedition 335 (modified from Cordier et al., 2005).





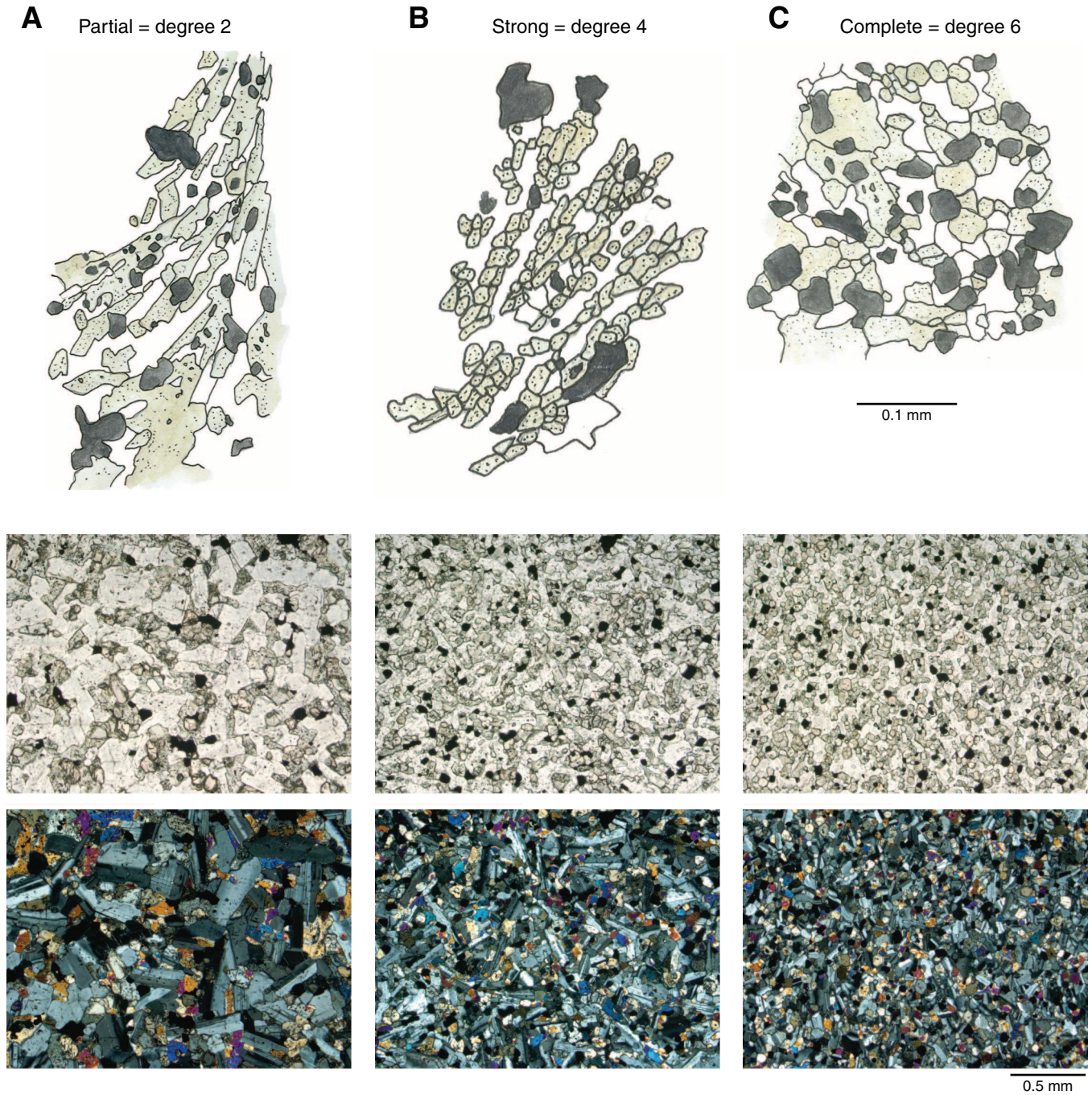
**Figure F10.** Example of full thin section photomicrographs under plane-polarized (top) and cross-polarized (bottom) light in which multiple domains were defined, Expedition 335.



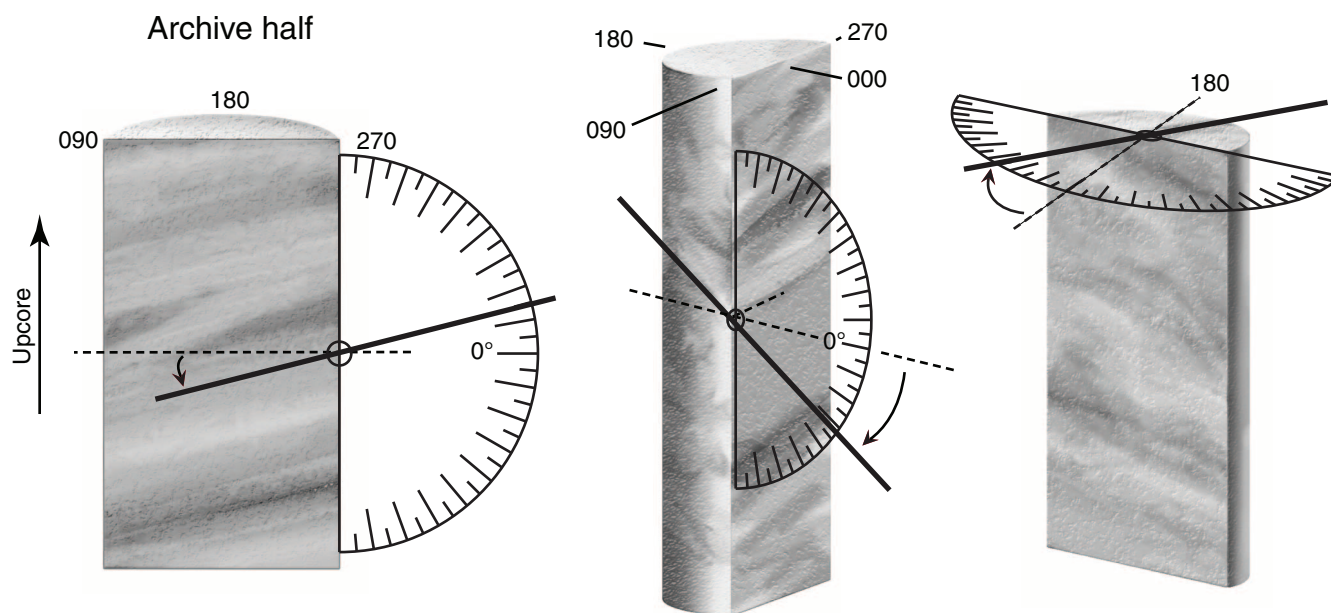
Sample 335-1256D-235R-1, 23-25 cm (Thin Section 3)



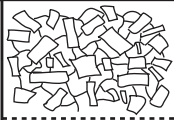
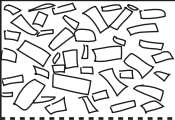
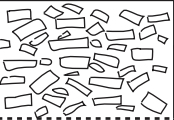
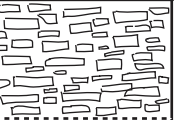
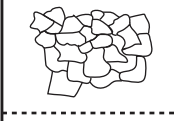
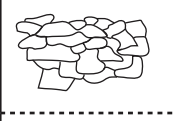
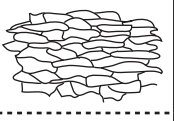
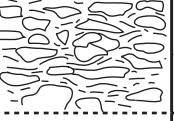
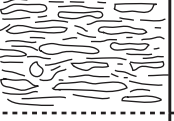
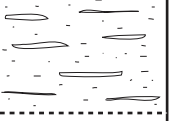

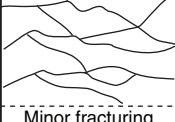
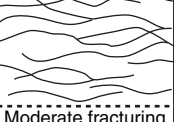


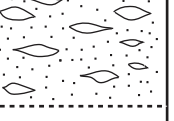
**Figure F11.** Recrystallization degree scale used during Expedition 335 following the methods of Teagle, Alt, Umino, Miyashita, Banerjee, Wilson, and the Expedition 309/312 Scientists (2006): 0 = no recrystallization, 2 = slightly recrystallized, 4 = strongly recrystallized, and 6 = completely recrystallized. Original sketches by C. Laverne.



**Figure F12.** Reference frame and method of measuring a planar feature used to describe the orientation of observed structures, Expedition 335.



**Figure F13.** Intensity and intensity rank for magmatic fabrics, crystal-plastic fabrics, and cataclastic deformation fabrics, Expedition 335.

Feature	Rank					
	0	1	2	3	4	5
Magmatic foliation						
	Isotropic: no shape fabric	Weak shape fabric	Moderate shape fabric	Strong shape fabric		
Gabbro crystal-plastic deformation						
	Undeformed	Weakly foliated	Strongly foliated	Porphyroclastic (Protomylonite)	Mylonite	Ultramylonite
Cataclastic deformation						
	Undeformed	Minor fracturing No sig. grain size reduction	Moderate fracturing No sig. grain size reduction	Dense anastomosing fracturing and incipient brecciation (<20% matrix)	Well-developed fault brecciation: clast rotation (20%-70% matrix)	Cataclasite (>70% matrix)



**Figure F14.** Image processing for quantitative shape-preferred orientation (SPO) analysis, Expedition 335. DN = digital number.

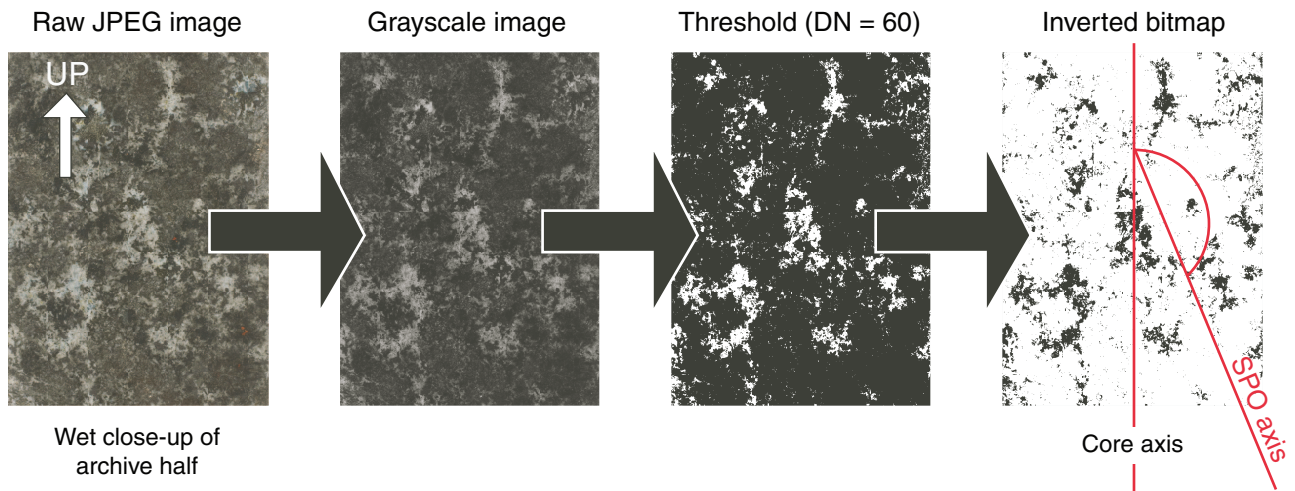




Figure F15. Operation of and settings for the “Intercepts” program (Launeau et al., 1990, 2010; Launeau and Robin, 1996) used in shape-preferred orientation (SPO) analysis, Expedition 335.

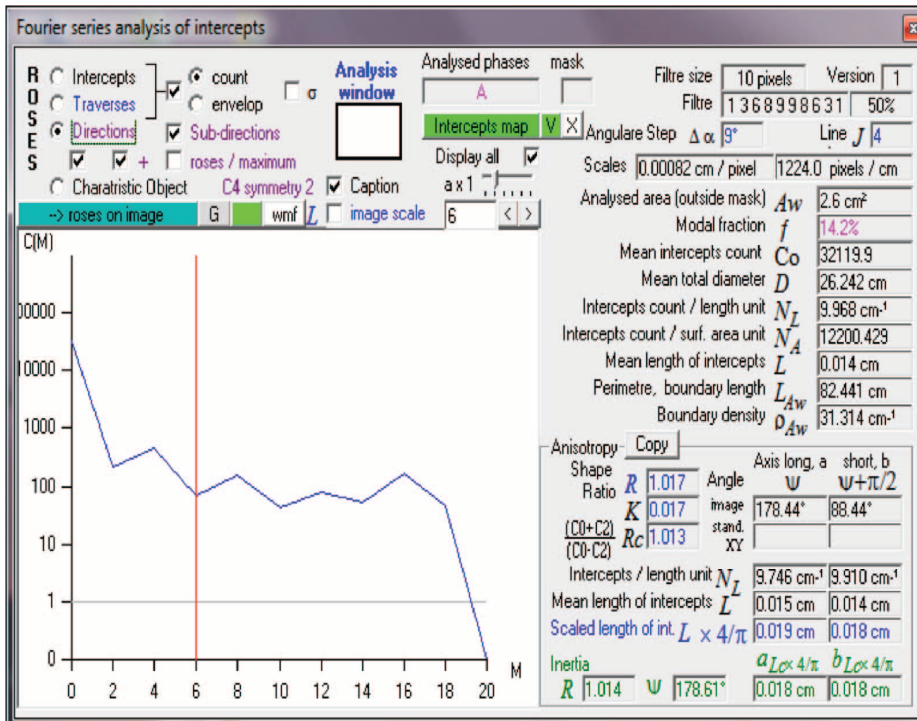
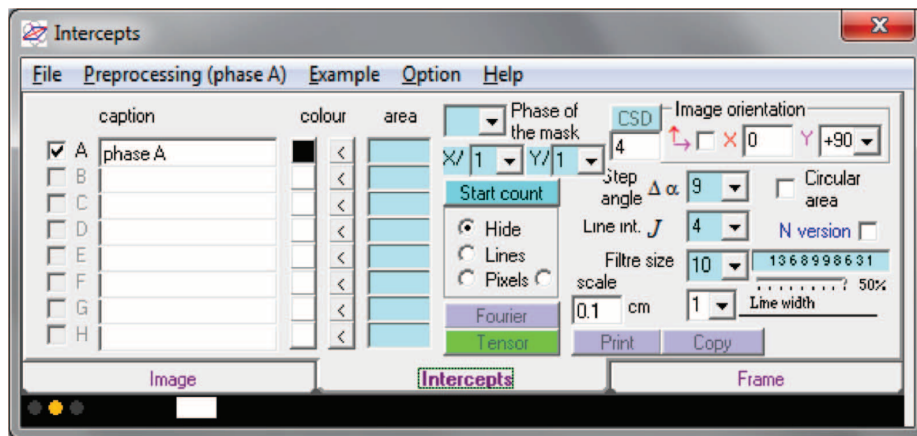
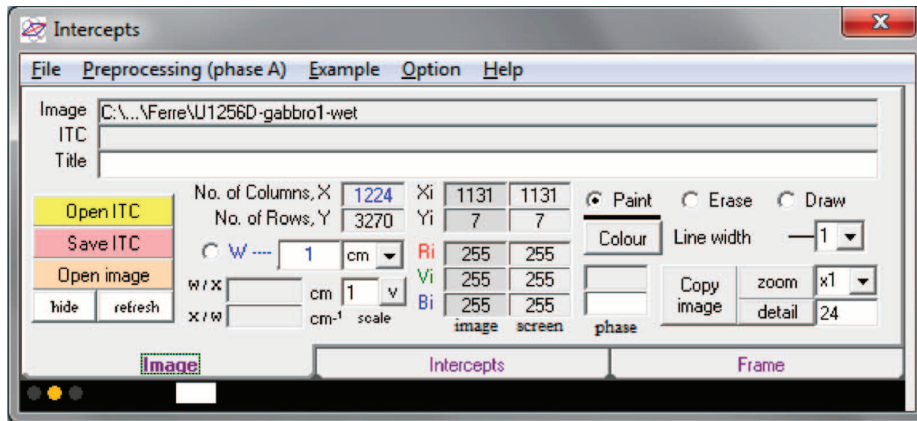
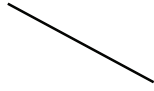



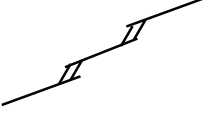

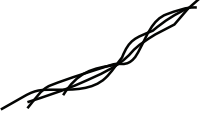
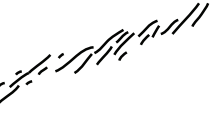
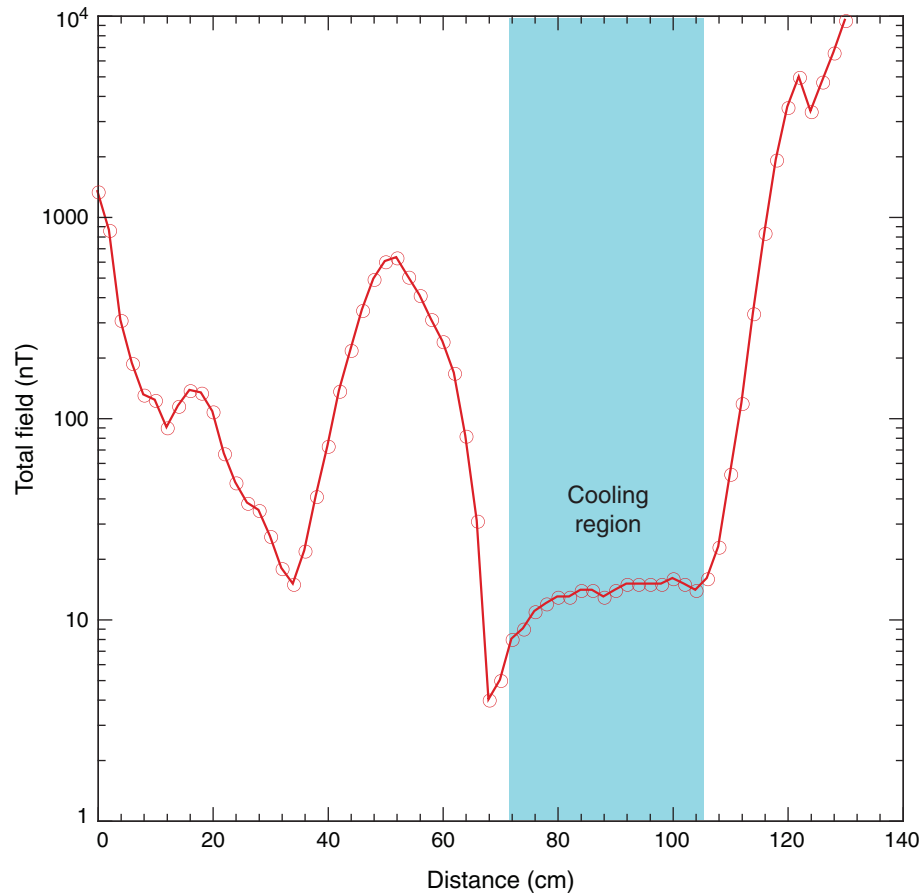


Figure F16. Morphologies of fractures and fracture network, Expedition 335.

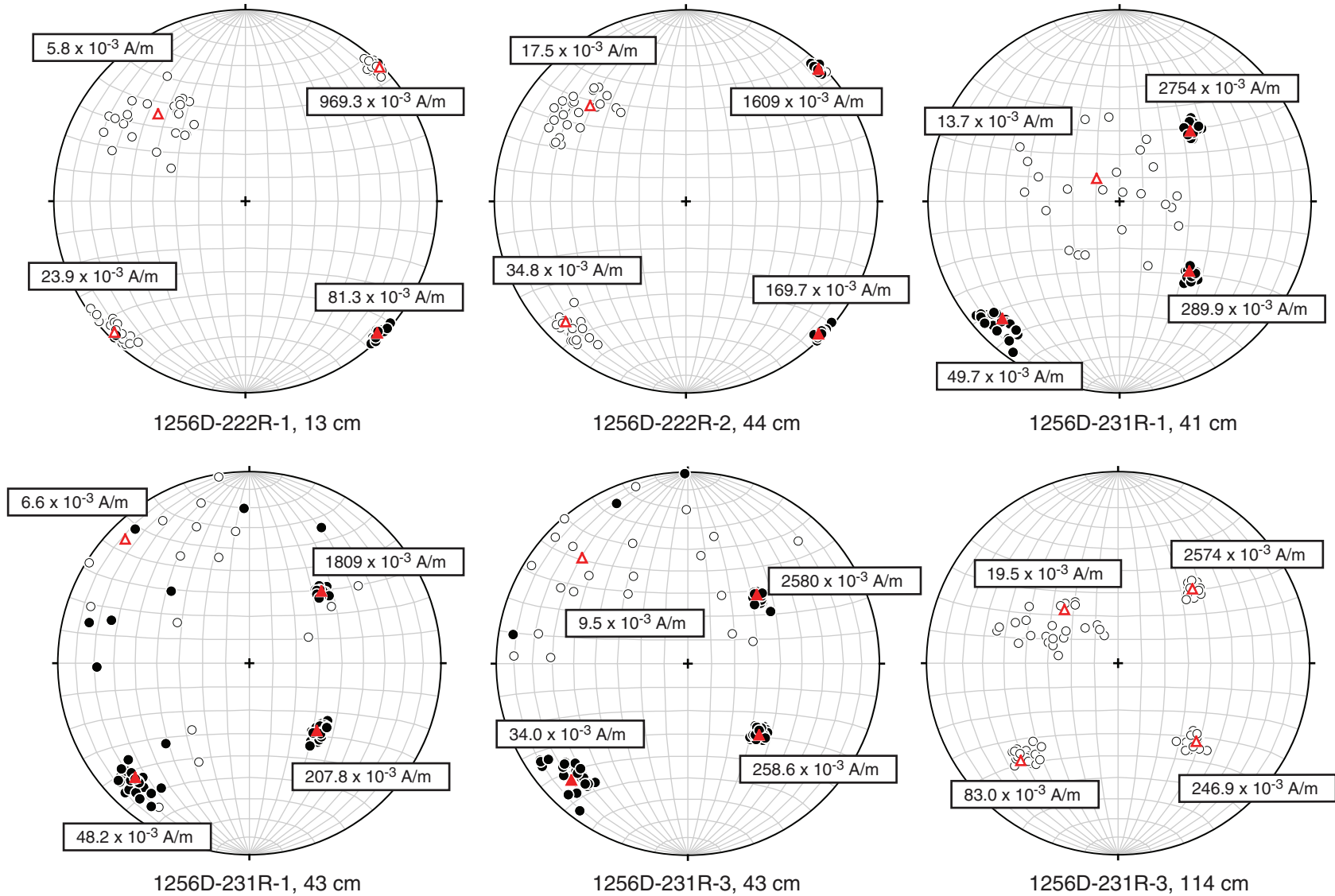
Fracture morphology		Planar		Curved		Irregular		Y-shaped
	No open fractures							
Fracture morphology/ Network		Stepped		Splayed		Anastomosing		Riedel array

**Figure F17.** Total magnetic field profile through the Schonstedt TSD-1 thermal demagnetizer, measured with an Applied Physics 3-axis fluxgate sensor while the *JOIDES Resolution* was at Site 1256 with a ship orientation of  $230^\circ$  (i.e., with the TSD-1 axis oblique to the local geomagnetic field direction). Survey conducted on 27 April 2011.



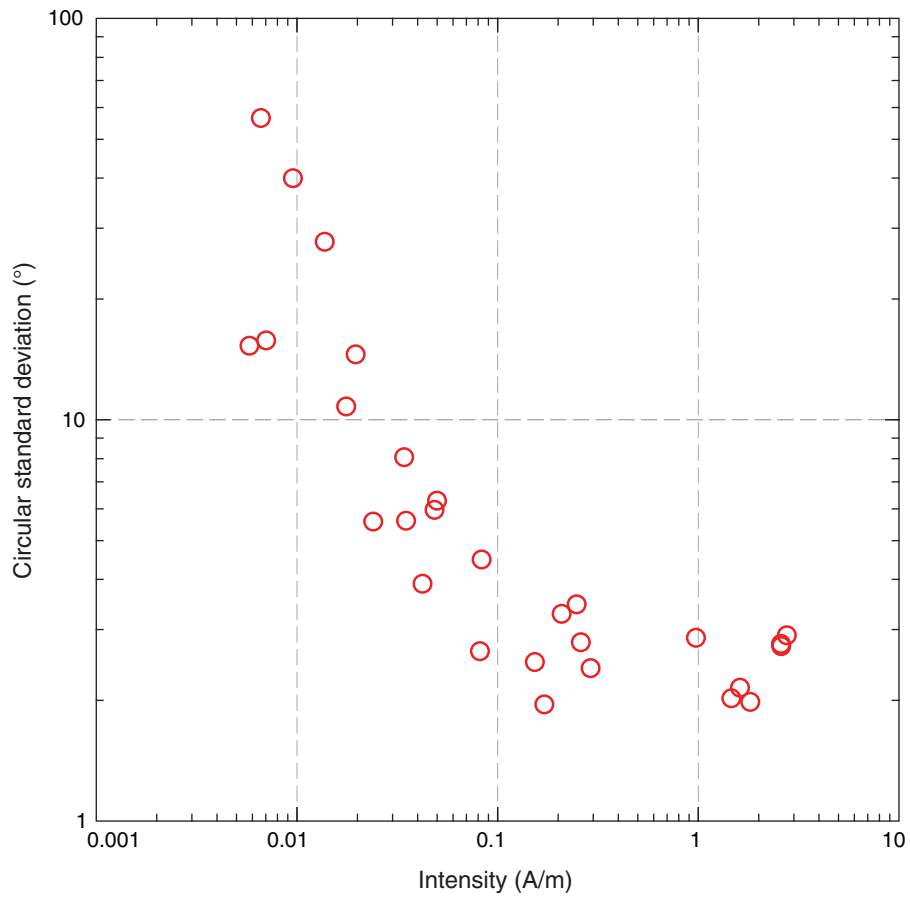


**Figure F18.** Equal area stereographic projections showing the distributions of remanence directions for individual samples measured in each of 24 positions on the superconducting rock magnetometer (SRM) at varying levels of remanence intensity, Hole 1256D. Note the increase in directional scatter as intensity decreases. Black symbols = SRM data, red symbols = AGICO JR-6A data used as a reference. Solid/open symbols represent directions on the lower/upper hemispheres, respectively.

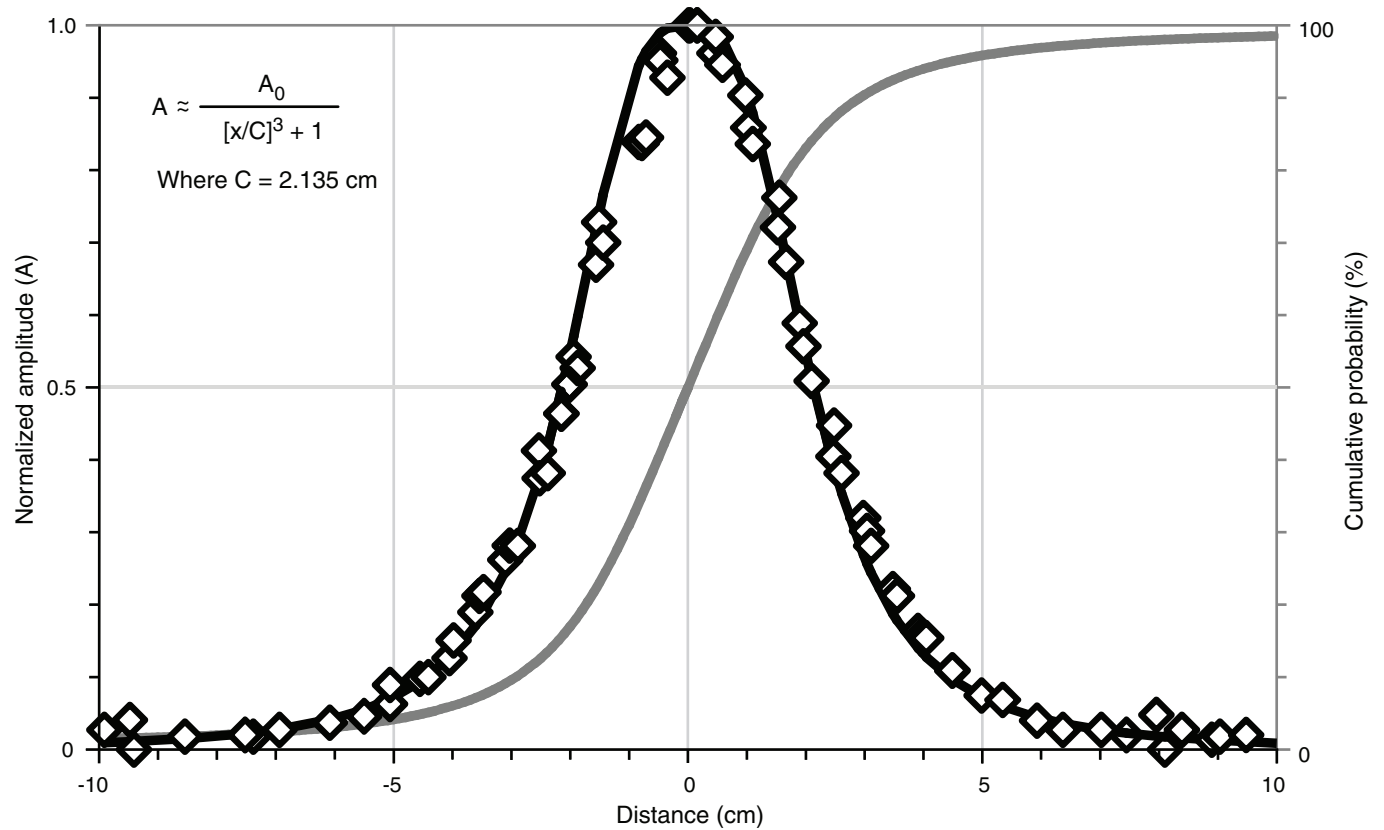




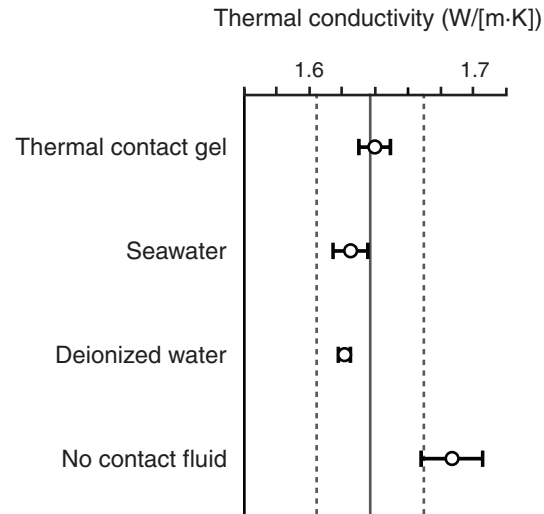
**Figure F19.** Relationship between circular standard deviation of distributions of remanence directions for individual samples measured in each of 24 positions on the superconducting rock magnetometer and remanence intensity, Hole 1256D.



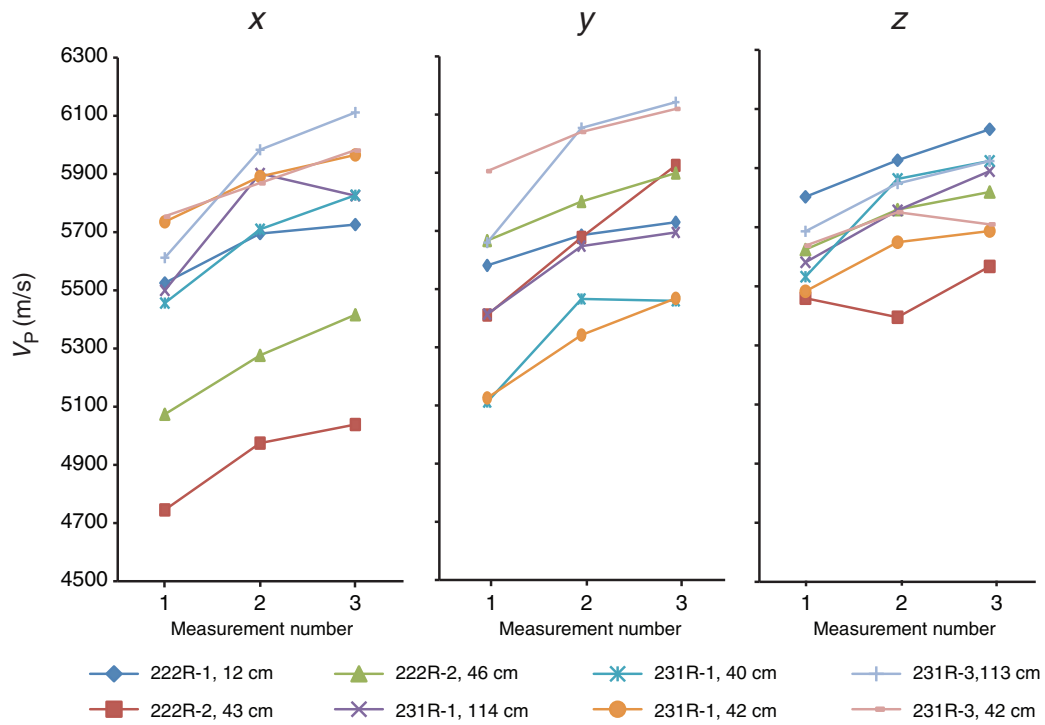
**Figure F20.** Normalized response curve of the MS2C Bartington magnetic susceptibility meter on the WRMSL (modified after Blum, 1997), Expedition 335. Normalized amplitude ( $A$ ) of magnetic susceptibility of thin discs against distance from the center of the MS2C coil ( $x$ ). Amplitudes are normalized against the peak value at zero distance. Black line shows fitted curve based on the inset equation, where the fitted scaling length ( $C$ ) is about one-fourth of the coil diameter. Gray line shows the cumulative probability function for the fitted curve, indicating that 90% of the measured signal is sourced from within ~4 cm of the coil.



**Figure F21.** Effect of different contact fluids on the measured thermal conductivity of the MACOR standard ( $k = 1.637\% \pm 2\%$ ), Expedition 335. Errors bars are  $1\sigma$  of 10 repeat measurements. Solid line = certified thermal conductivity, dashed lined = 2% error limit on the certified thermal conductivity. Measurements made without a contact fluid often fall outside of the instrument 2% accuracy limits.

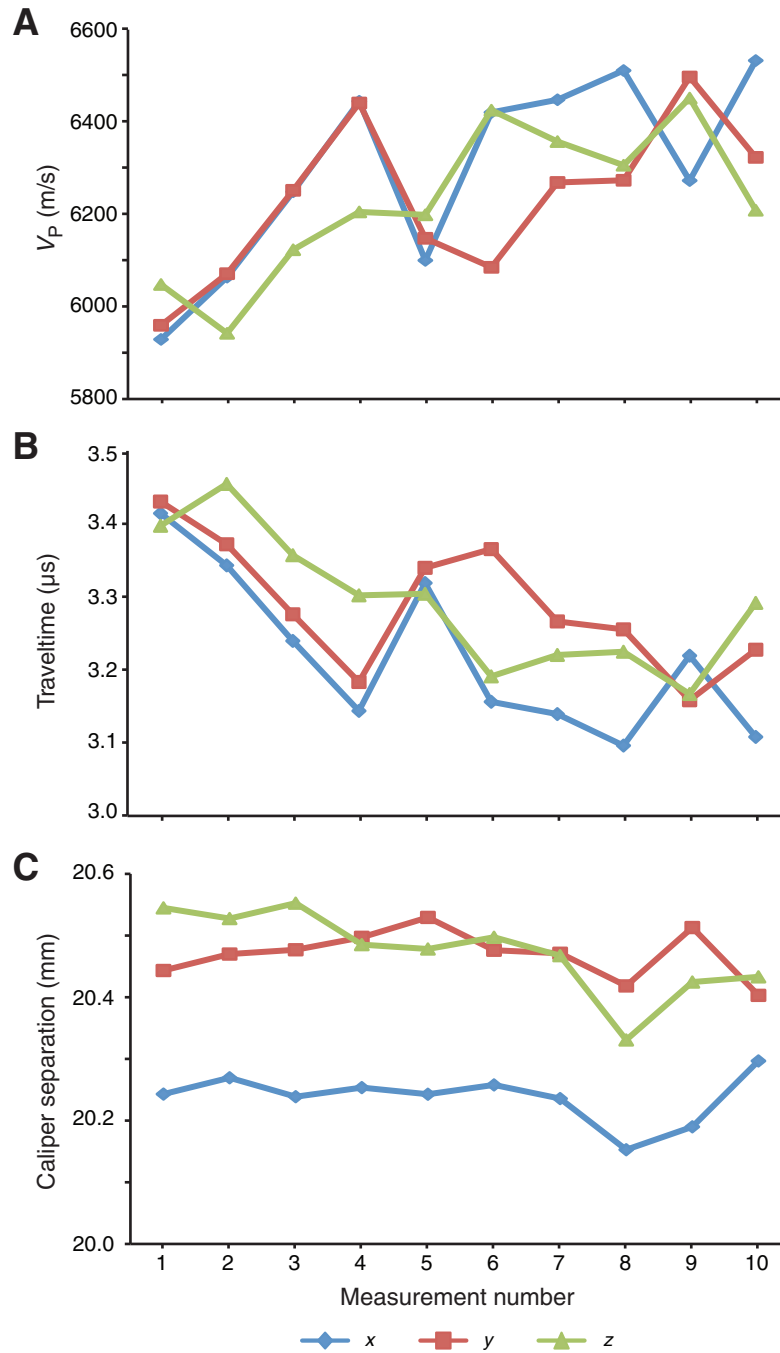


**Figure F22.** *P*-wave velocity in three orthogonal directions (*x*, *y*, and *z*) versus sequential number of measurement for eight different minicubes, Expedition 335. Each measurement was conducted following Expedition 312 protocol (deionized water added on the cube surface). Note large variations and persistent upward trend.

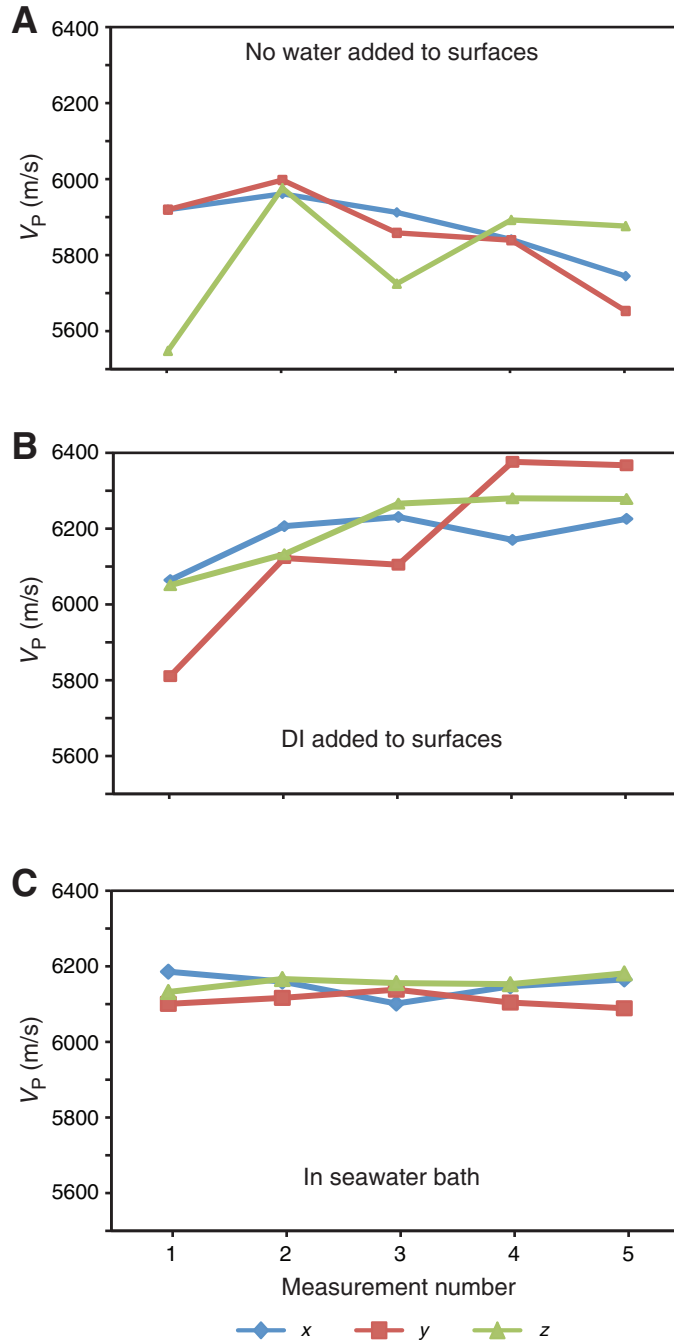




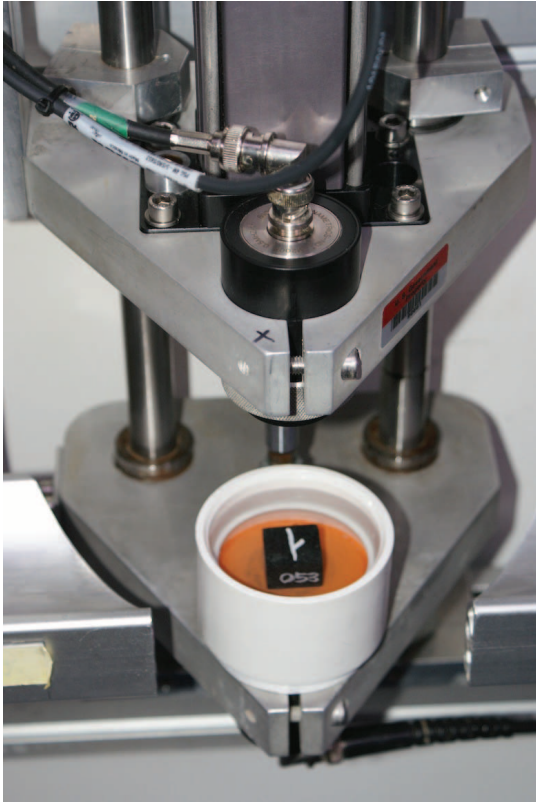
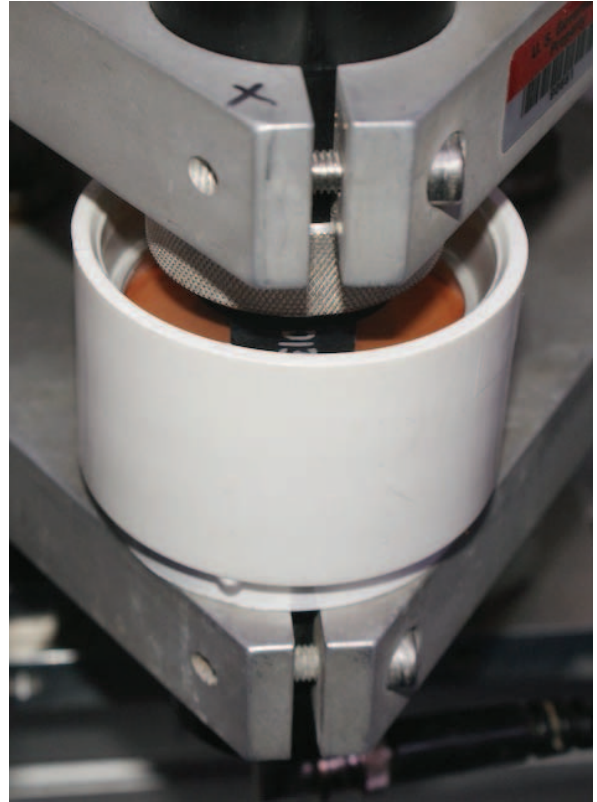
**Figure F23.** (A) *P*-wave velocity in three orthogonal directions, (B) corresponding traveltime, and (C) caliper separation for one minicube (Sample 335(312)-231R-3W, 52–54 cm; PP/PMAG CUBE3215471) measured 10 times, following Expedition 312 protocol (deionized water added on the cube surface). Note relatively stable caliper record but consistent trends in traveltime and velocity.



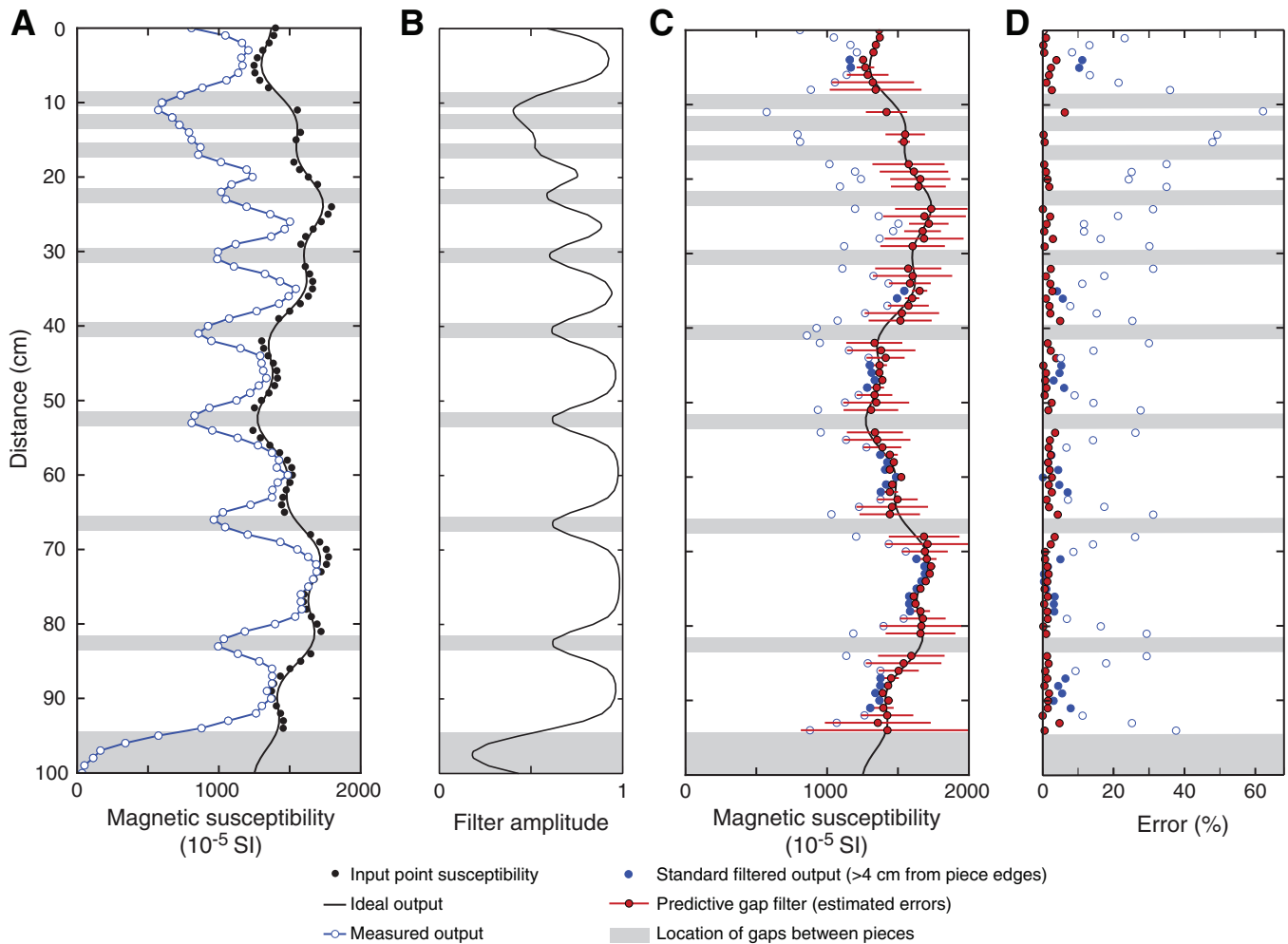
**Figure F24.** *P*-wave velocity in three orthogonal directions obtained on a minicube (Sample 335(312)-231R-3W, 52–54 cm; PP/PMAG CUBE3215471) under different saturation conditions (after initial 24 h saturation in seawater under vacuum). **A.** Wiped surfaces, no water added. **B.** Cube soaked in seawater, no excess water removed from surfaces before measurement, deionized water (DI) added to surfaces. **C.** Cube fully submerged in seawater bath during measurement (velocity value before correction for the effect of container). Note the excellent repeatability in case C.



**Figure F25.** A “bath” container for compression velocity measurements on discrete samples fully submerged in seawater, Expedition 335. **A.** Gantry caliper in the open position before the measurement. **B.** Gantry caliper closed on a minicube submerged in seawater.

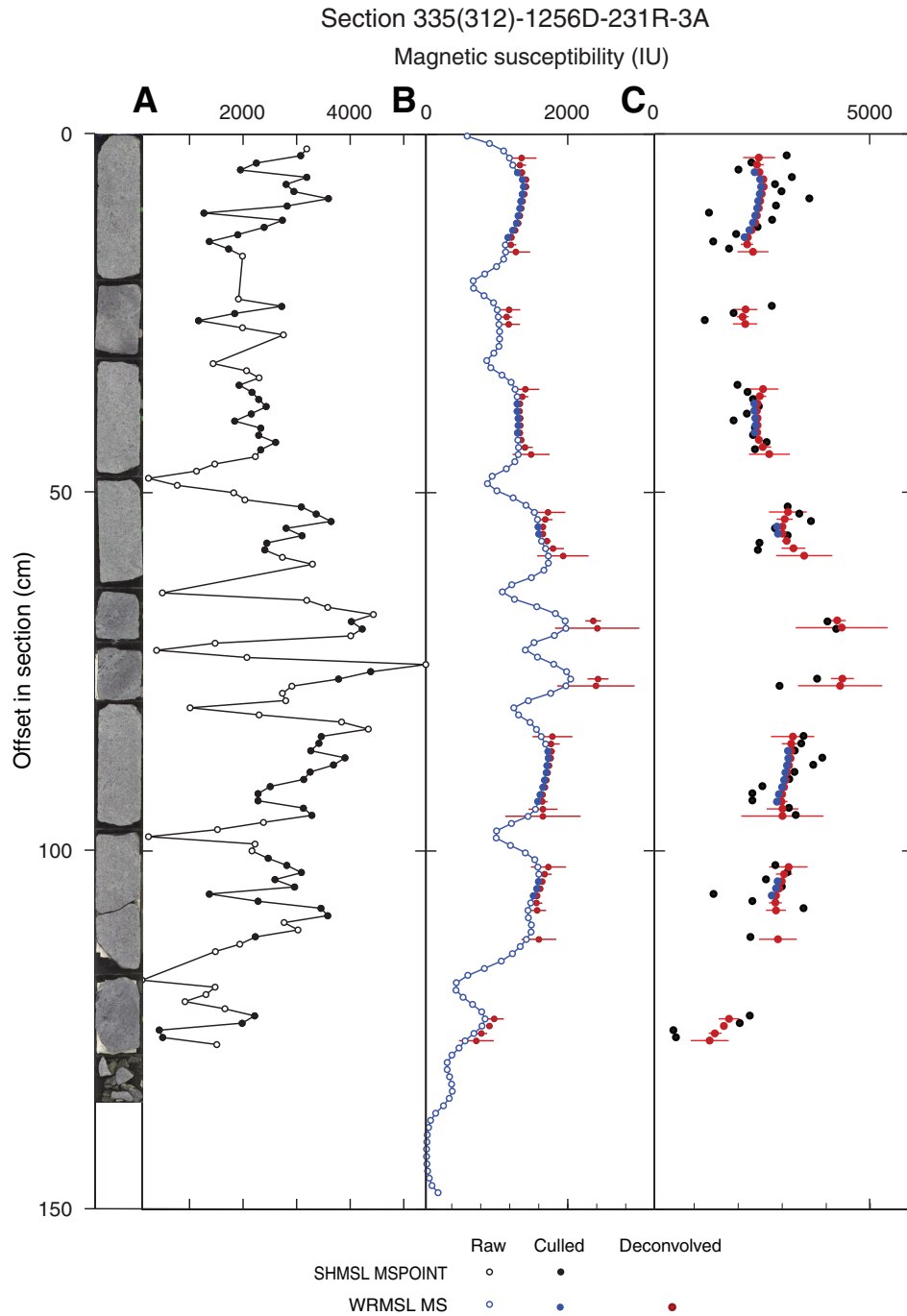
**A****B**

**Figure F26.** Synthetic test of gap filtering algorithm, Expedition 335. **A.** Input magnetic susceptibility (black circles) defined as a function of offset ( $z$ ) by  $\kappa(z) = 1500 - 200\cos(\pi z/25) + 100\cos(0.17\pi z)$ . Ideal output susceptibility (black line) defined by convolving  $\kappa(z)$  with the instrument response curve (Fig. F20). Measured output (open blue circles and blue line) defined by setting the input function to zero at gaps and convolving with the instrument response curve; random Gaussian noise with 10 nT standard deviation is added to the computed data. **B.** Amplitude of the predictive gap filter. **C.** Results of gap filtering; all data from gaps have been removed. Ideal output and measured output as in A; results of culling data <4 cm from piece edges (solid blue circles) and deconvolving data (red circles) using the predictive gap filter shown in B. Error bars are calculated from the maximum variation associated with mislocating the gaps by 1 cm. **D.** Percentage error in the measured and filtered data. (See text for further discussion.)

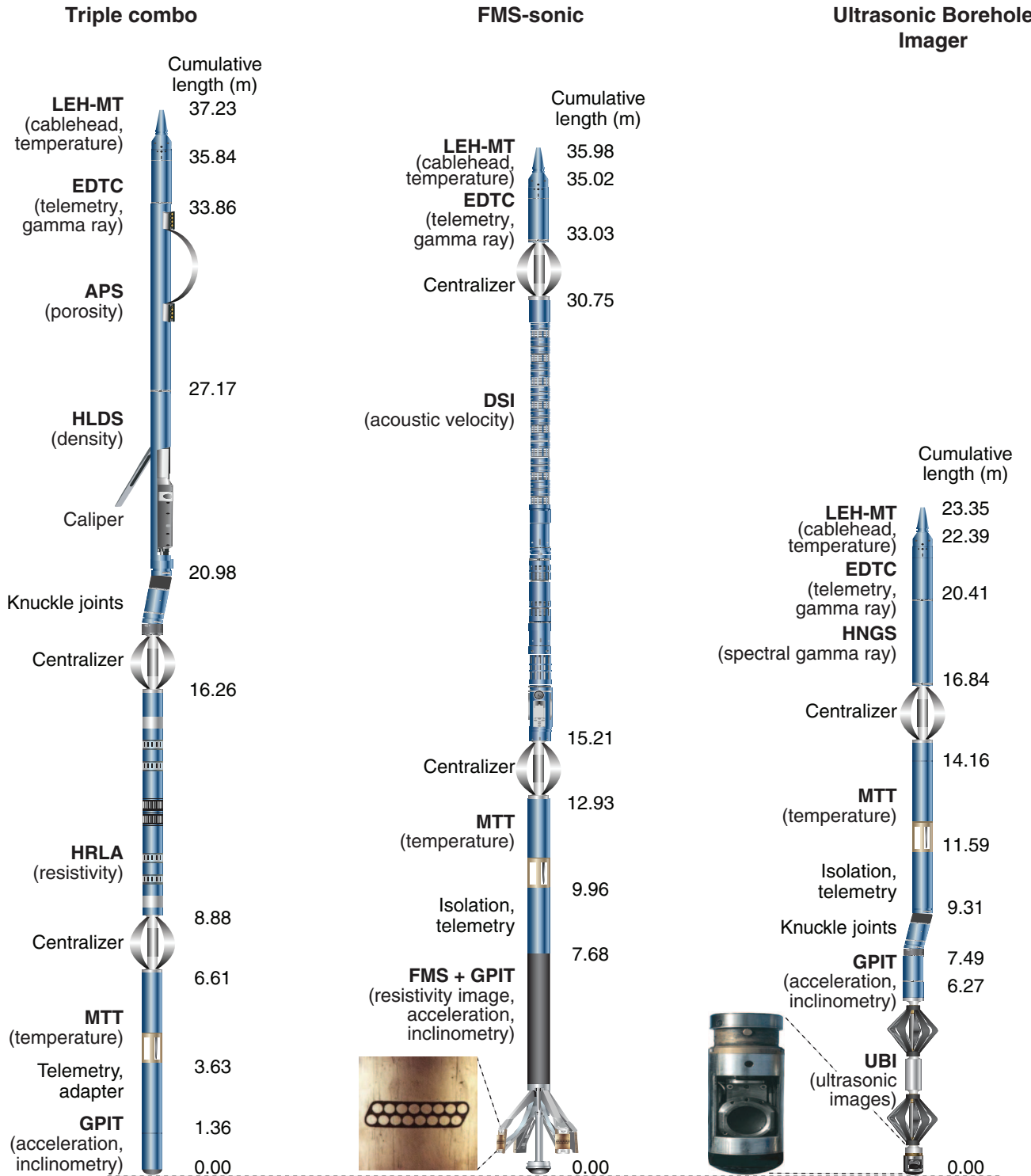




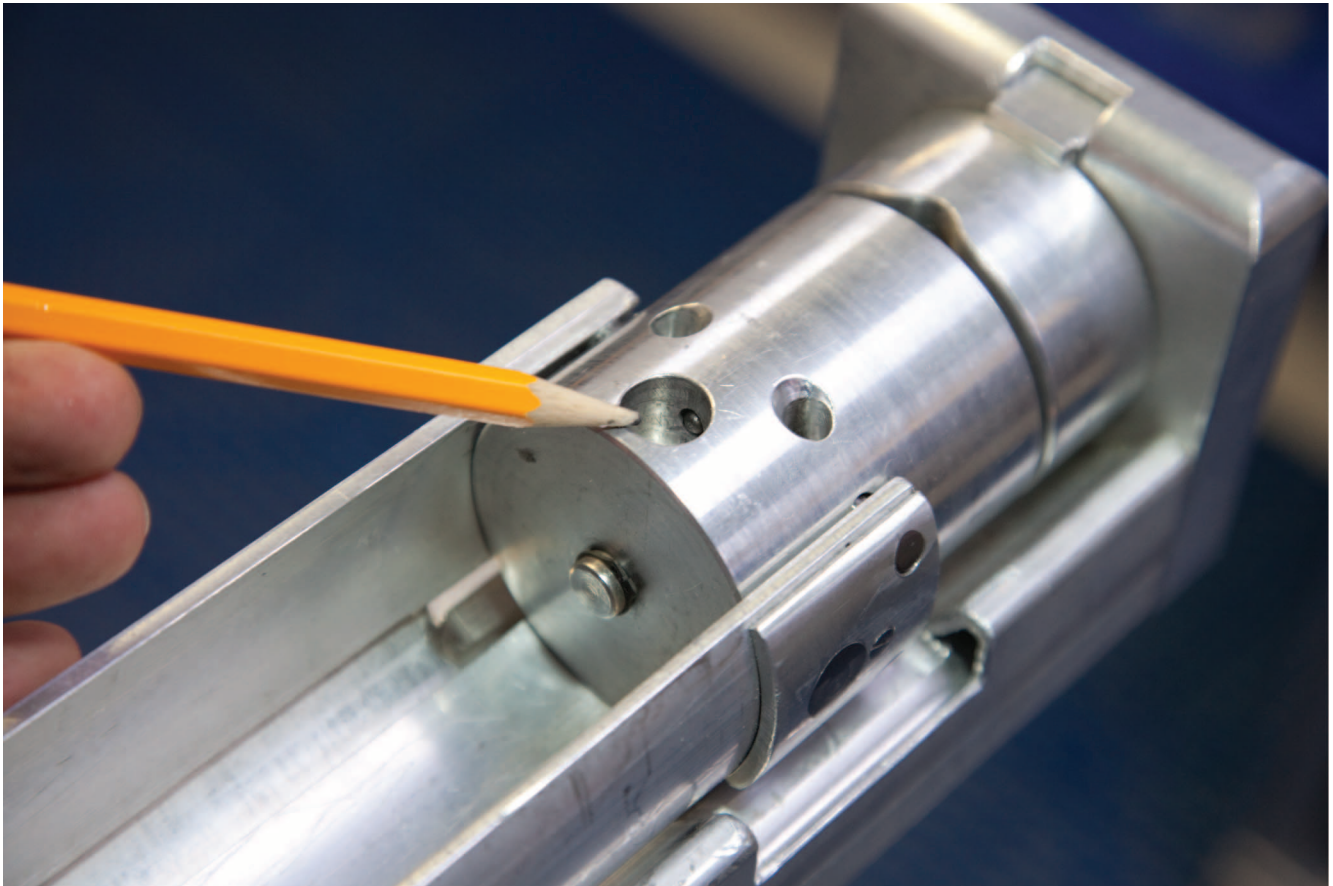
**Figure F27.** Results of gap filtering for a measured core section (335(312)-U1256D-231R-3A). **A.** Raw and culled point magnetic susceptibility (MSPOINT) from the Section Half Multisensor Logger (SHMSL). **B.** Raw, culled, and deconvolved Whole-Round Multisensor Logger (WRMSL) magnetic susceptibility (MS) data. **C.** Culled MSPOINT measured by SHMSL; filtered and scaled MS data measured by WRMSL.



**Figure F28.** Wireline tool strings scheduled for deployment during Expedition 335. LEH-MT = Logging Equipment Head with Tension and Mud Temperature, EDTC = Enhanced Digital Telemetry Cartridge, APS = Accelerator Porosity Sonde, HLDS = Hostile Environment Litho-Density Sonde, HRLA = High-Resolution Laterolog Array, MTT = Modular Temperature Tool, GPIT = General Purpose Inclinerometry Tool, DSI = Dipole Sonic Imager, FMS = Formation MicroScanner, HNGS = Hostile Environment Natural Gamma Ray Sonde, UBI = Ultrasonic Borehole Imager.



**Figure F29.** Aluminum frame used during Expedition 335 for holding whole-round core pieces for imaging their outer surface at four positions spaced at 90° increments. View of one end of the frame, with one of the four bracing strips removed, as would be the case while imaging the outer core surface.



**Table T1.** Nomenclature for non-core material recovered from Hole 1256D during Expedition 335.

Hole	Bit run	Tool	Subsample	Thin section billet	Thin section	Shipboard analysis	Requester	Sample label ID
335-								
1256D	12	DC	Grains	TSB01	TS_09			335-1256D-Run12-DC-Grains-TSB01-TS_09
1256D	12	EXJB	Rock B	TSB01	TS_10			335-1256D-Run12-EXJB-Rock B-TSB01-TS_10
1256D	12	RCJB	Rock D			MADC		335-1256D-Run12-RCJB-Rock D-MADC
1256D	13	FTJB	Rock C			ICP		335-1256D-Run13-FTJB-Rock C-ICP
1256D	15	BSJB					HARR	335-1256D-Run15-BSJB-HARR
1256D	15	FM						335-1256D-Run15-FM

DC = drill collar (may be followed by number), EXJB = external junk basket (EXJB1 and EXJB2 may be differentiated if appropriate), RCJB = reverse circulating junk basket, FTJB = flow-through junk basket, BSJB = bit sub junk basket, FM = fishing magnet. MADC = moisture and density, method C, ICP = inductively coupled plasma–atomic emission spectroscopy.

**Table T2.** Workbooks, tabs, and columns defined for descriptive data capture, Expedition 335.

Workbook	Tab	Team	Columns (N)
Petrology > macroscopic	Section-unit plutonic	Igneous petrology	81
	Section-unit volcanic	Igneous petrology	73
	Contacts	Igneous petrology, structural geology	20
	Texture	Igneous petrology, structural geology	20
	Alteration	Alteration and metamorphism	75
	Veins and halos	Alteration and metamorphism, structural geology	39
Structure > macroscopic	Magmatic fabric	Structural geology	19
	Crystal-plastic fabric	Structural geology	21
	Brittle deformation	Structural geology	27
Petrology > microscopic	TS lithology and texture	Igneous petrology	25
	TS plutonic mineralogy	Igneous petrology	86
	TS volcanic mineralogy	Igneous petrology	NA
	TS alteration	Alteration and metamorphism	58
	TS veins and halos	Alteration and metamorphism, structural geology	74
	TS structures	Structural geology	22
	Total:		640

TS = thin section. NA = not applicable.



**Table T3.** Wavelengths used for major and trace element analyses on the Teledyne Leeman Labs Prodigy ICP-AES instrument during Expedition 335.

Element	Wavelength (nm)	
Major:		
Si	250.690	251.611
Ti	336.122	337.280
Al	308.215	396.152
Fe	239.563	
Mn	257.610	
Mg	280.271	285.213
Ca	315.887	
Na	588.995	589.592
K	769.897	
P	213.618	214.914
Trace:		
Ba	493.409	
Sr	407.771	421.552
Zr	339.198	343.823
Y	360.073	
V	310.230	
Sc	361.383	
Cu	324.754	327.396
Zn	206.200	
Co	228.615	
Cr	205.552	
Ni	231.604	

For elements listed with two wavelengths, the wavelength yielding the best calibration line was identified for each run and used for the determination of concentrations.



**Table T4.** Detection limits, procedural blank, and estimates of accuracy and precision for major and trace element ICP–AES analyses, Expedition 335. (Continued on next page.)

Sample	Detection limit	Procedural blank	BAS-140						JB-1A					
			Run 1	Run 2	Average	Preferred value	Precision (%)	Accuracy (%)	Run 1	Run 2	Average	Preferred value	Precision (%)	Accuracy (%)
Major element oxide (wt%):														
SiO <sub>2</sub>	0.34	BDL	50.69	51.02	50.85	50.58	0.45	0.55	53.74	54.18	53.96	52.89	0.58	2.02
TiO <sub>2</sub>	0.03	BDL	1.03	0.99	1.01	0.98	2.98	2.65	1.31	1.29	1.30	1.32	1.44	-1.38
Al <sub>2</sub> O <sub>3</sub>	0.14	BDL	14.79	14.46	14.63	14.62	1.60	0.03	15.14	14.73	14.93	14.71	1.93	1.50
Fe <sub>2</sub> O <sub>3</sub> <sup>T</sup>	0.28	BDL	11.33	11.25	11.29	11.12	0.56	1.56	9.15	9.17	9.16	9.23	0.15	-0.75
MgO	0.30	BDL	8.38	8.20	8.29	8.16	1.58	1.56	8.13	7.96	8.05	7.86	1.43	2.38
MnO	0.01	0.10	0.19	0.19	0.19	0.19	1.47	-1.30	0.15	0.15	0.15	0.15	0.28	-1.50
CaO	0.16	BDL	12.55	12.43	12.49	12.42	0.67	0.54	9.64	9.47	9.55	9.36	1.26	2.05
Na <sub>2</sub> O	0.06	0.09	1.81	1.74	1.78	1.84	2.59	-3.61	2.96	2.94	2.95	2.78	0.70	6.18
K <sub>2</sub> O	0.01	BDL	0.01	BDL	0.01	0.01	1.61	2.65	1.44	1.41	1.42	1.44	1.44	-1.19
P <sub>2</sub> O <sub>5</sub>	0.05	0.07	0.08	ND	0.08	0.08	27.68	3.23	0.26	ND	0.26	0.26	27.68	-1.46
Totals:			100.86	100.26	100.61	100.00		0.61	101.91	101.29	101.73	100.00		
Trace element (ppm):														
Sc	1.37	BDL	59	45	52	43	18.62	20.25	29	28	28	29	0.14	-1.82
V	16.49	49.71	360	355	357	333	0.96	7.34	216	217	217	220	0.35	-1.57
Cr	12.37	15.64	186	188	187	186	0.91	0.46	425	397	411	415	4.83	-0.87
Co	6.46	BDL	NA	53	53	55	3.78	-2.77	NA	42	42	39.5	2.42	6.12
Ni	27.17	BDL	89	106	98	85	12.26	15.15	148	144	146	140	1.78	4.49
Cu	8.29	BDL	81	77	79	81	4.05	-2.22	57	58	57	55.5	1.50	3.27
Zn	1.99	2.16	49	ND	49	80	1.45	-38.14	107	ND	107	82	1.45	30.02
Sr	2.62	13.83	47	41	44	44	8.25	0.03	444	473	458	443	4.42	3.44
Y	3.72	1.72	31	28	30	24	6.77	24.26	25	23	24	25	4.48	-4.93
Zr	3.13	BDL	43	51	47	49	13.16	-4.31	144	132	138	144	6.25	-4.12
Ba	2.07	7.42	BDL	ND		2			509	499	504	497	1.41	1.35

Precision (or reproducibility) is the standard deviation of the mean of run-to-run analyses. Accuracy is the difference from preferred standard values (Preferred values) to compiled values of the standard materials recalculated on a volatile-free basis. Compiled values are from Govindaraju (1994) for MRG-1 and JB-1A and from Sparks and Zuleger (1995) for BAS-140. Fe<sub>2</sub>O<sub>3</sub><sup>T</sup> = all Fe as Fe<sub>2</sub>O<sub>3</sub>. BDL = below detection limit, ND = not detected, NA = not applicable.



Table T4 (continued).

Sample	Detection limit	Procedural blank	MRG-1					
			Run 1	Run 2	Average	Preferred values	Precision (%)	Accuracy (%)
Major element oxide (wt%):								
SiO <sub>2</sub>	0.34	BDL	40.63	39.56	40.09	39.70	1.90	0.99
TiO <sub>2</sub>	0.03	BDL	3.80	3.79	3.80	3.78	0.10	0.46
Al <sub>2</sub> O <sub>3</sub>	0.14	BDL	8.78	8.71	8.75	8.62	0.55	1.48
Fe <sub>2</sub> O <sub>3</sub> <sup>T</sup>	0.28	BDL	18.17	17.89	18.03	18.16	1.11	-0.70
MgO	0.30	BDL	13.52	13.66	13.59	13.72	0.74	-0.90
MnO	0.01	0.10	0.17	0.17	0.17	0.17	0.84	-0.20
CaO	0.16	BDL	14.81	14.82	14.81	14.87	0.06	-0.41
Na <sub>2</sub> O	0.06	0.09	0.77	0.72	0.74	0.74	4.46	0.92
K <sub>2</sub> O	0.01	BDL	0.18	0.17	0.17	0.18	3.83	-3.07
P <sub>2</sub> O <sub>5</sub>	0.05	0.07	0.09	ND	0.09	0.07	27.68	30.65
Totals:			100.92	99.49	100.25	100.00		
Trace element (ppm):								
Sc	1.37	BDL	66	55	60	56	12.83	8.12
V	16.49	49.71	546	512	529	524	4.55	0.84
Cr	12.37	15.64	480	460	470	444	3.09	5.84
Co	6.46	BDL	NA	109	109	87	3.23	25.73
Ni	27.17	BDL	212	202	207	183	3.40	12.93
Cu	8.29	BDL	128	153	141	133	12.65	6.09
Zn	1.99	2.16	170	ND	170	189	0.61	-9.89
Sr	2.62	13.83	277	275	276	270	0.61	2.30
Y	3.72	1.72	13	13	13	13	1.50	-0.70
Zr	3.13	BDL	102	110	106	104	4.84	1.56
Ba	2.07	7.42	52	50	51	53	2.69	-3.35

**Table T5.** Standard reproducibility and accuracy and precision estimates for gas chromatography analyses of CO<sub>2</sub> and H<sub>2</sub>O, Expedition 335.

Standard	Date (2011)	CO <sub>2</sub> (wt%)	H <sub>2</sub> O (wt%)	
JP-1	25 May	0.284	3.34	
	25 May	0.272	3.48	
	25 May	0.265	3.31	
	29 May	0.289	3.38	
	29 May	0.279	3.34	
	30 May	0.238	2.75	
	31 May	0.271	2.95	
	31 May	0.261	2.89	
	31 May	0.252	2.82	
	31 May	0.249	2.74	
	31 May	0.259	2.93	
	Average (wt%):		0.265	3.09
	Preferred value (wt%):		0.280	2.39
	Expedition 304:		0.290	2.38
Standard deviation (wt%):		0.016	0.28	
Precision (%):		6	9	
Accuracy (%):		-5	29	
BAS-140	25 May	0.099	1.28	
	25 May	0.094	1.54	
	25 May	0.087	1.46	
	30 May	0.086	1.36	
	30 May	0.084	1.35	
	30 May	0.086	1.36	
	30 May	0.084	1.35	
	31 May	0.098	1.50	
	31 May	0.097	1.50	
	31 May	0.098	1.50	
	31 May	0.104	1.52	
	Average (wt%):		0.092	1.43
	Preferred value (wt%):		0.050	1.12
	Expedition 304:		0.090	0.81
Standard deviation (wt%):		0.007	0.09	
Precision (%):		8	6	
Accuracy (%):		85	28	

Preferred values: JP-1 (Imai et al., 1995), BAS-140 (Sparks and Zuleger, 1995). Expedition 304: Expedition 304/305 Scientists (2006).







**Table T8.** International Atomic Energy Agency (IAEA, 2003) recommended energy windows for K, U, and Th gamma ray spectrometry.

Window	Nuclide (photo peak, MeV)	Energy range (keV)
IODP total count window		100–3000
IAEA total count window		400–2810
Potassium	<sup>40</sup> K (1.460)	1370–1570
Uranium	<sup>214</sup> Bi (1.765)	1660–1860
Thorium	<sup>208</sup> Tl (2.614)	2410–2810

**Table T9.** Standard measurements of MACOR ceramic block measured throughout Expedition 335, using the TK04.

Contact fluid	<i>n</i>	Thermal conductivity (W/[m·K])	95% confidence (W/[m·K])	Standard deviation (W/[m·K])
Thermal contact gel	10	1.640	0.007	0.010
Seawater	10	1.625	0.007	0.011
Deionized water	10	1.621	0.002	0.004
No contact fluid	10	1.687	0.013	0.019

**Table T10.** *P*-wave velocities obtained for discrete samples from Expedition 312 core during Expedition 335 following Expedition 312 protocol.

Core, section, interval (cm)	Top depth (mbsf)	<i>V<sub>p</sub></i> (m/s)			Sample text ID
		<i>x</i>	<i>y</i>	<i>z</i>	
335(312)-1256D- 222R-1W, 12	1444.72	5527	5578	5803	CUBE3215391
		5697	5682	5927	
		5728	5726	6031	
222R-2W, 43	1446.53	4747	5408	5460	CUBE3215401
		4977	5674	5395	
		5041	5921	5567	
222R-2W, 46–48	1446.56	5076	5663	5624	CUBE3215411
		5279	5797	5759	
		5418	5895	5819	
231R-1W, 114–116	1489.04	5502	5411	5581	CUBE3215451
		5903	5644	5757	
		5827	5691	5890	
231R-1W, 40–42	1488.30	5458	5110	5533	CUBE3215431
		5712	5463	5863	
		5829	5457	5924	
231R-1W, 42–44	1488.32	5738	5124	5483	CUBE3215441
		5893	5339	5649	
		5968	5465	5687	
231R-3W, 113–115	1491.69	5614	5656	5686	CUBE3215491
		5985	6049	5848	
		6113	6138	5924	
231R-3W, 42–44	1490.98	5755	5901	5637	CUBE3215461
		5870	6036	5751	
		5983	6115	5710	

Measurement of velocity in three orthogonal directions was repeated three times for each sample. Results are biased toward lower values because of incomplete sample saturation. This table is available in [ASCII](#) and in Microsoft Excel format (see 102\_T10.XLS in CHAPTER\_102 in TABLES in “Supplementary material”).

**Table T11.** *P*-wave velocity in three orthogonal directions and corresponding traveltime and caliper separation for one minicube (CUBE 3215471) measured 10 times during Expedition 335, following Expedition 312 protocol.

Hole, core, section, interval (cm)	Depth (mbsf)	$V_p$ (m/s)			Caliper (mm)			Traveltime ( $\mu$ s)			Measurement number	Text ID
		<i>x</i>	<i>y</i>	<i>z</i>	<i>x</i>	<i>y</i>	<i>z</i>	<i>x</i>	<i>y</i>	<i>z</i>		
335(312)-1256D-231R-3W, 52	1491.08	5929	5959	6047	20.24	20.44	20.54	3.41	3.43	3.40	1	CUBE 3215471
		6063	6071	5942	20.27	20.47	20.53	3.34	3.37	3.45	2	
		6248	6251	6122	20.24	20.48	20.55	3.24	3.28	3.36	3	
		6443	6439	6204	20.25	20.50	20.49	3.14	3.18	3.30	4	
		6099	6147	6198	20.24	20.53	20.48	3.32	3.34	3.30	5	
		6419	6084	6424	20.26	20.48	20.50	3.16	3.37	3.19	6	
		6446	6268	6356	20.24	20.47	20.47	3.14	3.27	3.22	7	
		6510	6273	6305	20.15	20.42	20.33	3.10	3.26	3.22	8	
		6272	6496	6450	20.19	20.51	20.42	3.22	3.16	3.17	9	
		6531	6322	6208	20.30	20.40	20.43	3.11	3.23	3.29	10	

This table is available in [ASCII](#) and in Microsoft Excel format (see 102\_T11.XLS in CHAPTER\_102 in TABLES in “[Supplementary material](#)”).

**Table T12.** *P*-wave velocity in three orthogonal directions obtained on the same minicube as in Table T11 under different saturation conditions during Expedition 335.

Core, section, interval (cm)	Depth (mbsf)	$V_p$ (m/s)			Comments	Measurement number	Instrument	Text ID
		<i>x</i>	<i>y</i>	<i>z</i>				
335(312)-1256D-231R-3W, 52	1491.08	5919	5920	5548	No water added	1	GANTRY	CUBE3215471
		5961	5998	5976		2	GANTRY	
		5912	5859	5725		3	GANTRY	
		5841	5839	5893		4	GANTRY	
		5745	5653	5876		5	GANTRY	
231R-3W, 52	1491.08	6064	5811	6051	DI added to surfaces	1	GANTRY	CUBE3215471
		6207	6122	6132		2	GANTRY	
		6231	6105	6266		3	GANTRY	
		6170	6376	6280		4	GANTRY	
		6226	6367	6278		5	GANTRY	
231R-3W, 52	1491.08	6186	6101	6132	Submerged	1	GANTRY	CUBE3215471
		6160	6116	6166		2	GANTRY	
		6101	6138	6156		3	GANTRY	
		6147	6104	6153		4	GANTRY	
		6165	6089	6181		5	GANTRY	

Each experiment was repeated five times. DI = deionized water. This table is available in [ASCII](#) and in Microsoft Excel format (see 102\_T12.XLS in CHAPTER\_102 in TABLES in “[Supplementary material](#)”).

**Table T13.** Sensor details and parameters used for data filtering, Expedition 335.

Logger	Sensor	Physical sensor size (mm)	Sensor resolution (mm)	Distance removed adjacent to gaps (mm)	Minimum piece size (mm)
WRMSL	MS	34	80	40	80
WRMSL	GRA	—	10	10	20
NGRL	NGR	100	200	—	—
SHMSL	MSPOINT	15	3.8	10	20
SHMSL	RSC	60	5	30	60

WRMSL = Whole-Round Multisensor Logger, NGRL = Natural Gamma Radiation Logger, SHMSL = Section Half Multisensor Logger. MS = magnetic susceptibility, GRA = gamma ray attenuation, NGR = natural gamma radiation, MSPOINT = point magnetic susceptibility, RSC = reflection spectroscopy color.



**Table T14.** Downhole measurements made by wireline tool strings, Expedition 335.

Tool string	Tool	Measurement	Sampling interval (cm)	Vertical resolution (cm)
Triple combo	LEH-MT	Temperature	15	NA
	EDTC	Total gamma ray	5 and 15	30
	APS	Porosity	5 and 15	36
	HLDS	Bulk density	2.5 and 15	38
	HRLA	Resistivity	15	30
	MTT	Temperature	15	NA
	GPIT	Tool orientation and acceleration	15	NA

For definitions of tool acronyms, see Table T15. All tool and tool string names except the MTT are trademarks of Schlumberger. Sampling interval based on optimal logging speed. Acoustic imaging approximate vertical resolution is at 500 kHz. NA = not applicable.

**Table T15.** Acronyms and units used for downhole wireline tools and data, Expedition 335.

Tool	Output	Description	Unit
LEH-MT		Logging Equipment Head with Tension and Mud Temperature	
	MTEM	Borehole fluid temperature	°C
	TENS	Cable head tension	lb
EDTC		Enhanced Digital Telemetry Cartridge	
	GR	Total gamma ray	gAPI
	ECGR	Environmentally corrected gamma ray	gAPI
	EHGR	High-resolution environmentally corrected gamma ray	gAPI
APS		Accelerator Porosity Sonde	
	APLC	Near/Array limestone porosity corrected	%
	STOF	Computed standoff	Inch
	SIGF	Formation capture cross section	Capture units
HLDS		Hostile Environment Litho-Density Sonde	
	RHOM	Bulk density	g/cm <sup>3</sup>
	PEFL	Photoelectric effect	b/e <sup>-</sup>
	LCAL	Caliper (measure of borehole diameter)	Inch
	DRH	Bulk density correction	g/cm <sup>3</sup>
HRLA		High-Resolution Laterolog Array Tool	
	RLA (1–5)	Apparent resistivity from computed focusing mode (1–5)	Ωm
	RT	True resistivity	Ωm
	RM	Borehole fluid resistivity	Ωm
MTT		Modular Temperature Tool	
	WTPE	Borehole fluid temperature	°C
GPIT		General Purpose Inclinerometry Tool	
	DEVI	Hole deviation	°
	HAZI	Hole azimuth	°
	F <sub>x</sub> , F <sub>y</sub> , F <sub>z</sub>	Earth's magnetic field (three orthogonal components)	°
	A <sub>x</sub> , A <sub>y</sub> , A <sub>z</sub>	Acceleration (three orthogonal components)	m/s <sup>2</sup>

For the complete list of acronyms used in IODP and for additional information about tool physics, consult IODP-USIO Science Services, LDEO, at [iodp.ldeo.columbia.edu/TOOLS\\_LABS/tools.html](http://iodp.ldeo.columbia.edu/TOOLS_LABS/tools.html).